이학박사 학위논문

Spin-orbit coupling driven electronic properties in 4d transition metal layered perovskites

스핀-궤도 상호작용에 의한

4d 전이 금속 산화물의 전자적 물성

2021년 2월

서울대학교 대학원

물 리 학 과

권 준 영

Spin-orbit coupling driven electronic properties in 4d transition metal layered perovskites

지도교수 김 창 영

이 논문을 이학박사 학위논문으로 제출함

2021년 1월

서울대학교 대학원

물리학과

권 준 영

권준영의 박사 학위논문을 인준함

2020년 12월

위 원 장 유 재 준 (인)

부 위 원 장 김 창 영 (인)

위 원 김 기 훈 (인)

위 원 장 준 호 (인)

위 원 최 영 재 (인)

Spin-orbit coupling driven electronic properties in 4d transition metal layered perovskites

Junyoung Kwon

Supervised by

Professor Changyoung Kim

A Dissertation Submitted to the Faculty of Seoul National University in Partial Fulfillment of the Requirements for the Degree of Doctor of Philosophy

The Graduate School

Seoul National University

Department of Physics and Astronomy

Abstract

Spin-orbit coupling driven electronic properties in 4d transition metal layered perovskites

Junyoung Kwon

Deptartment of Physics and Astronomy

The Graduate School

Seoul National University

A physical character of the condensed matters is based on various electronic interactions. The electric correlation leads to a Mott phase or a superconductivity, and the exchange energy between electron spins constructs complex magnetic properties. Recent studies reveals that, in many systems, the interaction between the electron spin and orbital is crucial. The spin-orbit coupling (SOC) introduces various novel properties in heavy atom compounds, which largely expands the interest of the material choice to the researchers. SOC is studied in many heavy atom systems such as Bi_2Se_3 with topological surface states, or Ir induced magnetic skyrmion with the SOC-driven magnetic interaction. The Sr_2IrO_4 (SIO) is another example of the strong SOC-driven physics, where the SOC induces new eigenstate of the bands to trigger enhance the effect of correlation to form a Mott phase in weakly correlated 5d transition metal oxide (TMO).

This thesis expands the SOC-driven physics with different approach. The role of SOC in heavy atom compounds deals an extreme and simple regime of the

SOC. On the other hand, in the lighter materials, the SOC is not considered as a primary parameter. In 3d TMOs, the SOC is even considered to be quenched because of crystal field driven orbitals are not favorable of SOC. However, the SOC is still effective in 4d TMOs. The magnitude of the SOC energy in 4d system is about 150 meV, which is large enough to reconstruct the band structure and provide similar eigenstates of 5d TMOs. Moreover, since the SOC strength is smaller than the extreme systems, the SOC would not be only parameter to affect the system. Therefore, one may consider the role of correlation, magnetic interaction or many different parameters to the system, and their relation with the SOC. Hence, this thesis is targeting the complex physics of the relatively smaller SOC under interruption from other interactions to pursue understanding of the SOC further.

This thesis introduces the works on two different 4d TMO systems. First, the electron doped Sr_2RhO_4 (SRhO) shows a new exotic metal-insulator transition (MIT) due to moderately spin-orbit coupled band structure. Even though the band structure of the SRhO is similar to SIO, the SRhO shows 2-band metallic behavior, while well split SIO is a SOC-driven Mott insulator. The difference is due to smaller SOC of SRhO, which does not split the two bands enough to fully occupy the lower band. Because of the moderate split, the lower band can be fully occupied before the upper band showing the Lifshitz transition. At the same doping, the study revealed that there is a MIT in the upper band of the SRhO. This thesis introduces the properties of the novel MIT and would suggest the connection between the MIT and the SOC-driven Lifshitz transition. From the angle-resolved photoemission spectroscopy (ARPES) to follow the doping dependent electronic structure, the study reveals the SOC has a crucial role to the MIT in electron doped SRhO.

Second system is the $Sr_2Ru_{1-x}Ir_xO_4$ (SRIO). The none-doped compound Sr_2RuO_4 (SRO) is the metallic system with three bands on the Fermi level. The Ir substitution on the SRO may provide various parameter changes, which includes electron doping, change of SOC and even structure transition. Due to the large differences made by the doping, the SIO has $J_{eff} = 1/2$ Mott phase, where only one half-filled band exists near the Fermi level, which is totally different electronic property compared to SRO system. This thesis tracks the complex change of electronic structure from the SRO to SIO, in order to seek a new physics from the complex parameter changes. From the ARPES experiment the study introduces the anisotropic change of the band, which cause the orbital-selective doping effect on one band. From the electronic structure analysis and tight-binding simulation, the study suggests the band renormalization by the SOC can provide the orbital-selective doping effect.

The studies on 4d TMO systems shows the examples of the SOC-driven physics, even in the moderately small SOC regime. Even though the general materials have various physical parameters competing or interacting with each other, especially for the study of SOC, the most of the studies focused on the simplified models in extreme regime. This thesis may provide an example to distinguish the role of SOC from the other parameters and to verify the crucial role of SOC even in the moderate regime. Those examples may provide deeper understanding of the SOC, and would provide motivation to study the 4d TMO systems to seek new physics.

Key words : Spin-orbit coupling, Electronic structure, Angle-resolved photoemission spectroscopy, 4d transition metal oxide, Metal-insulator transition, Orbital-selectiveness

Student number : 2016-37300

Contents

List of Figures

List of Tables

Chapter 1

Introduction

Recent discoveries of new SOC-driven physics opened new field of physics of SOC in condensed matter physics. Even though the spin-orbit coupling (SOC) is not considered significantly, since it is believed to be quenched in the crystal systems, now, it is well known that the heavy elements such as Bi or Ir has strong SOC which causes various new physics. Furthermore, the extremity of the SOC in heavy elements triggered interest of the lighter materials, where the SOC would be a competing parameter with others to provide unexpected new physics. This thesis, via study lighter 4d transition metal oxide (TMO) systems, would pursue full understanding of the SOC and would introduce a study on new physics driven by moderately small SOC.

1.1 Spin-orbit coupling driven physics

SOC is interaction between the spin and orbital, where both are provided by the electron in condensed matter. The spin is provided by the electron itself, which provides magnetic properties of the system. The orbital is the electron state bound by the atomic nucleus. The orbital provides the character of the system, which may define the conductivity or even the crystal structure. From such parameters, the past research introduced interesting physics such as superconductivity

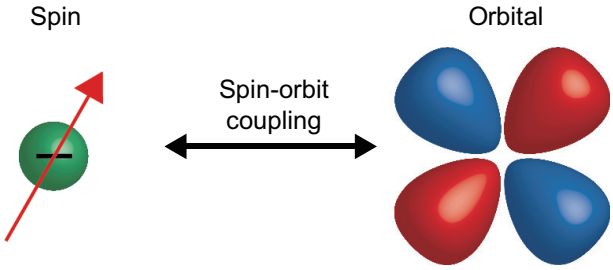

Figure 1.1: Coupling of spin and orbital

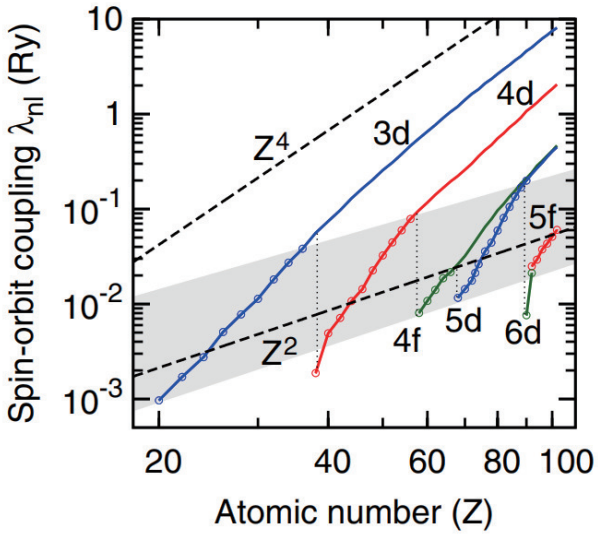

Figure 1.2: Strength of SOC in different orbitals [3]

[1] or correlation driven Mott physics [2]. However, the interaction of the two parameters are not believed to be important in the past research.

The SOC is suggested in the atomic physics. In the spherically symmetric atoms, the orbital includes the magnetic moment which is called orbital angular momentum (OAM). The interaction between the electron spin and OAM is called SOC, where its Hamiltonian can be written as

$$H_{SOC} = \lambda_{SOC} \vec{S} \cdot \vec{L}, \tag{1.1}$$

where $\vec{S}$ is spin driven moment and $\vec{L}$ is OAM. However, the crystal structure, which is the main subject of the condensed matter physics, has no spherical symmetry. Because of the broken spherical symmetry from the crystal structure, the electron orbitals are forced not to have OAM, or OAM is "quenched". Only

recently, the studies on heavy element compounds introduced a role of OAM even in the crystal systems, and have significantly large role of SOC.

The heavy element system consists of the atoms with large atomic number (Z). The electron orbitals in such systems tends to have larger effective radii, which prevents to be affected by the nearby atomic nuclei. Hence, the crystal structure does not totally quench the OAM, causing enlarged effect of SOC. Theoretically, for the atomic systems, the strength of SOC is known to be proportional to Z^4 in atomic system, and empirically, in solid states, the SOC strength is proportional to Z^2 as shown in the Figure 1.2.

Heavy element compounds show various new physics driven by the strong SOC. The typical example would be a topological insulator. In Bi_2Se_3, the SOC driven band inversion cause the topological insulating band structure, which leads to the topological surface state with Dirac cone as shown in the Figure 1.3. The Dirac cone is topologically protected, and shows robust electronic structure even with surface contamination, since the Dirac cone has a chiral spin texture, which is shown with circular dichroism ARPES measurement in the Figure 1.4. The large SOC leads to such unexpected band structure, and opens the large field of topology in condensed matter physics.

Spin-orbit coupling also introduces new type of magnetic interaction, called Dzyaloshinskii-Moriya (DM) interaction. Due to SOC and local inversion symmetry breaking from the crystal structure as depicted in Figure 1.5, one may consider the higher order spin-spin interaction, which can be written as,

$$H_{DM} = D_{DM}\vec{S}_i \times \vec{S}_j. \tag{1.2}$$

Such interaction provides non-collinear magnetic moment ordering, which is not preferred by the Heisenberg type magnetic interaction. Therefore, the DM interaction provides exotic magnetic structure such as a skyrmion (Figure 1.6).

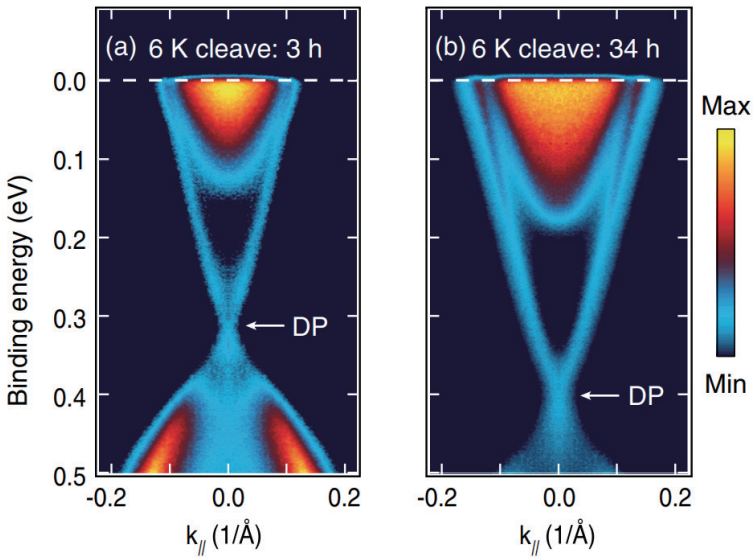

Figure 1.3: Electronic structure of Bi_2Se_3 [4]

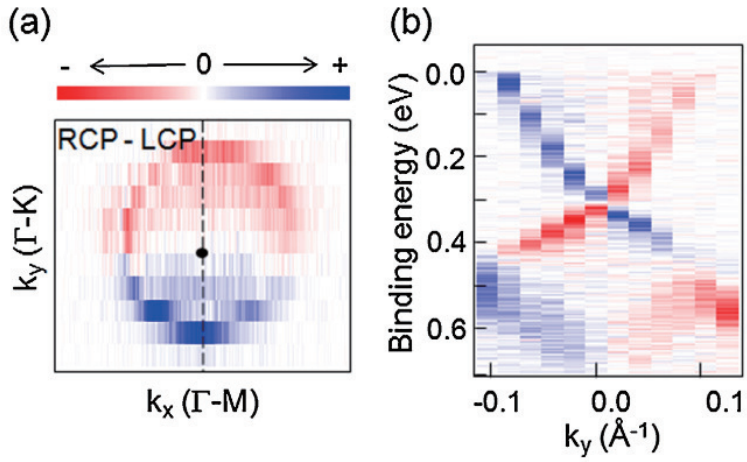

Figure 1.4: Circular dichroism in electronic structure of Bi_2Se_3 [5]

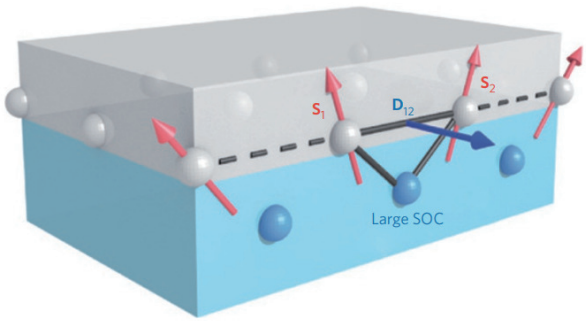

Figure 1.5: Geometry of the DM interaction at interface [6]

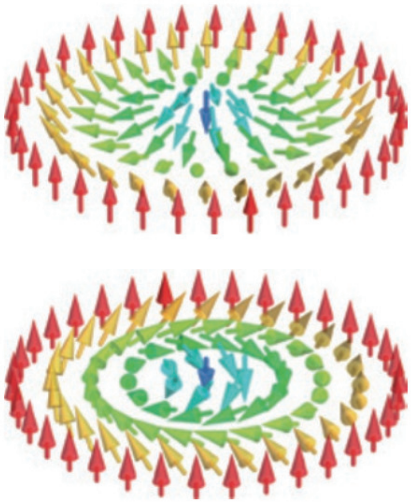

Figure 1.6: Skyrmion spin texture [6]

1.2 Spin-orbit coupling in oxides

In oxide materials, the new SOC-driven insulator phase discovered in Sr_2IrO_4 (SIO) opened a new field of J_{eff} physics [7]. The SIO is an insulator with odd integer electron number occupation of the valence band. Therefore, the systems require an excess explanation further than the normal band insulating mechanism. Such phenomena appear in many systems in 3d transition metal oxides, with large correlation-driven band split called Mott transition. However, it is not plausible for SIO, if consider the fact that the Mott state requires large electron-electron correlation, the Coulomb U, while the 5d transition metals have smaller U compared to 3d transition metal systems.

The recent study of SIO overcome the small U problem with the help of large SOC. The insulating mechanism of the SIO requires to analyze the band structure of the SIO. The study suggested the SOC splits the band structure of SIO and lowers the hopping rate of the valence band, allowing the system to have Mott phase with smaller U.

The band structure of SIO is affected by the two major parameters: crystal

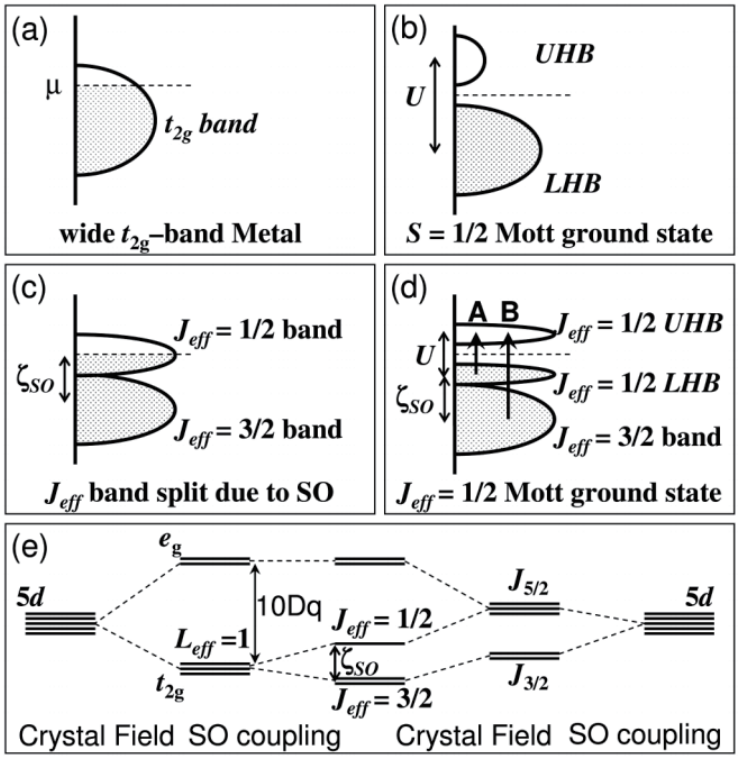

Figure 1.7: Band splitting in SIO by various parameters [7]

field and SOC. The Figure 1.7 shows that the SIO band structure split by the crystal field into e_g and t_{2g}. The e_g consists of $d_{x^2-y^2}$ and d_{z^2} orbitals, t_{2g} consists of $d_{zx}/d_{xy}/d_{yz}$ orbitals, because of the octahedron structure formed by IrO_6. The SOC without crystal field, on the other hand, reconstructs the d orbitals into different eigenstates: J_{eff} states. The Figure 1.7(e) shows the d orbitals split into the $J_{eff} = 5/2, 3/2, 1/2$, which has mixed eigenstates of e_g and t_{2g} orbitals. Therefore, the SOC splits the crystal field driven band structure as shown on the Figure 1.7(e), and resulting the narrow $J_{eff} = 1/2$ band. 5 electrons from each Ir fully occupies the $J_{eff} = 3/2$ bands and half-fill the $J_{eff} = 1/2$. Thus, the half-filled narrow $J_{eff} = 1/2$ band can have Mott phase even with the small U, due to small hopping rate.

The discovery of SOC driven Mott phase in 5d TMO remarkably expand the research of electronics from 3d TMO to 5d systems. The discovery of the SIO insu-

lating phase requires the researchers to study the electronic property of the large SOC system with analyzing the band eigenstates. Studies are done for the pioneering SIO system with various spectroscopic techniques such as angle-resolved photoemission spectroscopy (ARPES) [8–10], x-ray absorption spectroscopy (XAS) [7] or resonant x-ray scattering (RXS) [11], and verified the electronic structure and orbital character of the SIO, and confirmed the SOC-driven renormalization of the electronic structure.

Based on the large interest on SOC in heavy atom compounds, the recent study of the SOC-driven physics become continuously expanded to various systems, even to the lighter elements such as Rh, Ru. Due to singificant band renormalization of the SOC, even lighter elements such as 4d transition metals are considered to have the role of SOC. The analogy of the SOC-driven physics from the 5d transition metal oxides (TMOs), the recent studies on lighter 4d TMOs are implementing the SOC into the band structure analysis, and successfully insist the role of SOC in lighter materials.

1.3 New physics in 4d TMOs

In the past, the studies on 4d TMOs enlightened the physics of correlation by introducing the multi-band structure such as in Sr_2RhO_4 (SRhO) and Sr_2RuO_4 (SRO). Due to smaller crystal field effect from the larger orbital radii, the system has less crystal field split to have single band correlated physics as in 3d TMOs. However, the recent studies found that the lack of crystal field effect cannot fully explain the band structure of the 4d TMOs. The role of SOC is not negligible in 4d TMOs, hence one needs to consider the band eigenstate reconstruction from the SOC to complete the simulation of the bands.

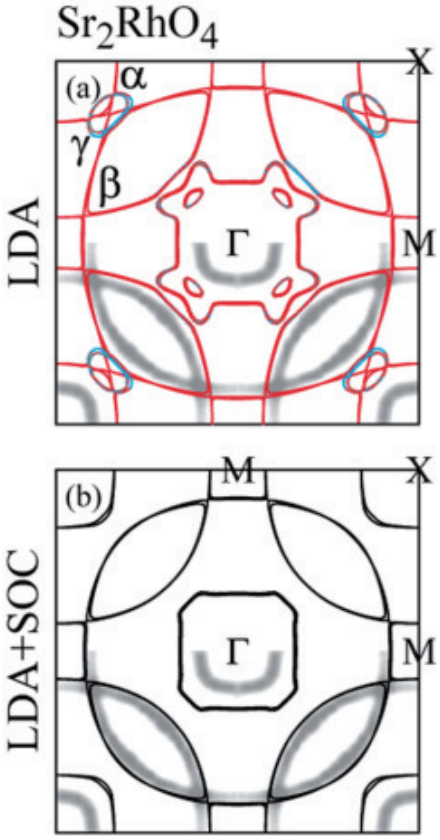

Figure 1.8: SRhO band structure calculation without and with SOC, compared with ARPES [12]

The SRhO is a typical 4d TMO, which is isostructural and isovalent to SIO, however, has totally different electronic properties. SRhO has metallic multi band structure, where the SIO has single band Mott phase due to larger SOC. However, the studies showed that the band structure of SRhO strongly affected by the SOC. The Figure 1.8 shows the band structure of SRhO without and with SOC, showing that band structure requires the effect of SOC.

It is similar in SRhO. The SRO has straight 2D like band structure along k_z momentum axis as in Figure 1.9. Even though the system is layered perovskite structure, the interaction between the layers cannot be ignored, hence the band structure of SRO shows non-2D dispersion of bands as in Figure 1.9(e) and (f). However, the SOC lifts the degeneracy of the crossing points and creates more

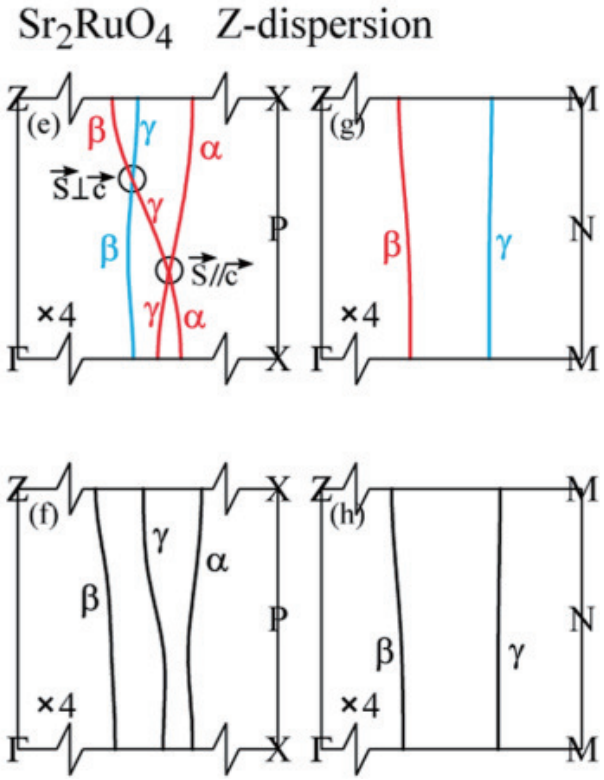

Figure 1.9: SRO k_z dispersion with and without SOC [12]

straight, non-dispersive band structure to form 2D-like band structure as in Figure 1.9(g) and (h).

Therefore, unlike the past view on the 4d TMOs, the SOC is significantly affecting the electronic structure of 4d TMOs. The studies suggest that the SOC in 4d TMOs strongly modifies the crystal field driven, SOC-quenched 3d TMO electronic structure. However, the SOC in 4d TMOs would not be a dominant parameter, since strength of SOC in 4d systems are about 150 meV [12], which is smaller than the SOC in 5d systems with more than 400 meV SOC [10]. In 4d systems, the SOC would be competing parameter with the parameters such as correlation, magnetic interaction.

Hence, the study of the SOC in the 4d system would provide complexed mixed eigenstates as the Figure 1.10 depicts. The crystal field driven real orbital eigenstates would not be the true eigenstates, nor the strong SOC-driven physics.

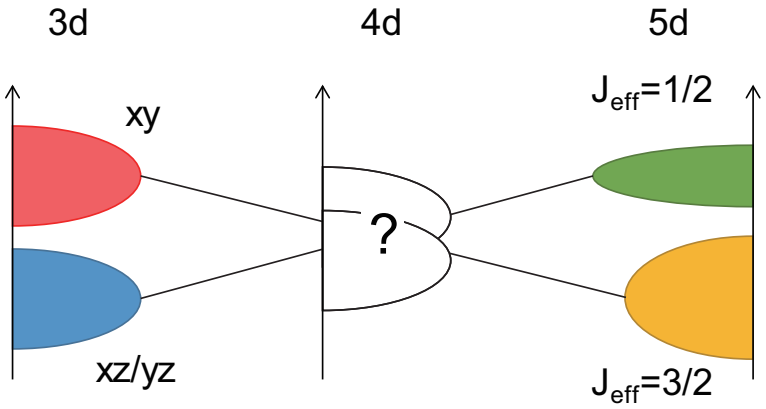

Figure 1.10: Possible new orbital character in 4d TMO

Unlike the extremely simple strong SOC physics in the 5d TMO systems, the SOC in 4d TMO would provide competing nature of the SOC with other interactions, which would provide much deep understanding of the SOC.

This thesis is targeting on the complex new electronic structure of 4d TMO systems driven by the moderate SOC. Mainly through the angle-resolved photoemission spectroscopy (ARPES), this thesis would provide global investigation of the band structure of 4d systems to reveal the role of the moderate SOC and provide new physics achieved by the SOC. First, the Lifshitz transition driven metal-insulator transition (MIT) in electron doped SRhO would be introduced. Second, the SOC-driven orbital-selective property in Ir doped SRO would be introduced. The thesis is organized as follows.

In chapter 2, the methods used to grow, characterize and analyze the systems would be introduced. The chapter would include the basics of the ARPES measurement, which would include photoemission process, construction of the general ARPES analyzer system and photon sources. The section would be followed by the introduction of the growth and characterization methods, which would include floating zone and flux method of single crystal growth and transport, magnetization, and structure characterization methods.

In chapter 3, the experimental result of electron doped SRhO system would be

introduced. The chapter includes basic properties of the undoped SRhO with previous studies on electron doped SRhO systems. Followed by experimental results including transport measurement results and band structure analysis. Through the experiments, the possible mechanism of the MIT discovered in $Sr_{2-x}La_xRhO_4$ (SLRhO) would be suggested, with universality of the Lifshitz transition driven MIT with similarly electron doped $Sr_{2-x}Ce_xRhO_4$ (SCRhO) system.

In chapter 4, the experimental result of $Sr_2Ru_{1-x}Ir_xO_4$ (SRIO) system would be introduced. The chapter would introduce basic properties of the SRO and SIO, the end compounds, which would be followed by the previous research of the SRIO. The band structure analysis would follow the introduction and would suggest the new orbital-selective doping effect discovered in SRIO. Tight-binding calculation assisted analysis of the orbital-selectiveness would provide the SOC-driven mechanism of the orbital-selectiveness, in the context of the full band evolution of the SRIO with SOC change.

The final chapter 5 would summarize the works, with showing suggestion of the further study.

Chapter 2

Experimental Methods

The main purpose of the research in this thesis is to investigate the band structure of the 4d TMOs. To directly study the band structure, the ARPES is used as a main tool. ARPES allows the direct observation of the electronic structure of many crystalline systems, which may provide solid evidence of the SOC-driven physics in this thesis. Moreover, to obtain the fine quality samples for the ARPES measurements, various single crystal growth method is used: the floating zone method and the flux method. Simple characterization measurements are also performed to identify/qualify the properties of the newly grown samples. This chapter introduces the basic methods used to study the 4d TMOs in this thesis.

2.1 Angle-resolved photoemission spectroscopy

Photoelectron spectroscopy is one of the famous spectroscopic experiment, which provides the information of electrons in any condensed matter systems. Initiated by the first observation of the photoelectron by Edmond Becquerel in 1839 [13], and theoretical proposal from Albert Einstein in 1905 [14], the photoelectric effect is well known effect from the condensed matter with electron excitation of the system. The photoemission spectroscopy utilizes two conservation laws to measure the electronic states in the condensed matter system and reveals the property of

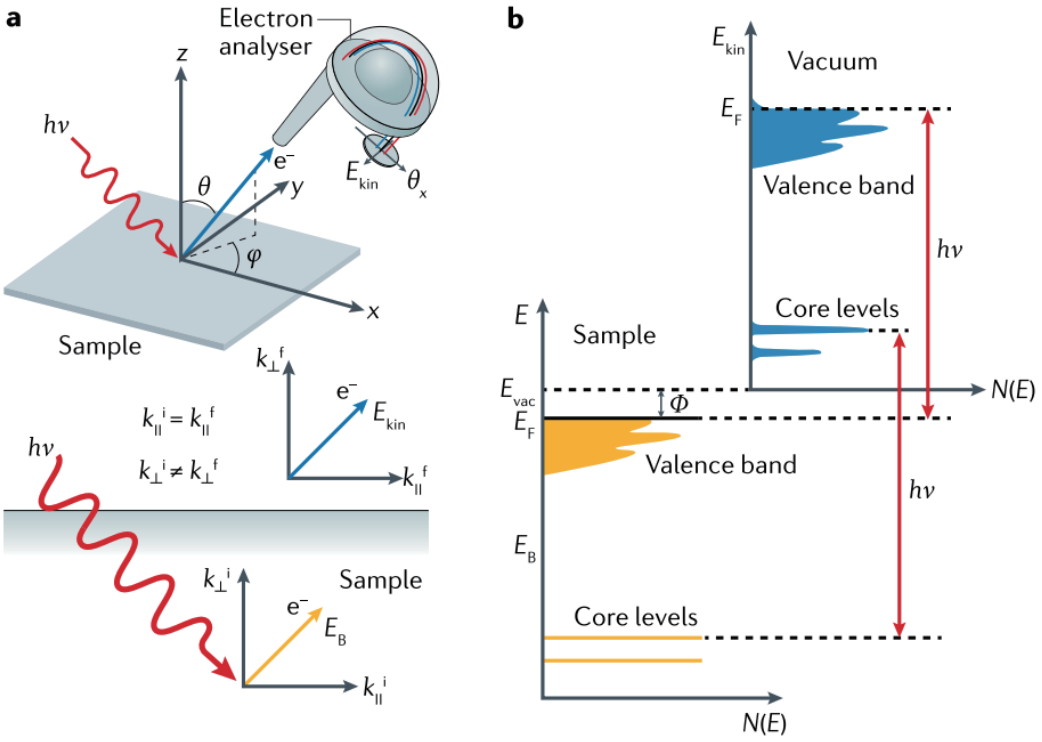

Figure 2.1: Schematics of photoelectron process [15]

the system.

First, the conservation of the energy provides the binding energy of the electron in condensed matters. The X-ray photoemission spectroscopy (XPS) method is developed in 1957 [16], which utilizes the kinetic energy of photoelectrons to show the information of the binding energy of the electrons in matters by considering the energy conservation law written as

$$E_k = h\nu - E_B, \tag{2.1}$$

where E_k is kinetic energy of photoelectron, $h\nu$ is the photon energy to excite the electron, and E_B is binding energy of the photoelectron before excitation. The photoelectron excited from the photon energy $h\nu$ can be traced back to the original electron energy states. As shown in the Figure 2.1(b), the electron energy states in the solid can be directly observed by the photoelectron energy spectroscopy. As a result the photoemission energy spectra from the XPS can be

reconstructed to be a core level structure of the electron energy states, which may provide the information of the chemical composition and bonding nature of the system.

As the discharge lamp is discovered to generate the ultraviolet (UV) source, the low energy excitation of the electrons by UV light source is utilized in 1961 [17], which developed the UV photoelectron spectroscopy (UPS). The UPS, unlike the XPS, has smaller kinetic energy of electrons that would allow much higher energy resolution. Such high resolution allows to observe direct information of the valence band structure near the Fermi level as shown in the Figure 2.1(b). This encouraged the implementation of the second conservation law.

Second conservation law is the momentum conservation. As the information of the valence band become accessible from the UV source, the dispersion of the band structure, the momentum resolution is required to study the complex crystal systems with various orbital characters. The momentum resolution is possible to provide the detailed and direct observation of the electronic structure, allowing one to reconstruct the valence band structure that defines the material's electronic properties.

The measurement of the electron momentum is done by resolving the photoelectron angle from the sample surface. For the simplified photoelectron process drawn on the Figure 2.1(a), the electron emission angle θ and ϕ allow to disintegrate the photoelectron momentum into two components: the momentum parallel to the surface ($k_{\parallel}$) and the momentum perpendicular to the surface ($k_{\perp}$). The two components of the photoelectron momentum can be written as

$$k_{\parallel} = \sqrt{2mE_k}(\sin\theta\cos\phi\hat{k_x} + \sin\theta\sin\phi\hat{k_y}) \tag{2.2}$$

$$k_{\perp} = \frac{\sqrt{2m(E_k\cos\theta^2 + V_0)}}{\hbar} \tag{2.3}$$

where V_0 is the inner potential. The two momentum vectors span the 3D momen-

tum k_x, k_y, and k_z [15], which adds the momentum resolution of the photoelectrons. Since the photoelectron has momentum conservation, it is natural to infer the electron in the sample has same momentum.

Hence, the proper electron analyzing system and light source, the "angle-resolved photoemission spectroscopy", would provide the full information of the energy-momentum relation of electronic structure in the condensed matter. In the following of the section, the detailed process and examples of the electron analyzer and various light source would be introduced.

2.1.1 Electron analyzers

There are two different methods to resolve the energy and momentum with electron analyzer. The one is hemisphere analyzer with electromagnet bending the electron path, which resolves the energy and a momentum of the electrons. The other is the time of flight (ToF) analyzer that measures velocity of the electron to measure the energy and 2D momentum space. The two analyzers have different mechanism of measuring photoelectron, which allows variety of choice to study photoelectrons.

The hemisphere analyzer is the most common analyzer used for ARPES measurement. As shown in the Figure 2.2, the hemisphere analyzer uses the hemisphere electromagnet to bend the electron path to resolve the energy. To do so, first, the photoelectrons from the sample enter to the lens system before the hemisphere. The lens would apply the electric field which would change a certain kinetic energy to desired pass energy (E_p). The kinetic energy of the rest of electrons is be affected by the lens simultaneously, and enter to the slit. Therefore the bunch of photoelectrons with energy around the E_p would enter the hemisphere. The hemisphere applies the magnetic field to bend the electrons' path. The mag-

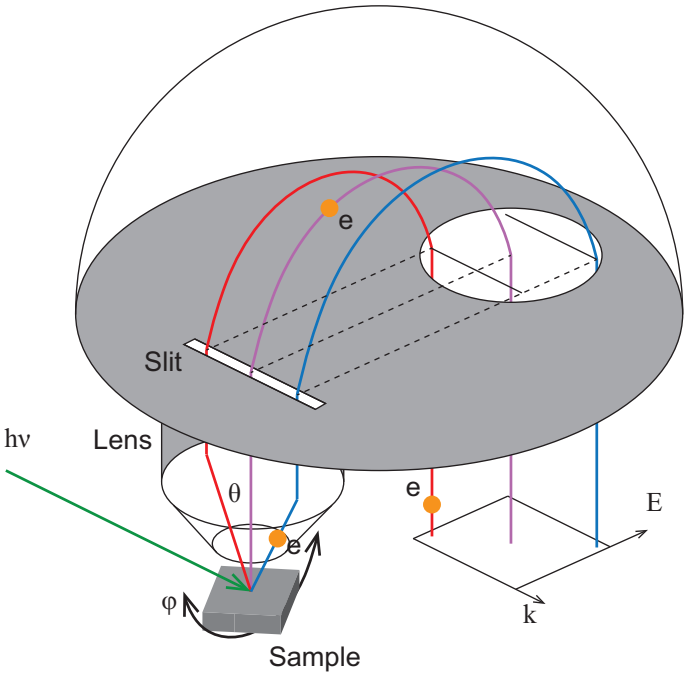

Figure 2.2: Schematics of hemisphere electron analyzer

nitude of the magnetic field is set to exactly bend the electron with E_p onto the center of the 2D measuring device. The electrons with higher energy would be bent less, and the electron with lower energy would be bent more. Hence, on the 2D detector, as shown on the Figure 2.2, the energy of the electrons can be distinguished by measuring position of the final electron.

The photoelectron angle θ can be straightforwardly resolved by the final position of the electrons on the 2D measuring device, due to momentum conservation. However, the electrons which does not enter the slit cannot be measured at once. Therefore, to resolve the angle perpendicular to the slit (ϕ), one needs to rotate the sample as depicted with the black arrow in the Figure 2.2. Hence, with hemisphere analyzer with rotating sample may resolve two momentums and energy.

To measure the final electrons, hemisphere analyzer typically uses three step of detector units. First, the electron hits the multiple channel plate (MCP), which consists of the nano-fabricated arrays of electron multiplier that enlarges the photoelectron signal enough to be measured. The multiplied electron bunch then

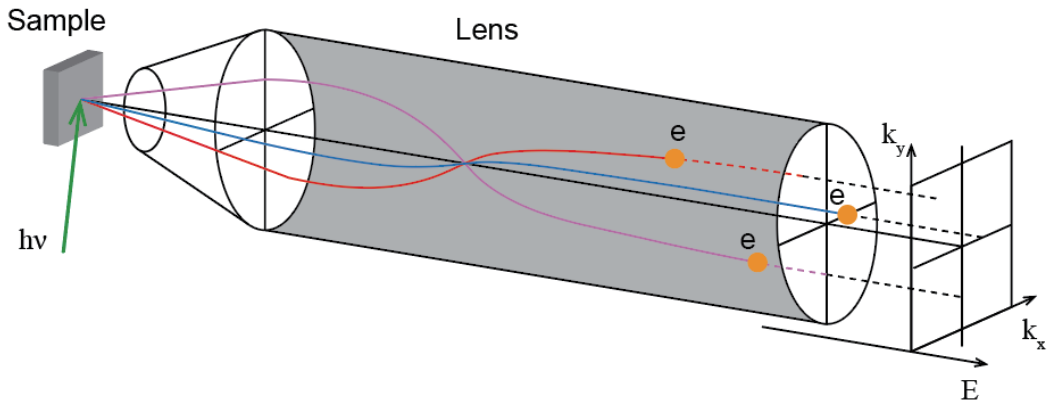

Figure 2.3: Schematics of ToF electron analyzer

hits the scintillator unit, which provides light signal from the charged particles. Eventually the light induced by the electron can be measured with the 2D CCD unit that may resolve one angle axis and an energy axis.

On the other hand, the ToF analyzer resolves the momentum and energy in different way. As the Figure 2.3 shows, the ToF analyzer is shaped as long cylinder, where the electron passes through. Basic idea of the ToF analyzer is to measure the electron energy from the speed of the electron, and measure the electron momentum with the 2D position detector. Hence, the ToF analyzer may resolve two momentum and energy of the photoelectron without manipulating the sample.

To measure the electron speed, ToF analyzer requires a pulsed laser source, with proper strength and wavenumber to excite one electron per pulse. A photoelectron excited by a pulse of laser would enter the cylinder and the analyzer counts the time of the electron propagation within the cylinder and measures the electron position on the 2D detector. To measure the electron, ToF uses MCP with a delay line detector (DLD). The MCP multiplies the electron, as it does in the hemisphere analyzer, and the bunch of electron hits the DLD to measure the time of the hit and the position of the hit. Therefore, the ToF analyzer may

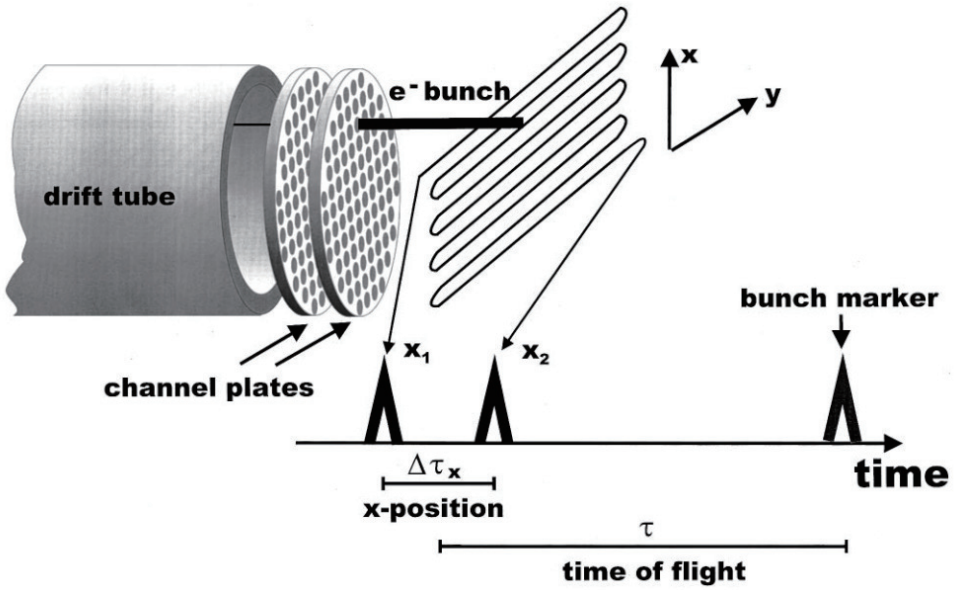

Figure 2.4: Schematics of DLD [18]

measure 2D momentum with energy at once.

The DLD is the key element of the ToF analyzer. The DLD consists of two different wires. The Figure 2.4 shows one of the wire. The wire typically is arranged to form an array of the straight lines. The electron bunch would provide current flow when it hits the line, and the electric pulse is measured on each end of the line. The time would be recorded from each end, which are denoted by x_1 and x_2. The signal arrival time difference of the x_1 and x_2 would represent the position of the wire, where zero difference indicating that the electron hit on the middle of the wire. Also, the speed of the electron can be measured from the sum of the signal arrival time on x_1 and x_2, where the sum represents the electron hitting time. The electron hitting time would be compared with the pulsed laser signal timing to calculate the speed of the electron. However, the ToF analyzer would not distinguish the double excitation of electrons per pulse, which would double the x_1 and x_2 signal, making electronics impossible to distinguish.

The electron analyzer has been largely developed so far, and it still is developing to measure many systems. Recent studies showed various new techniques

with the electron analyzer. The photoemission electron microscopy (PEEM) [19] is widely used microscopy with the electron analyzer that may show the real space image of the samples, which includes the information the electron energy states on each real space points. Typically, magnetization or orbital distribution on the sample can be measured with PEEM. Moreover, using the magnetic film, the electron analyzer even can resolve the spin of the electrons, which would provide spin-resolve ARPES measurement [20, 21].

Additional to the analyzer technique, the technique of the light source has been largely developed. The light may provide more efficient and faster measurement, as well as introduce new parameter that provides further information of the sample's electronic structure, such as time-resolution.

2.1.2 Light source

To achieve the light source for ARPES, there is one major requirement. Since the photoelectric effect only occurs when the electron receives the energy larger than the work function, the light source requires to have energy exceed the work function. For many cases, the work function is around 5 eV, hence, one needs the UV source with wavenumber much smaller than about 248 nm (5 eV).

Gas discharge lamps would be a common choice of the light source. Gas discharge lamp utilizes the low-pressure gas. With low-pressure, gas atoms such as He, Xe, and Ne, become plasma, by losing electron. The discharge lamp consists also with the electron gun, which would provide extra electron to the low-pressure gas. The excess electron would be recombined with the gas plasma, and provide fluorescent light with photon energy same with the emission lines of the gas. For instance, the He discharge lamp, which is the most common choice for ARPES experiment, provides 21.2 eV (He Iα) and 40.8 eV (He IIα) [22, 23]. The discharge

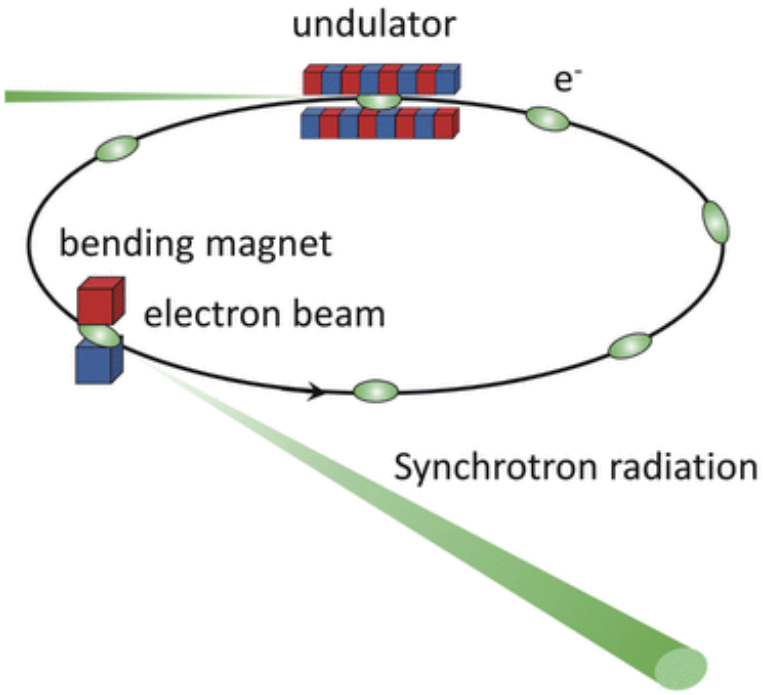

Figure 2.5: Schematics of synchrotron radiation [24]

lamp requires no large space and can only run with simple controller. Therefore, many lab ARPES facility utilizes the discharge lamp as a light source.

The limitation of the discharge lamp is clear. Since the gas providing the discharge effect has discrete emission lines, the energy of the discharge lamp is not a variable. This would be a large obstacle in many cases, since the perpendicular momentum resolution requires the varied electron kinetic energy. Since the band structure of any crystal structure would have 3D band dispersion, the fixed photon energy would not provide the full investigation of the band structure. Moreover, depending on the orbital character of the bands and the dispersion along the perpendicular direction, the fixed photon energy may have small cross section for certain electrons, forbidding the observation of such electrons. Therefore, the photon energy variation is required.

The synchrotron light source is a common choice to vary the light energy. Synchrotron source typically generates the light by bending the fast propagat-

ing electron bunch as shown in the Figure 2.5, which provides the acceleration driven light emission from the charged particles. Since the manipulation of the electron bunch with the magnet would differ the condition of emitting photons, the synchrotron source can change the energy of the emitting light as well as polarization.

Also, the brightness of the synchrotron can be significantly larger compared to discharge lamp. This provides several advantages. First, the data would have less noise because of the better statistics. Second, since the much larger flux allows one to cut the light source, resulting smaller beam radii. The smaller beam provides less spatial variation allowing more fine momentum and energy resolution, also allows to measure smaller sample. Typically, synchrotron source has flux larger than the 10^13 photons/s with maintaining beam radii less than a hundred μm [25].

However, the synchrotron has a few limitations. Even though the energy is variable, the variable energy range is limited for each facility, depending on the beam line specification and synchrotron energy. The energy resolution is also limited since the monochromatized light has larger energy dispersion compared to discharge lamp. Typically, the energy resolution of the synchrotron source is larger than 10 meV, while the He lamp provides around 1 meV resolution. Most of all, the synchrotron facility is not quite accessible, compared to a lab source.

Recently, to overcome the limitation of the discharge lamp and the synchrotron facility, the new source of laser is gathering interest. The laser commonly used for generating light with energy less than about 1.5 eV, which is not suitable for photoemission. However, recent development of ultra-short high energy pulsed laser allowed one to achieve large intensity even after the nonlinear optical effect, which typically reduces the intensity of the incident light by 1/1,000,000. Using various

materials with large nonlinear effect, such as β-BaB_2O_4 (BBO) or $KBe_2BO_3F_2$ (KBBF), one can enlarge the energy of the photon source and achieve large enough photon source to generate the photoelectrons [26]. Moreover, a proper pulsed laser source allows to implement extra dimension; the time-resolution [27–29].

In this thesis, in order to measure the 4d TMO electronic structure, it is necessary to use the fine analyzer with high energy. Typically, the few tens of eV light source is used to measure the 4d systems which can be easily achieved with the synchrotron radiation source. Moreover, because of the light source selection, the ToF analyzer (who needs pulsed light source) cannot be used, hence hemisphere analyzer is used for the experiments. With choice of hemisphere analyzer and high energy synchrotron radiation, proper observation of the spin-orbit coupled 4d TMO band structure would be introduced.

2.2 Sample growth

Angle resolution for the photoemission requires fine single crystal with clear surface. There are many ways to grow a single crystal, but for SLRhO, floating zone method is suitable to achieve fine crystal, and for SRIO, flux method is suitable. Furthermore, resistivity, magnetism or X-ray diffraction can be used to qualify the fine crystallinity of the grown samples and verify the basic physical properties of them. In this chapter, overall single crystal growth and basic measurement techniques would be introduced.

2.2.1 Floating zone method

Floating zone method is used to grow many crystalline systems such as SRO, Manganites such as $TbMnO_3$ [30], and cuprate superconductors [31, 32]. Float-

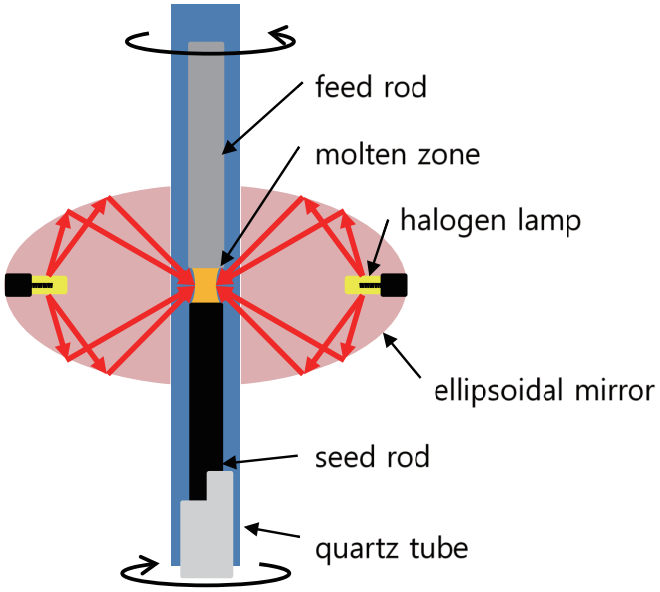

Figure 2.6: Schematic geometry of floating zone image furnace

ing zone method basically follows the method of flux method, which melts the polycrystlline samples and crystalizes it by slow cooling. However, unlike the flux method, floating zone method doesn't use any container while melting the ingredients.

Basic set up of the floating zone furnace can be schematically drawn as Figure 2.6. With two or more mirrors as depicted on the Figure 2.6, the light emitting from the halogen lamp would be focused on the center where the polycrystalline rod forms a molten zone. Hence, the floating zone furnace is also called as an "image furnace". Within the image furnace, the feed rod and seed rod is placed and attaching with each other, where the molten zone exists on the middle which is melted feed rod by the focused light. The rods simultaneously move to downward direction so as to move the molten zone. Hence, the molten feed rod, the polycrystal, crystalizes on the seed rod with slowly cooling down as the molten zone moves, and the further moving feed rod would accumulate the crystal further on the seed rod.

During the crystallizing process, the freely moving polycrystalline molecules

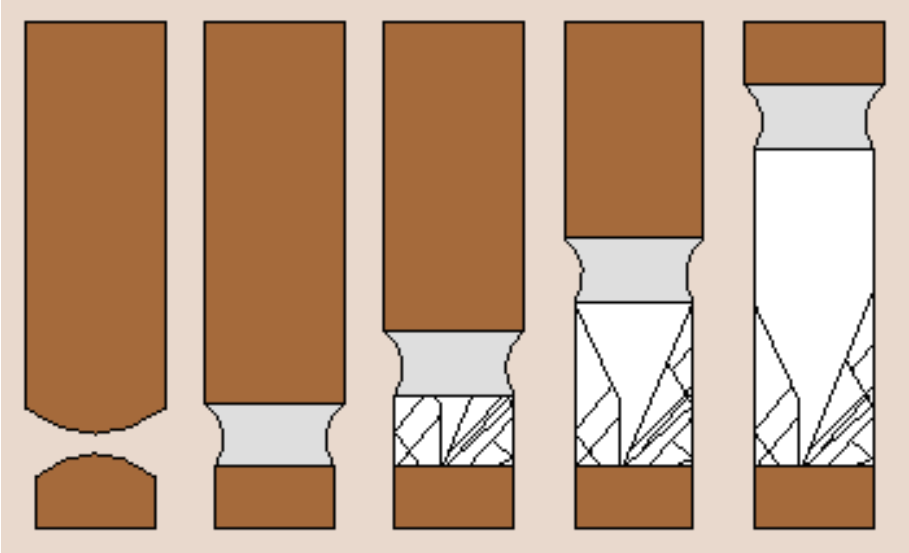

Figure 2.7: Crystal growth process of floating zone method [33]

accumulate on the seed rod with random crystal orientation as depicted in the Figure 2.7. As one of the crystal randomly become larger, the crystal molecules would probabilistically tend to follow the larger crystals, eventually making all the rod into one crystal. To achieve fully melted molten zone and homogeneity of the crystal, the seed rod and the feed rod is rotating along the opposite direction, which would mix the molten molecules well enough to be totally melt and stay homogeneous.

The major difference and advantage of the floating zone method compared with flux method is the fact that floating zone method doesn't use any container. Flux method uses various crucibles to contain the melted resolution, which consists typically of alumina or Pt. Even though the composition of the containers are chose not to chemically react with the resolution, often the materials form a chemical bonding and cause the impurity in crystal. However, the floating zone method would avoid such reaction. Furthermore, the containers would include excess residuals which may induce contamination of the crystal. However, as the molten zone is freely circulating with the rotating rods, the molecules of the crystal would freely bond with the crystal and the residuals may be left in the

molten zone. In such contamination free environment, the crystallinity and the stoichiometry of the crystal could be better compared to other methods.

However, there are limits for using floating zone method. Since the molten zone should be attached in between the feed and seed rods, the viscosity of the molten crystal is a critical factor. The materials with less viscosity would not hold the molten crystal on the molten zone. In that matter, floating zone method is suitable to grow the SLRhO system.

2.2.2 Flux method

Flux method is one of the basic method to grow single crystals. The flux method utilizes the difference of the solubility for different temperature of the materials, indicating most of the systems which can be melted can be crystalized by the flux method. Many systems can be grown with the flux method, for instance YBCO [34], SIO [35, 36], and many others are well known examples.

The most characteristic process of the flux method is that it uses flux to melt the crystals. For the floating zone method, most of the samples are melted without any flux, which is often called as self flux method. However, the self flux cases, the melting point of the material is very high, and even exceeds the decomposition temperature. The flux resolves the problem, by dissolving the desired material into a suitable solvent at much lower temperature.

The method is useful for many systems, such as SIO. The Ir is known to easily form clusters at high temperature, which is not suitable to use the floating zone method without flux. It is very difficult to prevent the cluster since it requires the slow growth speed while growing the floating zone. Moreover, the high temperature of floating zone growth vaporizes the Ir oxide compounds which would not give the proper stoichiometry. However, the chloride flux would significantly lower

the melting (dissolving) temperature of SIO polycrystal and almost eliminates the volatility, hence slow growth can be achieved.

However, the limit of the flux method is clear. The suitable solvent should be found to perform the flux method. The solvent should dissolve the crystal at temperature, as well as should be easily removed to pick up clean crystal without breaking or surface contamination. Moreover, the solvent used for oxide materials easily dissolve the ceramic crucibles, which often requires to use the expensive Pt based crucibles. The suitable crucible even can always be the source of contamination as described in the previous subsection. Though, due to the problem of Ir, the SRIO material requires to be grown with the flux method.

2.3 Sample characterizations

Quantitative estimation of the quality of the grown crystal is necessary. There are many parameters that can determine the crystal quality. First, the crystallinity indicates the periodicity of the atomic arrangement within the crystal, which is necessary for every property of crystal. Next, the resistivity is a typical representation of the electronic state, that may show the rough band occupation status by allowing to determine the system's metallicity. Magnetization is also a possible indication of the crystal property, showing whether the system has magnetic ordering or even a short range interaction that may affect the system's electronic structure. In this subsection, some of the typical characterization methods are introduced.

2.3.1 Structure characterization

First, the crystallinity, the quality of the crystal structure can be character-

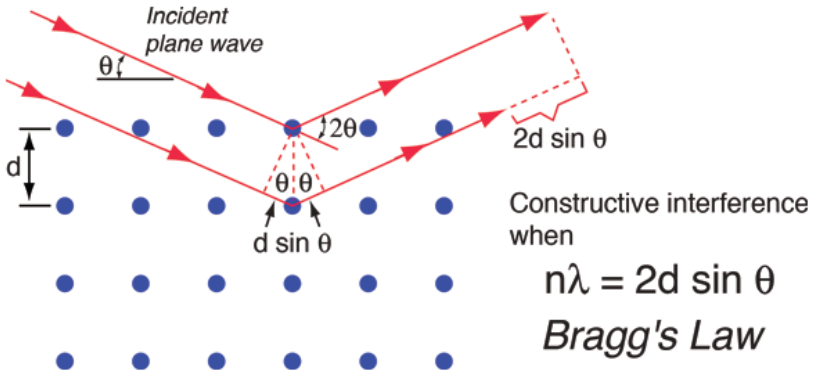

Figure 2.8: Schematic geometry of XRD experiment [37]

ized typically with diffraction techniques. There are various diffraction techniques. Commonly for the polycrystalline sample, the X-ray diffraction (XRD) technique with monochromatic light source can be utilized to verify the crystal structure. The XRD measures the interference patterns from the reflected X-ray from the sample structure. For a certain condition, as shown in the Figure, the constructive interference from the crystal planes would provide strong reflection. Such a condition is called Bragg condition (Figure 2.8), written as

$$2d\sin(\theta) = n\lambda \tag{2.4}$$

where d is the spacing between the Bragg planes, consists of atoms in the crystal. λ is the wave number of the X-ray source and θ is the incident angle of the source with respect to the Bragg plane, which requires to be equal to angle of outgoing light. Since the polycrystalline samples have microscopic crystals with every orientation, it is not necessary to rotate the sample to satisfy the Bragg condition. Hence, as shown in the figure, the X-ray diffraction pattern can be achieved only with changing the θ.

However, the satisfying the Bragg condition with single crystals requires additional effort. For a certain Bragg planes, since the incident and emission light angle θ must be equal to meet the Bragg condition, the single crystal must be ro-

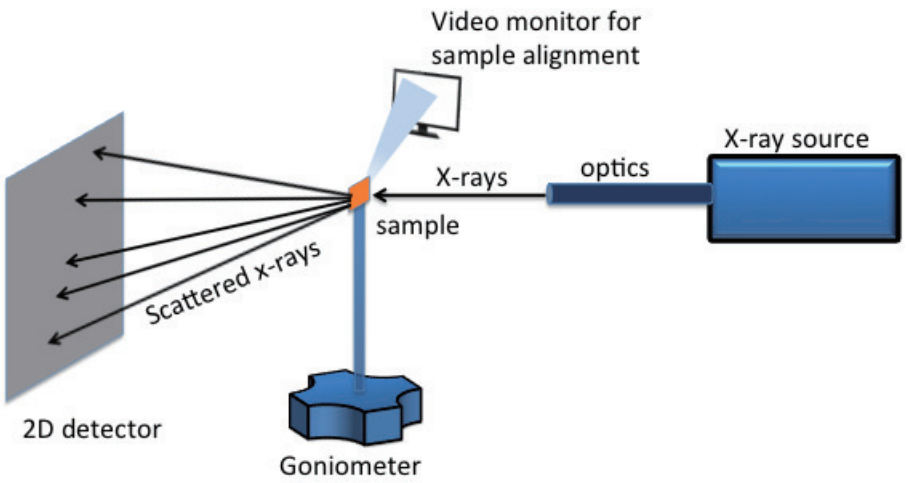

Figure 2.9: Schematic geometry of 2D detector SC-XRD [38]

tated to a certain angle. Therefore, to observe the whole Bragg peaks as with the polycrystalline samples, one needs to rotate the sample over all spherical angle.

There are two typical ways to measure Bragg peaks of the single crystals. One is to raise the efficiency of changing θ, and the other is to widely vary the λ. The first technique uses the 2D X-ray detector, that can measure the various Bragg peak at once. As shown in the Figure 2.9, the single crystal XRD (SC-XRD) measurement shows Bragg peak over 3D reciprocal spaces, which contains identical information with the polycrystal XRD. From the SC-XRD pattern, one may verify the crystal structure of the single crystal and whether the crystal structure contains unwanted symmetry.

The other method, widely varying λ is used in the Laue diffraction technique. The Laue diffraction utilizes the broadband X-ray source, which contains the wide energy range of the X-ray light. Therefore, the θ can be varied with the changing λ, which results in the data as schematically shown in the Figure 2.10. With the Laue diffraction, one may verify the crystallinity by estimating the Bragg peak width. A broad bragg peak on the Laue diffraction pattern indicates the disordered crystal structure. Also, the crystal direction can be determined by the

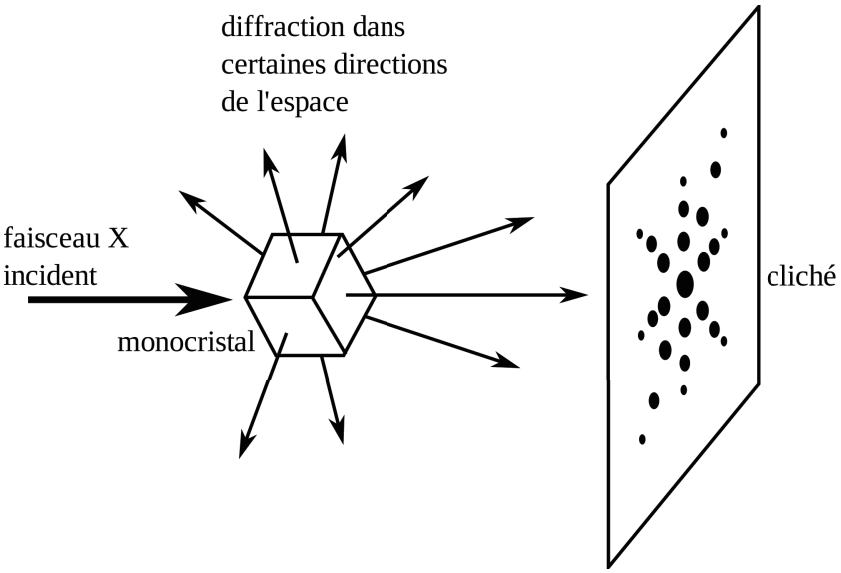

Figure 2.10: Schematic geometry of Laue diffraction [39]

Laue diffraction.

With such diffraction measurement, the crystallinity, how periodically ordered the crystal is, can be quantified with the diffraction patterns. With the proper crystallinity, further study of the intrinsic physics of the crystal is possible.

2.3.2 Electric characterization

Resistivity can measure the basic electronic property of the sample. The metal and insulator, which is extreme ends of the electric property, show different behaviors of resistivity under changing temperature. The metal induces the resistivity of the electron mainly by electric force between the atomic nuclei with the freely propagating electrons, therefore lowering the temperature reduces the atomic fluctuation and hence lowers possibility for nuclei to hinder the electron propagation. Therefore, the metallic sample would show decreasing resistivity when lower the temperature. However, the insulator shows totally different behavior. In the insulator, the electrons are localized around the atomic nuclei, which requires the external energy to be excited to hop into the nearby atoms. At the high temper-

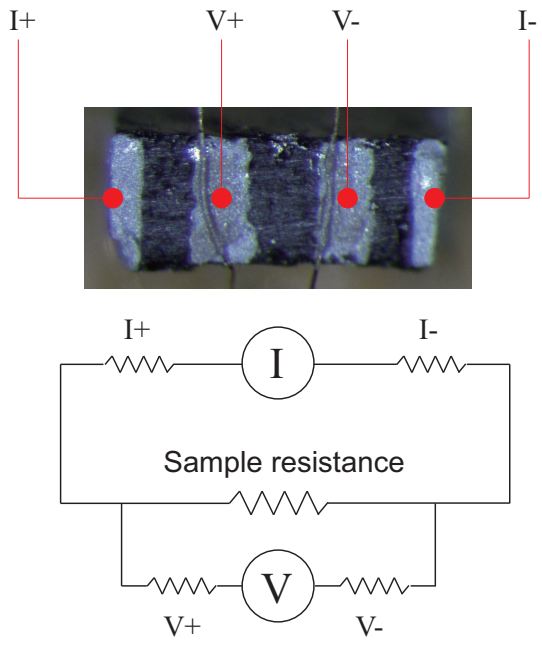

Figure 2.11: 4-probe resistivity setup

ature, the atomic fluctuation may excite the electrons which may allow relatively free electronic hopping, however at the low temperature, the fluctuation would become smaller, making it difficult for the electron to hop. Typically, resistivity in the insulator with gap follows

$$\rho \propto e^{T/E_g} \tag{2.5}$$

where the E_g is gap of the insulator. Hence, the resistivity of the insulator exponentially increases with the temperature lowering.

To measure the resistivity of the system, 4-probe measurement is a common way. Since it is necessary to make the electrode to measure the voltage or current and to apply them, the most challenging task to measure resistivity is to make the electrodes on the sample to have less contact resistance. There are many ways to reduce the contact resistance for each electrode, and 4-probe is a good way. The Figure 2.11 shows the 4-probe setup made with silver epoxy on a sample. Typically, two probes (I+ and I-) are used to apply the current and the other two (V+ and V-) are used to measure the voltage, as shown in the Figure 2.11. The two

contact resistance on the current source sides are attached to sample resistance in series, hence, the current applying doesn't depend on the contact resistance. Also, for the voltage measurement, the contact resistance is connected parallel to the sample resistance, the voltage measurement cannot be affected by the contact resistance, considering the voltage reader typically has large resistance.

Such resistivity measurement would verify the metallicity of the samples, and hence may show the clue of the valence band structure of the samples. Electronic structure of metal may imply Fermi surface of the bands, and the insulating behavior would predict the gap feature or localized electrons from various reason. For every sample, resistivity measurement would provide good clue before measuring the electronic structure with ARPES.

2.3.3 Magnetic characterization

Last but not least, the magnetic property of the crystal can be a clue to estimate the electronic property of the crystal. In many cases the magnetism of the sample would show various modification of the samples. The ferromagnetism, may appear in the system with large spin-spin interaction (exchange interaction), which aligns the spins onto the same direction. Such ordering results in splitting of the band structure with the exchange energy. The antiferromagnetism, which orders the spins antiparallel to each other, often creates the enlarged magnetic unit cell larger than the crystal structure. The unit cell doubling driven replica band may hybridize with the original bands, creating the hybridization gap. For some case when the hybridization triggers the insulating gap is called the Slater insulator.

The typical magnetic orders can be measured with temperature dependent magnetization measurement. The ferromagnetic behavior is typically shown with

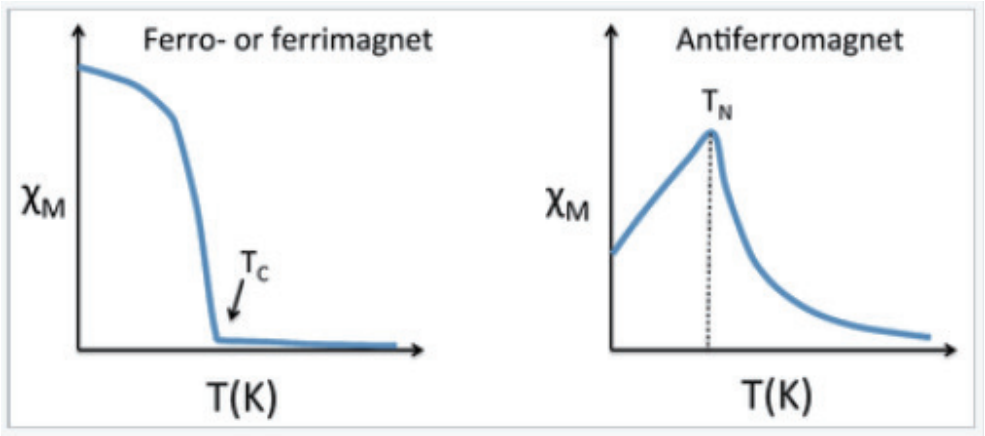

Figure 2.12: Typical magnetization behaviors [40]

the abrupt increase of the magnetization as shown in the left panel of the Figure 2.12, which is due to the spins ordering onto a certain direction. The offset temperature is called Curie temperature (T_C). The antiferromagnetism, on the other hand, is represented by the peak (the right panel of the Figure 2.12). When magnetic field is applied to measure the magnetization, the temperature lowering typically enlarge the net magnetization due to lowering of the thermal fluctuation effect. However, it suddenly decreases below the critical temperature, as the antiferromagnetic ordering aligns the spins in antiparallel direction. Hence, the peak shows up in the Figure, and the critical temperature is called Néel temperature (T_N).

With above basic characterization, one may acknowledge the system properties. With combination of the ARPES measurement, one may achieve the role of electronic structure to such characters. It may allow one to verify the role of each orbital to the system, which may reveal the role of new orbital in the moderately spin-orbit coupled 4d TMOs.

Chapter 3

Metal-insulator transition in electron doped Sr_2RuO_4

From the electronic structure study, electron doping on SRhO showed unexpected SOC driven MIT. The mother compound SRhO is isovalent and isostructural to the SIO system, the SOC driven $J_{eff} = 1/2$ Mott insulator. However, because of the smaller SOC, the SRhO system has good metallic behavior. The discrepancy of the SRhO and SIO also can be found from the electron doped compounds, where the La doping on SIO collapses the Mott gap, while the La doped SRhO shows the insulating property, which is shown by the polycrystalline study. In this chapter, in order to investigate the electronic property of the 4d TMO SRhO system, the electronic structure analysis with ARPES measurement is introduced. The study suggests a new type of intrinsic MIT in La doped SRhO system, which may be triggered by the moderateness in SOC of the Rh based system.

3.1 Previous results

The mother compound SRhO has layered perovskite structure with A_2BO_4 type composition [41]. SRhO contains layers of RhO_6 octahedrons, each share corners with neighboring octahedrons as shown in the Figure 3.1. The notable structure is that the octahedrons within the layer has in-plane staggered rotation along the

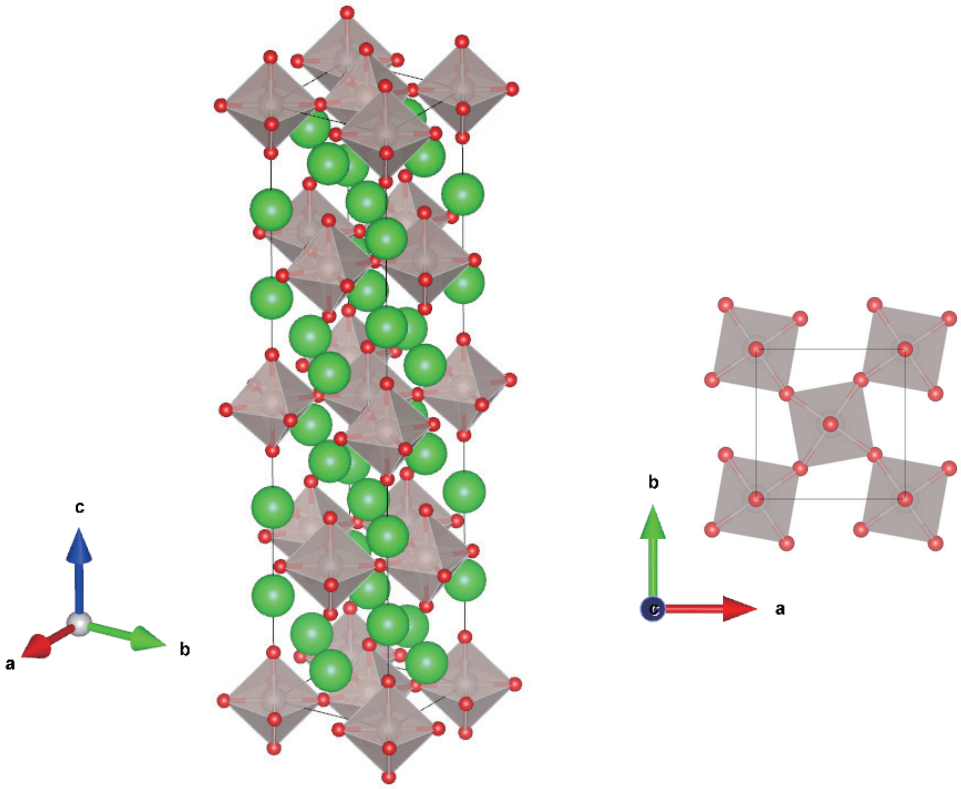

Figure 3.1: Crystal structure of SRhO

c-axis, creating the unit cell doubling.

The electronic property of the SRhO is well known for the good metallic behavior with Fermi liquid property at low temperature. Studies show that the T^2 behavior of resistivity as in the upper panel of the Figure 3.2, which indicates the Fermi liquid property, appears along both c-axis and ab-plane. Moreover, due to the layered structure, the c-axis and ab-plane resistivity shows strong anisotropy, which makes c-axis resistivity about 1000 times larger than that of ab-plane.

The magnetism in the lower panel of the Figure 3.2 shows no strong temperature dependence. The usual paramagnet with localized magnetic moments follows Curie law, the $1/T$ dependence of the magnetization. However, the SRhO magnetization doesn't show such dependence, but globally static behavior with little dispersion. The theory of Pauli paramagnet suggests such temperature in-

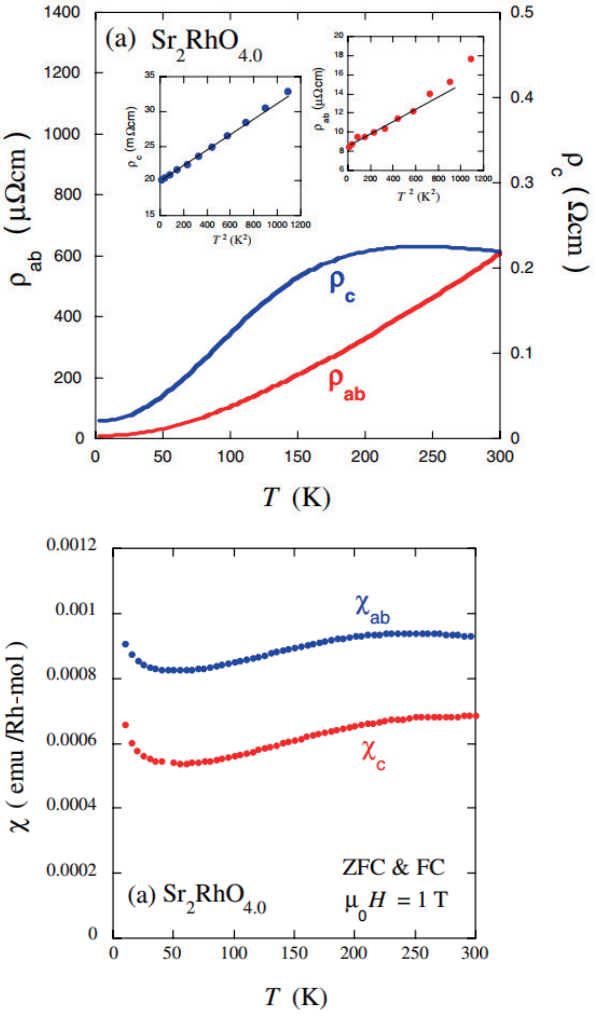

Figure 3.2: Electronic and magnetic properties of SRhO [42]

dependent magnetization in the itinerant system, which is consistent with the metallic behavior of the SRhO.

The electronic structure of SRhO contains three 4d orbital driven valence bands around the Fermi level, which mainly has t_{2g} character from the octahedron driven crystal field. Total five electrons fill the valence bands due to Rh^{4+}. Two of the electrons fully occupies one band (γ) and the rest of electrons partially occupies the remaining two bands (α and β), which makes the system partially occupied metal. Therefore, the Fermi surface is consist of the α and β bands, which is shown in the Figure 3.3.

The typical character of the Fermi surface bands are commonly defined with

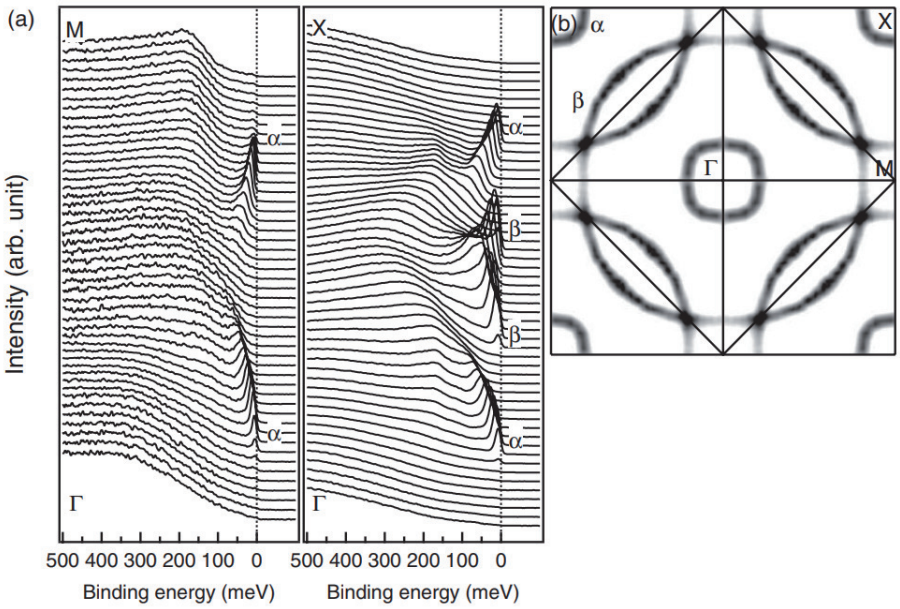

Figure 3.3: Electronic structure of SRhO [43]

the crystal field driven eigenstates ($d_{xz/yz/xy}$). However, recent theoretical studies showed much realistic correction to the band calculation with considering the effect of SOC. The Figure 3.4 shows the LDA calculation results, showing better prediction of the realistic ARPES band structure by considering SOC. Furthermore, consideration of Coulomb interaction provides effectively enlarged SOC [44], which suggests that the SOC in SRhO significantly affects the eigenstates. The SOC mixes the $d_{xz/yz/xy}$ band eigenstates and opens the hybridization gap at crossing points of the bands, resulting new, but better prediction of band structure.

Recognizing the significance of the SOC would introduces a new point of view to understand the electronic properties of SRhO. The tight-binding calculation on the Figure 3.5 compares SRhO and large spin-orbit coupled SIO band structure by varying the SOC without considering the Mott gap formation of SIO. In the right panel of the Figure 3.5, the SIO band structure with large SOC energy about 400 meV defines strongly spin-orbit coupled eigenstates. The color scale shows the projection of each band to the J_{eff} eigenvalues. The β band can be almost

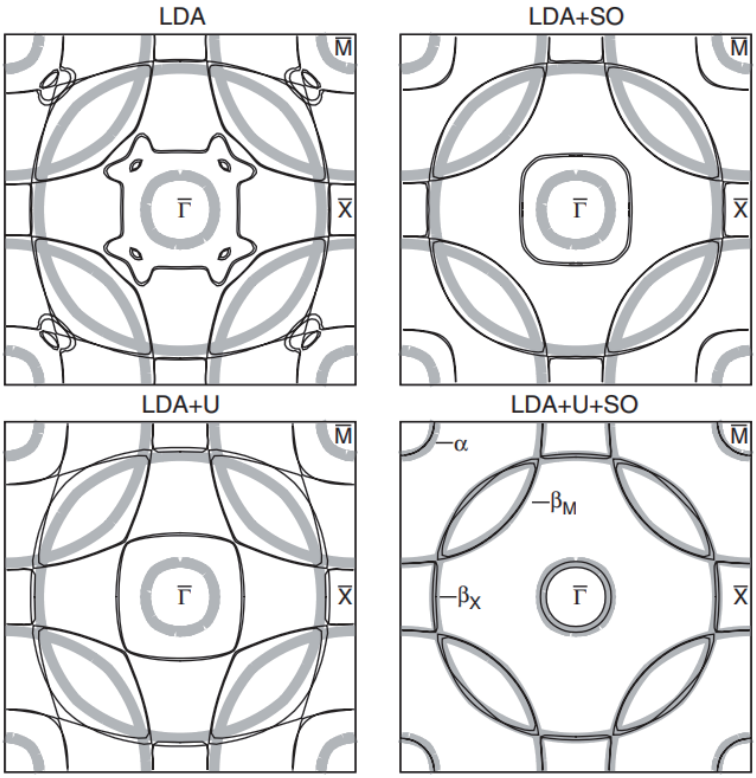

Figure 3.4: LDA calculation of SRhO compared with ARPES [44]

fully projected to the $J_{eff} = 1/2$ band, while the α shows strong $J_{eff} = 3/2$ character. As a result of SOC split, the α band clearly separated from the β, so the α band is completely occupied and located below the Fermi level. Unlike the SIO, the SRhO in the left panel of the Figure 3.5 has smaller SOC driven split between the α and β band, resulting the 2-band metallic fermi surface. However, it is noticeable that the band projection of α and β of SRhO is not so different from that of SIO showing similar color scheme.

The recent calculation with LDA+SOC also supports the similarity of the α/β band character in the two systems, SIO and SRhO. The Figure 3.6 shows the band calculation result, with projection of each eigenstate with each J_{eff} orbitals. From the result, the α and the β band structure of each system shows little qualitative discrepancy and shows similar projection pattern, indicating that the SIO and SRhO has similar band eigenstates. As it did in the tight-binding

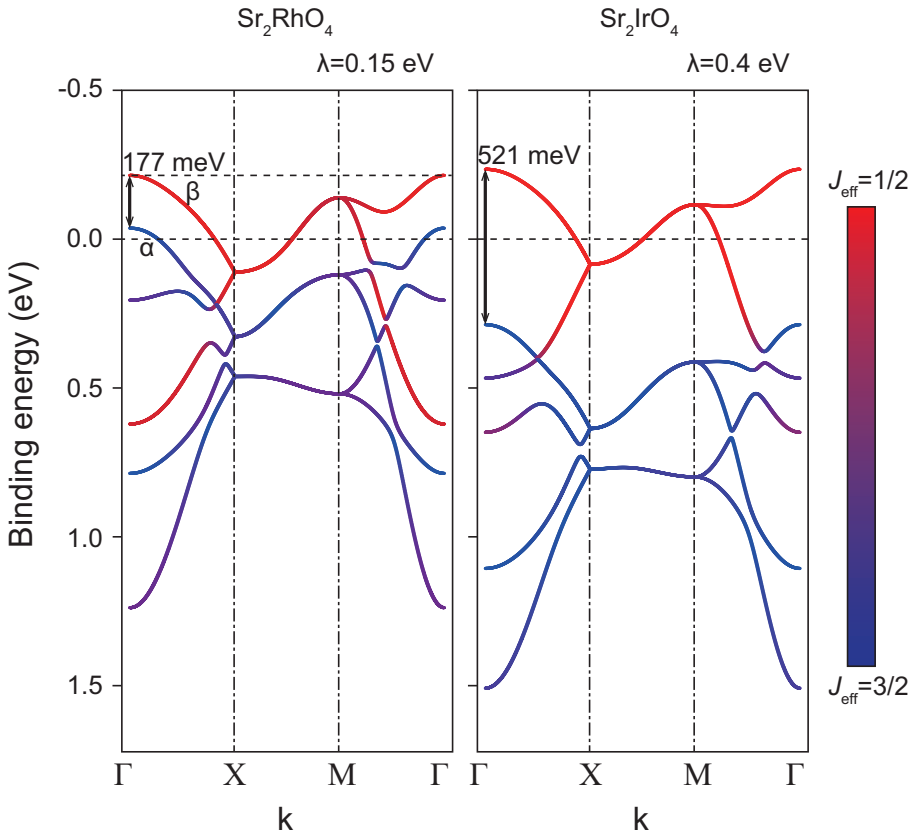

Figure 3.5: Tight-binding calculation of SRhO and SIO

calculation result from above, the major discrepancy between the SIO and SRhO band structure is the energy split between the bands due to difference of the SOC.

Therefore, if the α (strongly $J_{eff} = 3/2$) is fully occupied in the SRhO, the only remaining β (strongly $J_{eff} = 1/2$) band would show similar $J_{eff} = 1/2$ physics as in the SIO. This intrigues the electron doping study to fill up the α band from SRhO, creating the single-band Fermi surface with β band, resulting the similar band structure with SIO. The bandwidth of the $J_{eff} = 1/2$ would be much smaller than the β band without SOC ($d_{xz/yz}$), which would provide unexpected transport properties in electron doped SRhO system.

Though, previous study shows a controversy on the electronic property of electron doped SRhO. The polycrystalline study of La doped SRhO (SLRhO) shown in the Figure 3.7 discovered a MIT around La contents $x = 0.2$. How-

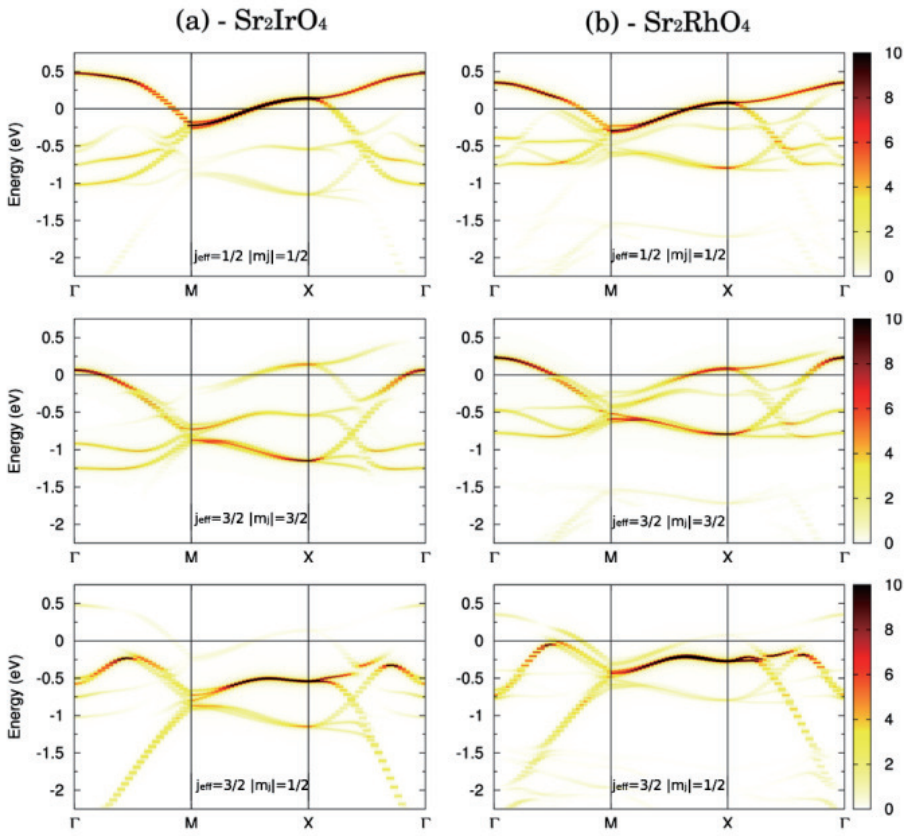

Figure 3.6: LDA calculation with J_{eff} projection of SRhO and SIO [45]

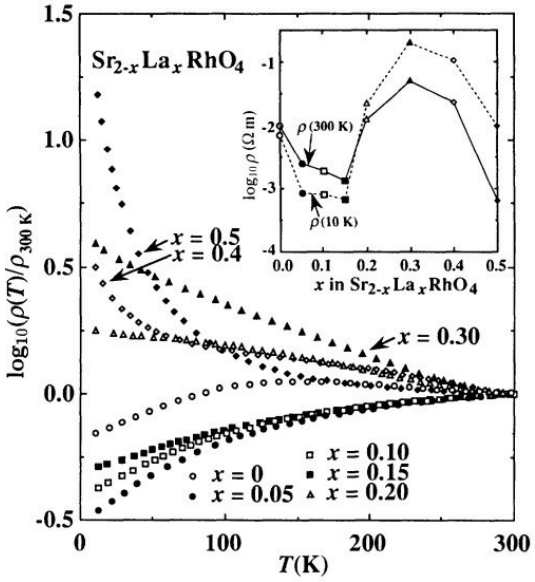

Figure 3.7: Polycrystal resistivity measurement of SLRhO [46]

ever, the DMFT calculation result in the Figure 3.8 suggested the metallic phase without significant change of the Fermi surface, and predicted the itinerant fer-

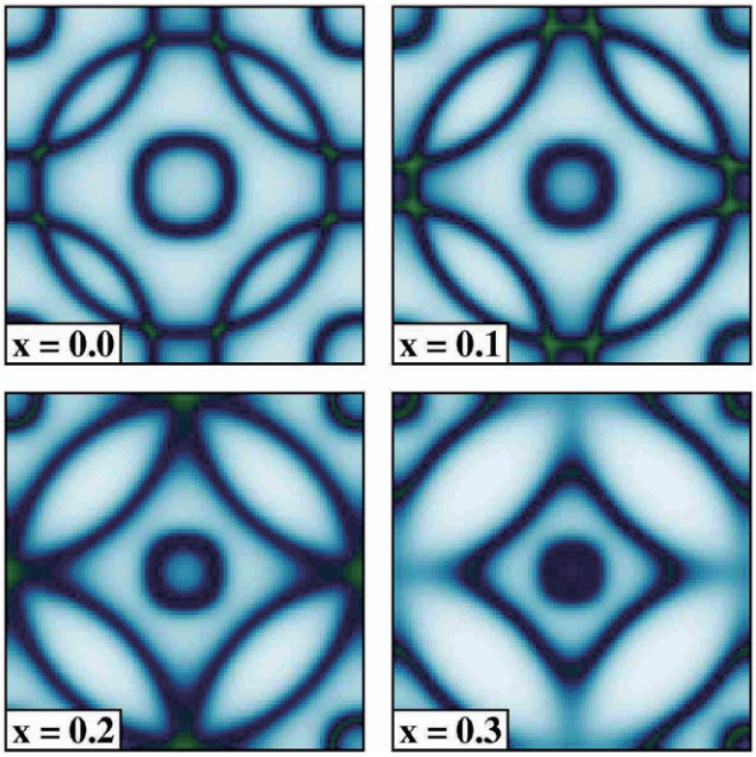

Figure 3.8: DMFT calculation of SLRhO [47]

romagnetism. The study to reveal the intrinsic electronic property of the SLRhO system would be necessary to understand the true physics of electron doped SRhO.

3.2 Experimental results

3.2.1 Sample growth

To investigate the intrinsic property of the electron doped SRhO, doping dependent fine single crystal is grown. Within the A_2BO_4 type chemical formula of SRhO, the major electronic contribution comes from the B site atom, the Rh, and octahedral oxygen arrangement. Therefore, to avoid the side effect of altering the electronic property by substituting the B site atoms (e.g. change of SOC, Coulomb U and etc.), the electron doping is implemented by A site substitution.

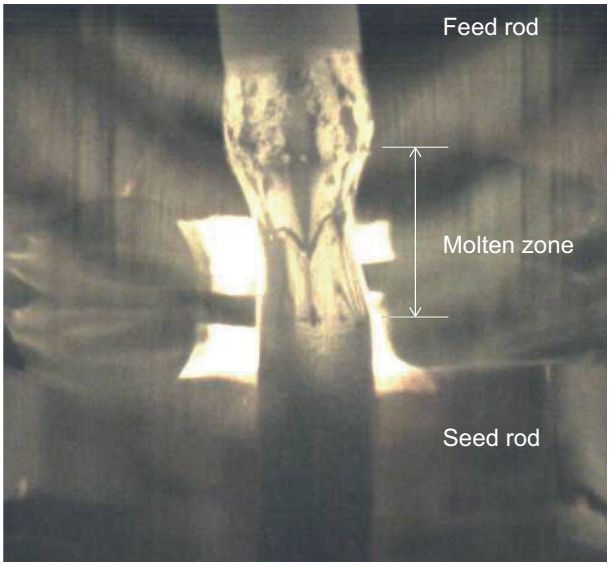

Figure 3.9: Floating zone growth of SLRhO

The La is used as a dopant, since the La has the closest radii to Sr.

Single crystals of SLRhO are achieved by the floating zone method. A single crystal of the similar system (SRO) can also be grown with floating zone method. However, there are two major problems when growing the SLRhO. One is the high volatility of the Rh_2O_3, and the other is the unstable oxidation number of the Rh atom.

First, the volatility is significant while melting the rod during the growth. The high temperature more than 2000 °C is required to melt the SRhO polycrystal rod, and it leads to the high volatility of Rh_2O_3 during the growth. Hence, it is necessary to add excess amount of Rh_2O_3 when forming a polycrystal rod to prevent the lack of Rh during the floating zone growth. To overcome the problem, 6% excess Rh_2O_3 from the stoichiometry is added to compensate the volatility.

The ground powder is, first, calcinated with 1100 °C and sintered after thoroughly grinding with 1200 °C. The polycrystal is again thoroughly ground and tubed to make about 5.5 mm diameter rod and it is pressed with 350 kg/m^2 with water pressure. The rod is again sintered with 1300 °C to harden the rod. The

Figure 3.9 shows the floating zone growth showing seed rod and feed rod attached with the molten zone. The diameter of the seed rod, the grown crystal, is smaller than the feed rod, which may because of the higher Rh_2O_3 contents in the feed rod and evaporation before become crystal.

Second problem appears during the floating zone growth. The stable oxidation number of Rh is not favorable to grow perovskite systems. To create perovskite materials, B site atoms should form +4 oxidation state, which may form BO_6 octahedrons with sharing points. Ru has stable oxidation state with +4 oxidation, however the Rh is stable with +3 oxidation number. Therefore, the RhO_6 octahedron structure would be easily broken and may include O deficiency. Therefore, during the floating zone growth, the rod is placed under 10 atm of 99.999% O_2 environment. The high pressure of the oxygen forces the Rh to form +4 oxidation number, and reduce the lack of oxygen. Furthermore, the grown single crystal is annealed after growth under O_2 flow, to match the stoichiometric oxygen contents. The annealing temperature is set to 1100 °C for all samples which is common annealing temperature for SRhO [42].

The resulting single crystal showed typical quasi-2D layered crystal behavior, where the cleavage along the ab-plane is much easier than along other perpendicular planes. The Figure 3.10 shows the cleaved surfaces of the single crystals for selected compounds.

3.2.2 Transport measurements and MIT

The resistivity measurement of the single crystal is done with 4-probe method with physical property measurement system (PPMS, Quantum Design). The measured data in the Figure 3.11 shows a doping dependence of the resistivity. The figure shows that the lanthanum doping gradually increases the resistivity. The

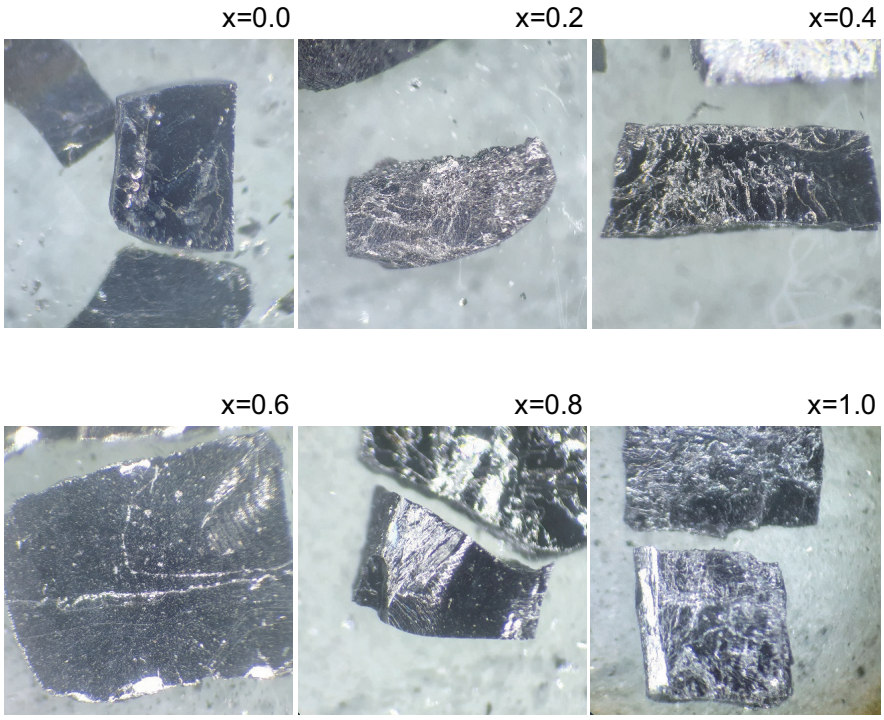

Figure 3.10: Single crystal SLRhO

slope of resistivity around 300 K has transition around $x = 0.4$ which indicates the metal to insulator transition. The insulating compounds with $x > 0.5$ shows clear negative slope of resistivity even at the 300 K. However, no anomaly that can used to infer the origin of the MIT.

Magnetization is also shown in the Figure 3.12. The figure shows the doping dependent magnetization, where the SRhO shows clear Pauli paramagnetic behavior, which is consistent with the Figure 3.2 from the previous research. The noticeable change is the gradual transition of the magnetization from Pauli-type to Curie-type paramagnet, by showing the near $1/T$ behavior of the temperature dependence at $x = 0.8$. The difference between the Pauli type and Curie type may reflect the change of the electronic property, where the itinerant behavior commonly results in the Pauli type paramagnet and localized moments shows Curie type behavior. Therefore, the magnetization may imply the localization of the electrons, which is consistent with the resistivity result. However, the mag-

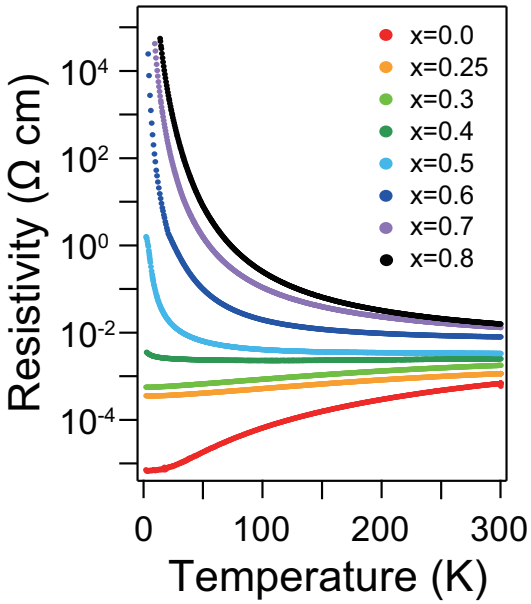

Figure 3.11: Single crystal resistivity measurement of SLRhO [48]

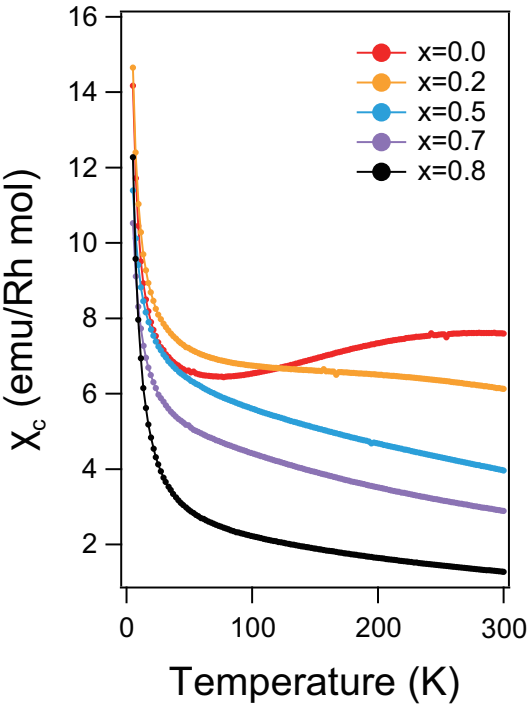

Figure 3.12: Single crystal magnetic susceptibility measurement of SLRhO

netization also does not show any anomaly as in Figure 2.15, hence, the origin of the MIT is still unclear. Hence, the electronic structure study would be necessary to reveal the band evolution around the MIT.

3.2.3 Electronic structure analysis

In order to find the mechanism of the MIT in SLRhO, the corresponding electronic structure is measured with ARPES with synchrotron facility. The photon energy of 70 eV is used for all experiment, while controlling the temperature around 30 K for improving the data quality. All experiment is performed under ultra-high-vacuum chamber below 5×10^{-11} Torr. The measurement is performed on the freshly cleaved surfaces in the chamber.

Figure 3.13 shows the doping dependence of electronic structure. In Figure 3.13(a) shows the Fermi surface of SRhO, the $x = 0.0$ compound. The system contains two different electron pockets, α and β, which is consistent with the previous studies [43]. The α band is a hole like band centering at the Γ point, which is indicated with green dashed line on the energy momentum distribution in the Figure 3.13(h). The β band, also centering around the Γ point, shows electron like band dispersion. Correspondingly. the β band dispersion can be shown in the Figure 3.13(h) with yellow dot line. Brillouin zone (BZ) is constructed as the red line in the Figure 3.13(a).

Over the whole doping range, because of the excess electrons provided by each La atom, the α band shows rigid-band-like shift. From Figure 3.13(h–k), α band gradually moves downward along energy. After critical doping level $x = 0.4$, the α band top is located right below the Fermi level, indicating the Lifshitz transition of α around $x = 0.4$. Even after the α band sink below the Fermi level, the band continuously shifts downward. The evolution of the α band does not show band renormalization.

The β band, on the other hand, shows anomalous doping dependent behavior. Before the MIT, the Figure 3.13(h-k) shows the β band gradually showing a rigid-band-like shift, resulting slight expansion of the Fermi surface volume in

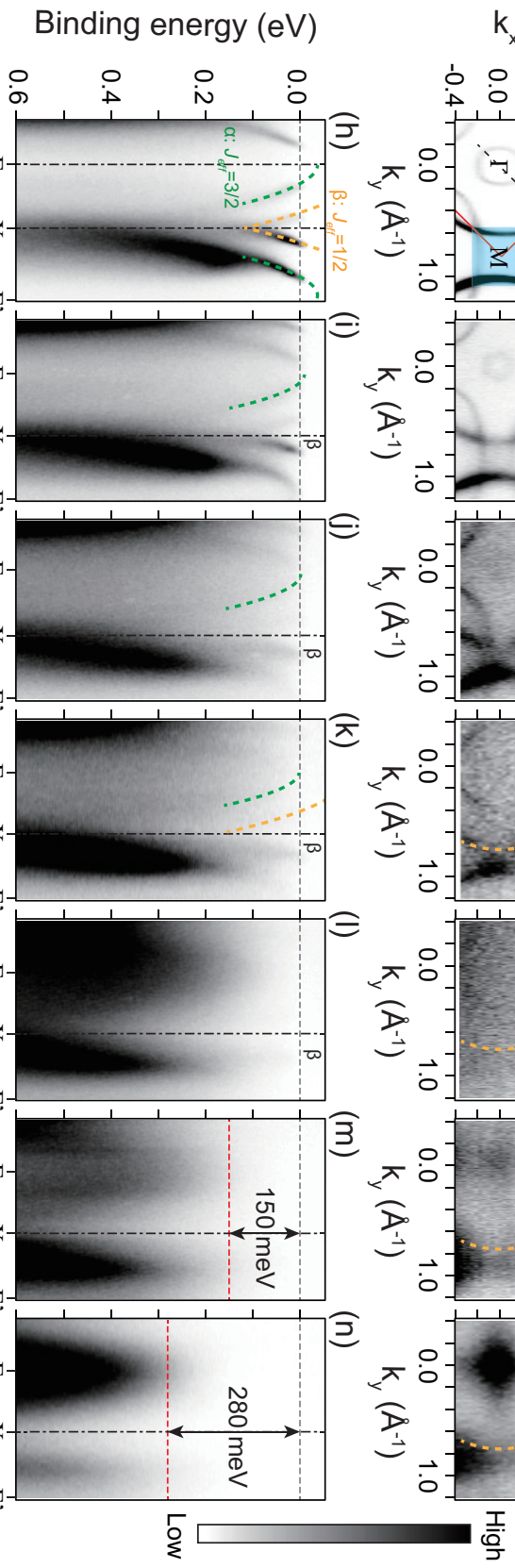

Figure 3.13: Doping dependent electronic structure of SLRhO [48]

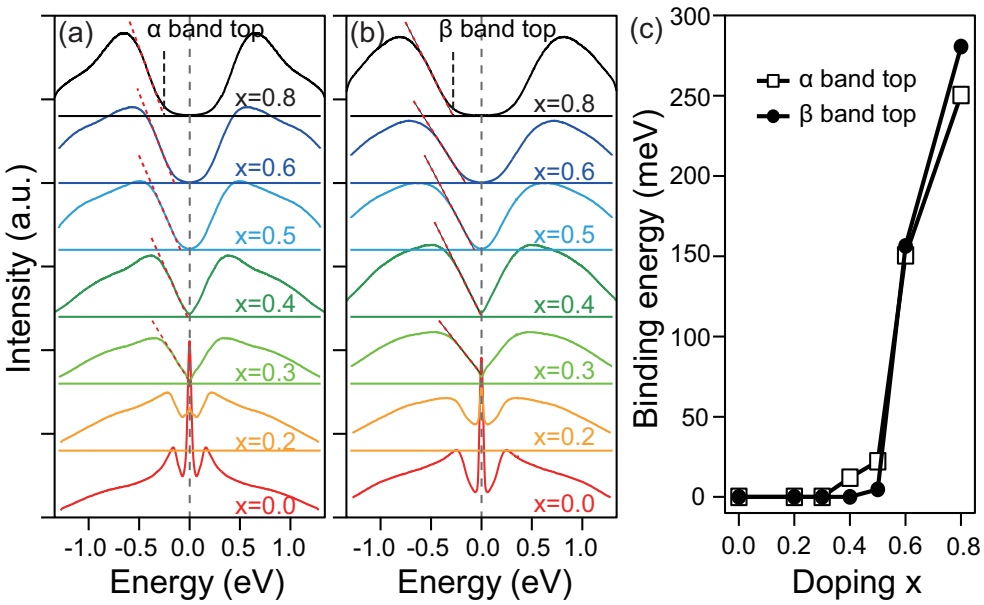

Figure 3.14: Band dependent integrated band distribution curve and estimated band top positions [48]

the Figure 3.13(a-d). At $x = 0.4$, the critical doping level, the β band spectral weight on the Fermi level suddenly become very weak. At $x = 0.5$, the spectral weight on the Fermi level clearly disappears, which is shown with empty Fermi surface in the Figure 3.13(e). Unlike α, the evolution of the β cannot be explained by the simple electron doping effect, implying a band renormalization with MIT.

The Figure 3.14 shows qualitative doping dependence of each band. The Figure 3.14(a) and (b) shows energy distribution curves (EDCs) of each band achieved by integrating the blue shaded areas of Figure 3.13(a). The upper shaded area shows only α band character and the lower shaded area would show only β band character near Fermi level. To eliminate the Fermi-Dirac dispersion around the Fermi level, which hinders to study the true spectral weight of the bands, the EDC data intensity $I(E - E_F)$ is symmetrized by taking sum of the $I(E - E_F)$ and $I(E_F - E)$. Hence, investigating the doping dependent spectral weight in the Figure 3.14(a) and (b) would provide the evolution of the insulating gap.

It is clear that the α band shows a gap starting from the $x = 0.4$, since the

α sinks below Fermi level starting from the $x = 0.4$. The β also shows clear gap feature starting from the critical doping, $x = 0.4$. It is noticeable that the gap formation of each band starts at the same doping level, $x = 0.4$. The Figure 3.14(c) shows the band top position from the linear fitting of the leading edge (red dot line on Figure 3.14 (a) and (b)) for each EDC. Even though the mechanism of the MIT of each band is different, the two bands start to create a gap at the same doping level. It implies that the MIT of β possibly be related to the α Lifshitz transition.

Moreover, the band gap of the β is robust under the further charge doping. The gap does not collapse from the further La substitution, and it even expands to become larger than 250 meV. This behavior does not appear in normal insulating phase, where the charge doping immediately occupies the conduction band above the Fermi level, and allow the transport. Hence, a proper new model is required to understand the MIT of the β band.

3.3 Mechanism of the MIT

Understanding the mechanism of the β band MIT is necessary to fully understand the SLRhO's MIT. However, it is not easy since the resistivity data in the Figure 3.11 and magnetization data in the Figure 3.12 shows no noticeable anomaly that may trigger the MIT. One may consider few more candidates.

Most simple parameter to consider is an electron number. The even electron number would show fully occupied band insulator, and the odd number electron number possibly shows a correlation driven Mott phase or Pierl's instability from superstructure. However, it is unlikely for the SLRhO MIT, since the MIT occurs at non-integer occupation. At the critical doping level ($x = 0.4$) the β electron

number is 1.4e, which does not fully occupy a band to apply the normal band insulator theory. Also it cannot be a Mott phase, which requires odd number electron filling. No commensurate order may derive 1.4e occupation insulator phase, which also can be supported by resistivity and magnetism study without anomaly.

The structure can be another candidate to trigger the MIT. The SRhO has a rotation distortion of octahedron along the c-axis. Since the crystal radius of La in SLRhO is smaller than that of Sr, the lattice may experience chemical strain to have further distortion. Indeed, the tolerance factor of x=2.0, the virtual end compound La_2RhO_4, is 0.983, which is much less than that of SRhO which has tolerance factor of 1.012. The simple calculation indicates that the La doping would give more distortion to the system where tolerance factor near 1 would have less distortion of octahedrons. The study of layered perovskite crystal symmetry with distortion suggests that the larger chemical pressure on SRhO may provide tilting distortion, which creates a displacement of the apical oxygen out of the c-axis.

However, the tilting distortion would not trigger the MIT in SLRhO. The Figure 3.15 shows the virtual band structure of SIO, with considering the rotation and tilting distortion. The figure shows that the band dispersion drastically changes with rotation distortion along the (001) axis and this would give the band dispersion similar to SRhO, which is isostructural and isovalent to SIO. Further calculation shows the tilting distortion along the (110) axis. The result on the Figure 3.15 shows that the band dispersion does not change much from the rotation-distorted band dispersion and does not seems to be more MIT favorable, which may require change of the bandwidth. The theoretical result would exclude the structure transition as a trigger to the MIT.

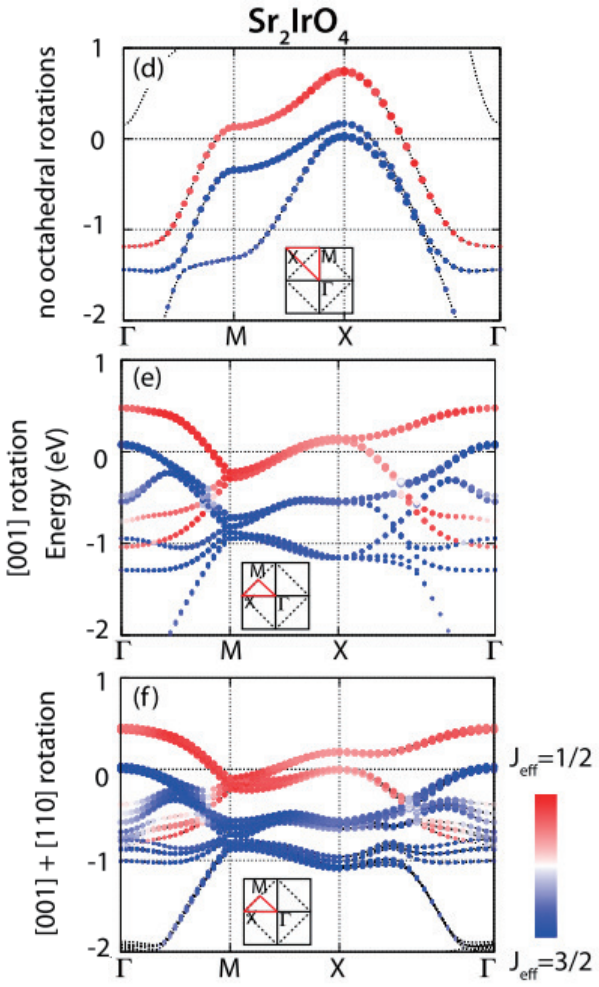

Figure 3.15: Structure dependent LDA+SOC calculation of SIO [49]

The robustness of the MIT under the charge doping also can hinder understanding the mechanism. The Figure 3.14(c) shows that, even after the critical doping $x = 0.4$, the insulating gap of SLRhO does not collapse from the further electron doping, and even shows an increase of the gap. The ordinary band insulator and Mott insulator would show unstable insulating phase under charge doping, which often results in a narrow region of insulating phase in the doping dependent phase diagram [50].

Therefore, one would doubt the disorder effect as a simple explanation. In many doped systems with disorder effect shows strong localization of the electrons, which is called Anderson localization. The La indeed would provide a dis-

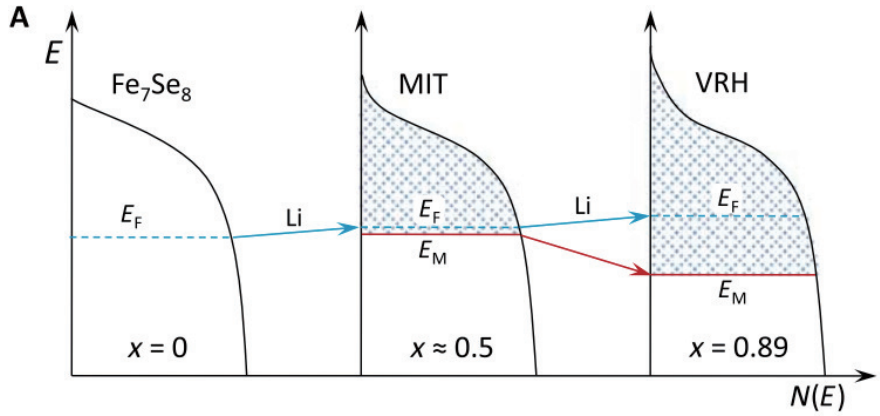

Figure 3.16: Band evolution of Anderson localization in $Li_xFe_7Se_8$ [51]

order effect since it may randomly drive lattice distortion by substituting the Sr atoms. However, the spectroscopic study on the Anderson localization strongly against the idea that SLRhO has merely disorder driven MIT.

The Figure 3.16 shows the example of the strongly localized disordered system, $Li_xFe_7Se_8$ with schematic description of its band. Li intercalation in the Fe_7Se_8 provides two major changes. First, the Li provides electron to the system, and second, it induces the distortion of the crystal structure. The random site occupation of the Li atom brings strong disorder effect to the system. Hence, the doping induces the random potential distortion and broadens the band as describe on the middle panel, which is represented by the elongated tail of the band edge. Starting from the edge, where the energy state of the most distorted sites exist, the localized state appears as the potential distortion hinders the electron hopping. The Figure 3.16 indicates the localized states by shade, where the mobility edge E_M distinguishes the localized and delocalized states. On the other hand, the electron doping from Li raises the E_F, the Fermi energy. At Li contents over 0.5, the E_F passes the E_M and the electron on the Fermi level would become localized. This would bring the disorder driven electron localization, the Anderson localization.

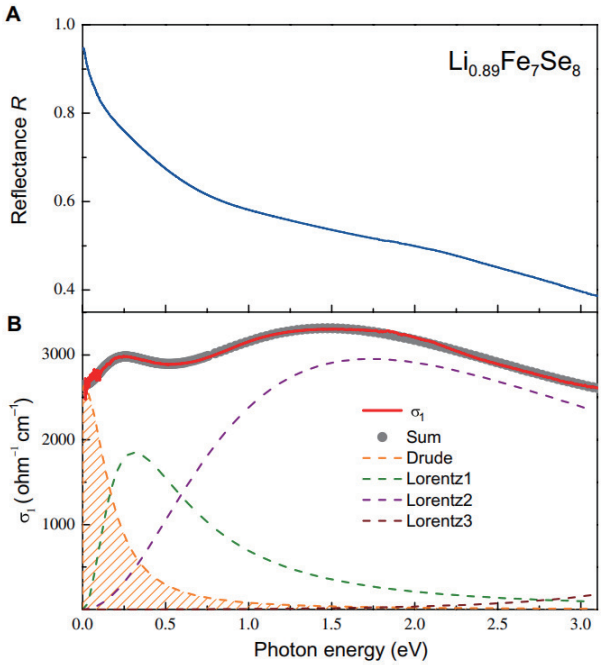

Figure 3.17: Reflectance and optical conductivity of Anderson insulator $Li_0.89Fe_7Se_8$ [51]

The schematic analysis would suggest there would be no significant band change in the electronic structure, however, the character of the state would be changed from itinerant to localized. It is notable that the Anderson localization does not create a band gap, even though the system becomes insulator, which would leave finite spectral weight on the Fermi level. This can be confirmed with the spectroscopy result in the Figure 3.17, showing the optical spectroscopy measurement. The measured optical conductivity indicates that the zero energy excitation exits, which implies the states, indeed, exists on the Fermi level.

The study on graphene with the H deposition would be a direct example of the finite spectral weight on the Fermi level via ARPES experiment. In the Figure 3.18, the system become insulator since the H deposition induces the disorder, however, the system does not show any gap, but the broadening of the band structure, which is the result of the random distortion of the potential from disorder. Therefore, the clear gap formation of the insulating SLRhO cannot be

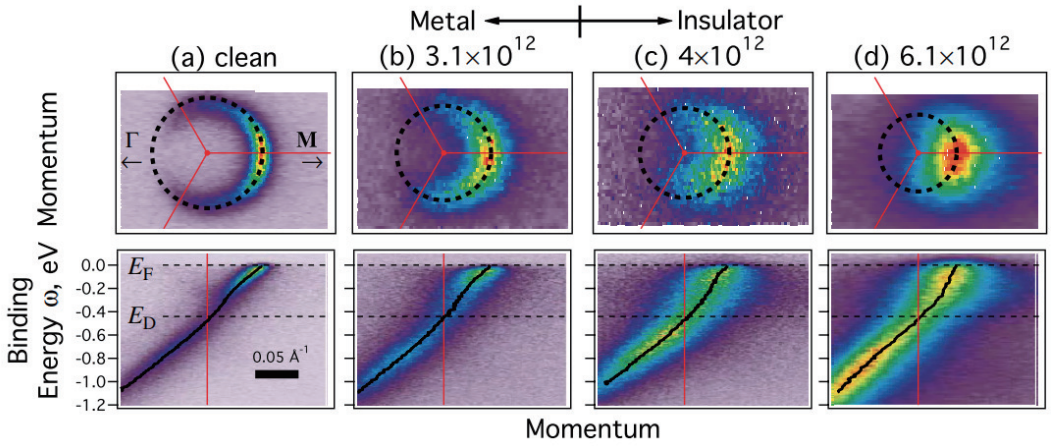

Figure 3.18: H dosing dependent Anderson localization of graphene shown by ARPES [52]

soley explained by the disorder effect. Then, what can trigger the gap of the SLRhO?

The electron-electron correlation to be a possible candidate triggering the gap. The Efros and Shklovskii introduced a concept of "Coulomb gap", which suggests the electron-electron interaction can derive a gap in strongly localized disorder system [53, 54]. The Coulomb gap may occur when the electrons in each strongly localized state have the long-range Coulomb interaction with each other, creating Mott-like correlation driven gap on the Fermi level. Hence, the Coulomb gap suggests the correlation gap in any electron number system, as long as the electrons are strongly localized by disorder.

Furthermore, the theorists introduce the Anderson-Hubbard model, in order to quantum mechanically model the disordered & correlated system. By expanding the correlation based Mott-Hubbard model with disorder effect, the Anderson-Hubbard Hamiltonian can be written as

$$H = -t \sum_{<i,j>\sigma} c^{\dagger}_{i\sigma} c_{j\sigma} + U \sum_{i} n_{i\uparrow} n_{i\downarrow} + \sum_{i\sigma} W_i n_{i\sigma} \tag{3.1}$$

where $c^{\dagger}_{i\sigma}(c_{i\sigma})$ is the creation (annihilation) operator for electron at site i, σ the spin, t the hopping between the nearest-neighbor sites, $n_{i\sigma} = c^{\dagger}_{i\sigma} c_{i\sigma}$ a local

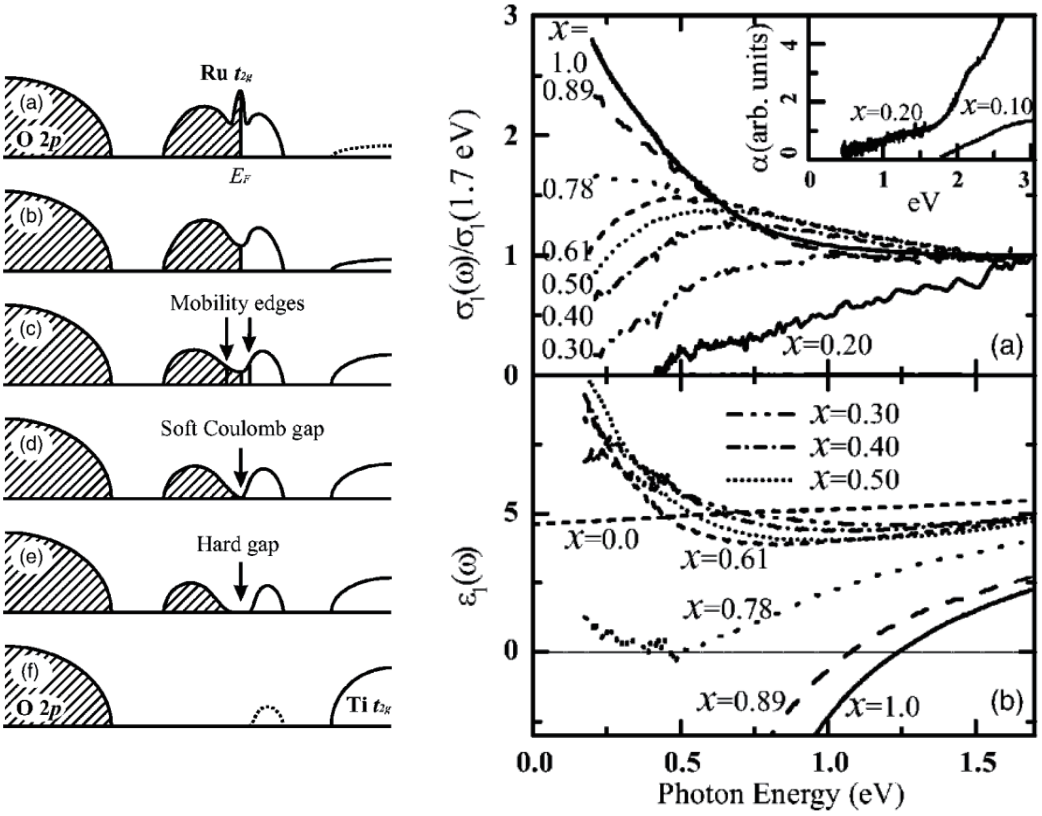

Figure 3.19: Schematics of the band structure of $SrTi_{1-x}Ru_xO_3$ (left) and the optical spectroscopy results (right) [55]

electron number operator at site i, U the on-site Coulomb repulsion energy and W_i a random potential energy at each site [55]. Even though the Hamiltonian is not easy to be utilized in the band calculation, the concept of the Coulomb gap and Anderson-Hubbard model introduce new physics driven by correlation in a non-integer electron number, with help of the disorder.

Many systems are considered to be possible candidate of such disordered & correlated insulator. The Figure 3.19 shows the example of the $SrTi_{1-x}Ru_xO_3$ system, where the MIT occur on $x = 0.4$ and remains insulating at $x < 0.4$ [55]. The optical conductivity in the right panel Figure 3.19 would infer the Fermi level spectral weight by extrapolating the data toward the 0 eV photon energy. From the data the spectral weight is almost zero at $x = 0.4$ and gap is formed at $x < 0.4$. Such band structure is schematically displayed on the left panel of

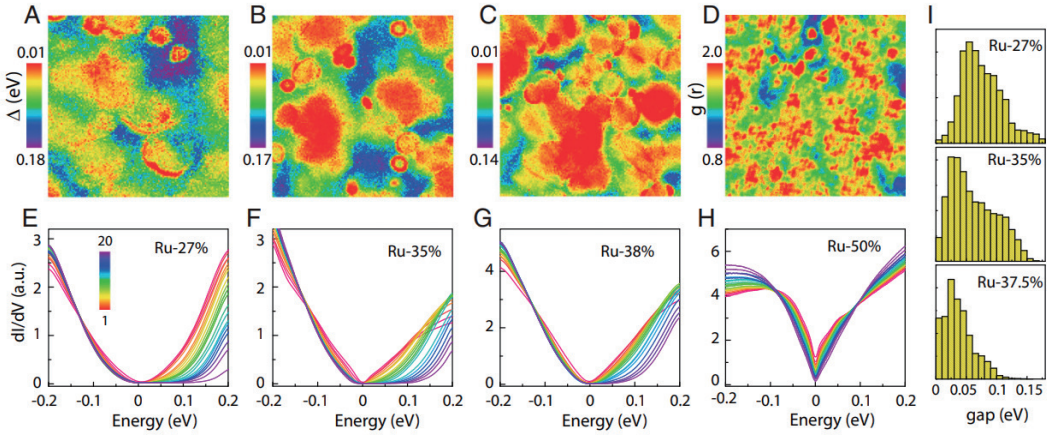

Figure 3.20: Tunneling spectroscopy of $Sr_3(Ir_{1-x}Ru_x)_2O_7$ [56]

the Figure 3.19. The study suggests that the role of Ti is two folded. One is the disorder effect that would localize the states, and the other is the increase in correlation. The study showed that the $x = 0.5$ shows finite spectral weight on the Fermi level, but insulating when measure the resistivity, which is corresponding to (c) of the left panel of the Figure 3.19. Further doping would start to create a gap, due to the correlation, which is starting from the $x = 0.4$. The gap shows same robust behavior to the system as it did in the SLRhO.

The scanning tunneling spectroscopy (STS) study on $Sr_3(Ir_{1-x}Ru_x)_2O_7$ in the Figure 3.20 also shows a properties of the disordered & correlated insulator. The $Sr_3Ir_2O_7$ is well known as a $J_{eff} = 1/2$ Mott insulator. The Ru doping on the system would provide the hole doping, and would collapse the Mott insulator property. However, the STS study showed that the system has the insulating phase even at the half substitution of the Ir site. Furthermore, the gap dispersion along the energy showed "cusp" of the density of states, which is predicted from the theoretical research of the disordered & correlated insulators [53, 54].

The remaining question is what can change the correlation effect to induce the Coulomb gap. This thesis takes a Lifshitz transition of the α band as a clue. The Figure 3.21 shows the schematic band structure of the SLRhO. At the

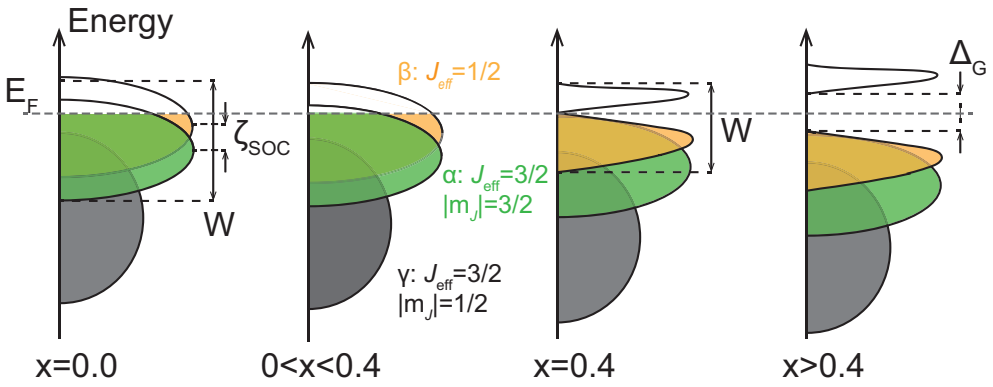

Figure 3.21: Schematic band structure of SLRhO [48]

non-doped SRhO system, the α and β are split due to the SOC. Since the 4d transition metal system has smaller SOC compared to 5d system, the α and β band split is not large enough to fully split the bands. Hence, both of the bands are partially unoccupied. The electrons in α and β bands both can have contribution to hopping from one site to nearby site, which would define large bandwidth including both of the bands as indicated on the Figure 3.21. As electron is doped into the system, the α become fully occupied, and the electron transport be solely originated from the β at the $x = 0.4$. At that point, the bandwidth of the system would solely be defined by the conduction band β, and the system would have much weaker hopping rate. This bandwidth transition from the α band Lifshitz transition may change the transport of the system and enlarge the effective correlation U/W as the SOC did with the narrow $J_{eff} = 1/2$ band in the SIO. Hence, the β band may have strong correlation effect above the critical doping level $x = 0.4$.

With help of the ARPES band evolution analysis, the above analysis emphasizes a role of α band Lifshitz transition in the MIT of the SLRhO. However, it is not easy to prove the solid contribution of the Lifshitz transition to enhance correlation. Due to correlation driven broadening of the bands, the ARPES experiment cannot clearly define the bandwidth. Also, the theoretical modelling is

challenging since the Anderson-Hubbard Hamiltonian contains random potential distortion, which requires enormous computing power. To support the relation between the SLRhO MIT and the Lifshitz transition, further experimental evidence would be necessary.

3.4 Confirmation of Lifshitz transition triggering the MIT

The SLRhO study showed the novel MIT possibly triggered by the Lifshitz transition. The suggested disorder & correlation driven MIT mechanism implies that the Lifshitz transition may trigger the MIT without relation between the critical electron number. One may construct experiments with changing the parameters to alter the critical doping level. If the SOC is changed by substituting the Rh with Co or Ir, the MIT would still exist, but with a different critical point, since the band split of the α and the β can be changed by the SOC variation. Also, the change of the element in Sr site would change the critical doping level. The element such as Ce would provide different electron doping rate to the system. This section introduces Ce driven MIT instead of the La, in order to support the relation between the Lifshitz transition and the MIT.

The Ce would bring two different parameters compared to SLRhO. First, the electron provided by the Ce would be changed. The Ce has one more electron compared to La, the electron doping ratio per atom can be different from the La substitution. Moreover, the disorder triggered by Ce can be different from the La atom. The crystal radii of the Ce and La is different, hence, the atomic distortion triggered by Ce is different from that of La. Hence, the study on $Sr_{2-x}Ce_xRhO_4$ (SCRhO) may alter the critical doping rate of the Lifshitz transition, and whether the critical doping of MIT follows or not can support/disprove the relation be-

tween the Lifshitz transition and the MIT.

The Ce substituted single crystals are achieved by the same growth method with SLRhO using floating zone furnace. Total 6 doping concentrations (x =0.0, 0.1, 0.15, 0.2, 0.22, 0.25) are successfully grown with the floating zone method, however due to chemical miscibility, further doping produced CeO_2 cluster instead of globally homogeneous Ce doping.

From the ARPES result, the band evolution may show clear resemblance between the SLRhO band structure. In the Figure 3.22(g-l), the α band is tracked by the parabolic function fitting, which are indicated by dashed lines. Indeed, the Lifshitz transition occurs by rigid-band-like shift of the α at $x = 0.2$. On the other hand, the β band shows clear disappearance on the Fermi surface around the $x = 0.2$. The ARPES result suggests that the critical point of the α band Lifshitz transition is changed from $x = 0.4$ (in the SLRhO) to $x = 0.2$, with still showing the coincidence of the β MIT at the critical point. Hence, the Ce doping study would support that the MIT of the electron doped SRhO can be triggered by the Lifshitz transition.

Indeed, the transport measurement of SCRhO shows similar behavior with SLRhO. The Figure 3.23 shows the doping dependent resistivity that shows the MIT critical doping at $x = 0.2$, which is the half of the SLRhO case ($x = 0.4$). Considering that the Ce has one more electron compared to La, it is understandable that the Ce inducing the half critical doping rate. Hence, the resistivity also supports the Lifshitz transition driven MIT shown in the ARPES measurement.

Furthermore, considering the effect of disorder would emphasize the role of the Lifshitz transition. At the critical doping of SCRhO ($x = 0.2$) and the SLRhO ($x = 0.4$) the effect of disorder is different. The strength of the disorder effect may be estimated by comparing the doping driven Shannon crystal radii change

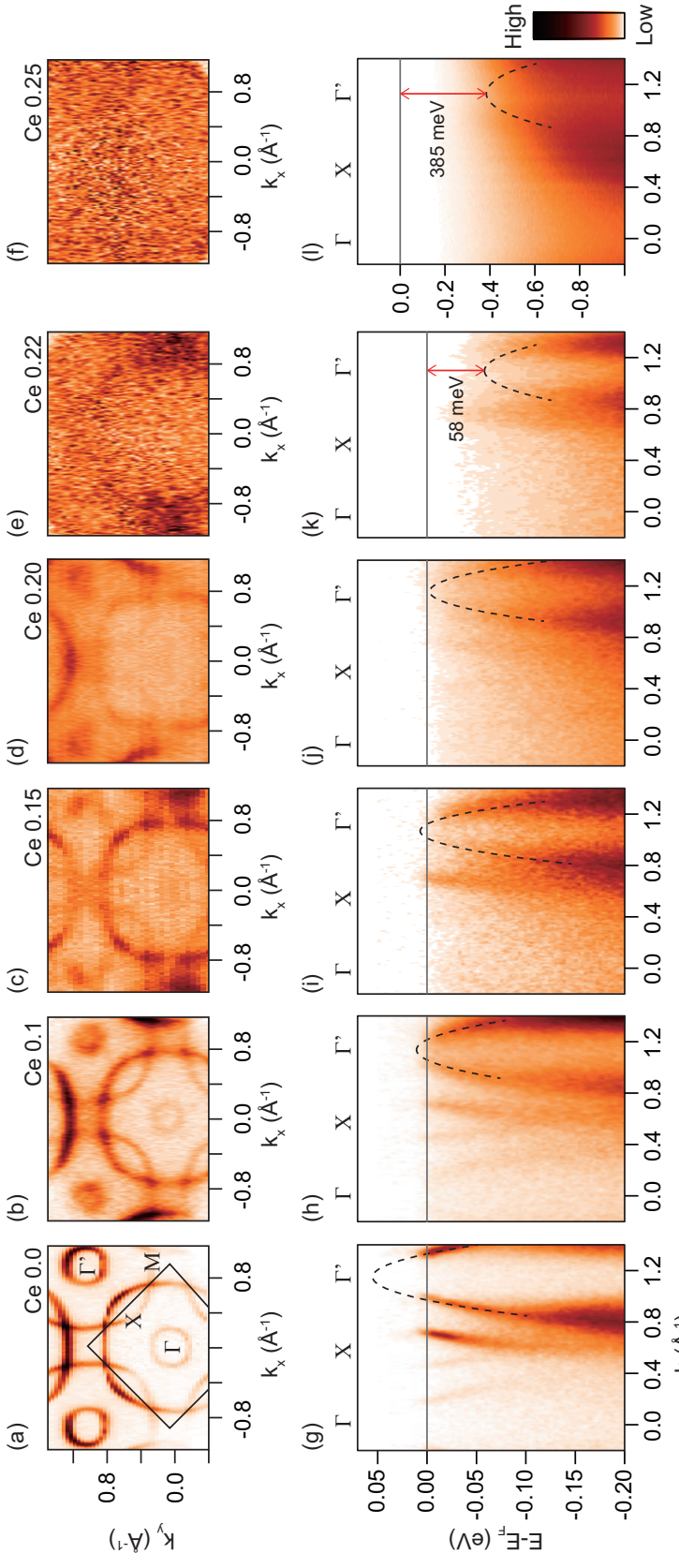

Figure 3.22: Doping dependent electronic structure of SCRhO

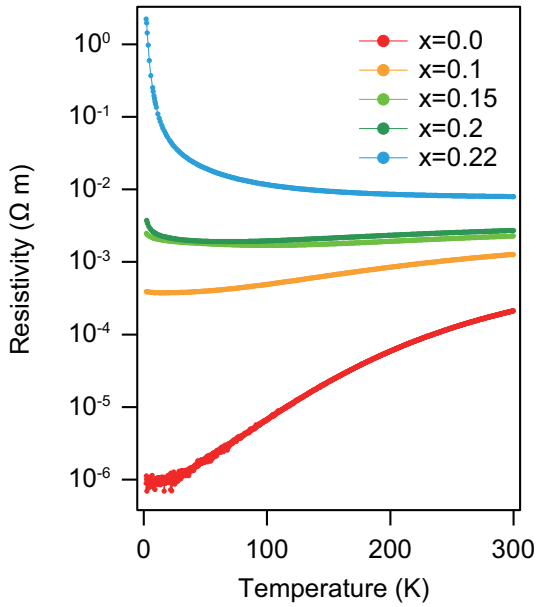

Figure 3.23: Doping dependent resistivity of SCRhO

on the Sr site. The Shannon radii of the Sr in the A_2BO_4 type structure is about 1.45 Å. On the other hand, the Shannon radii of the Ce is about 1.336 Å, while that of La is about 1.356 Å. Hence, the average A site radii of $x = 0.2$ SCRhO is about 1.4272 Å, while the average radii of the $x = 0.4$ SLRhO is about 1.4124 Å. Hence, the change of crystal radii is smaller for the Ce doping case, indicating less disorder at the critical point. The Lifshitz transition triggered MIT at even less disorder suggests that the disorder is not the governing parameter to achieve the insulating phase, but it only helps the system to have insulating phase.

The study of the SCRhO provides universality of the electron doping driven MIT in SRhO. The study supports that the Lifshitz transition may trigger the MIT with band structure analysis. The disorder effect may be required to localize the electronic states, however, the study on the SCRhO may indicate it cannot determine the critical doping of the MIT. The split between the α and the β determines the critical doping of the Lifshitz transition, hence, the critical doping of the MIT.

Hence, the relation between the MIT and Lifshitz transition implies an im-

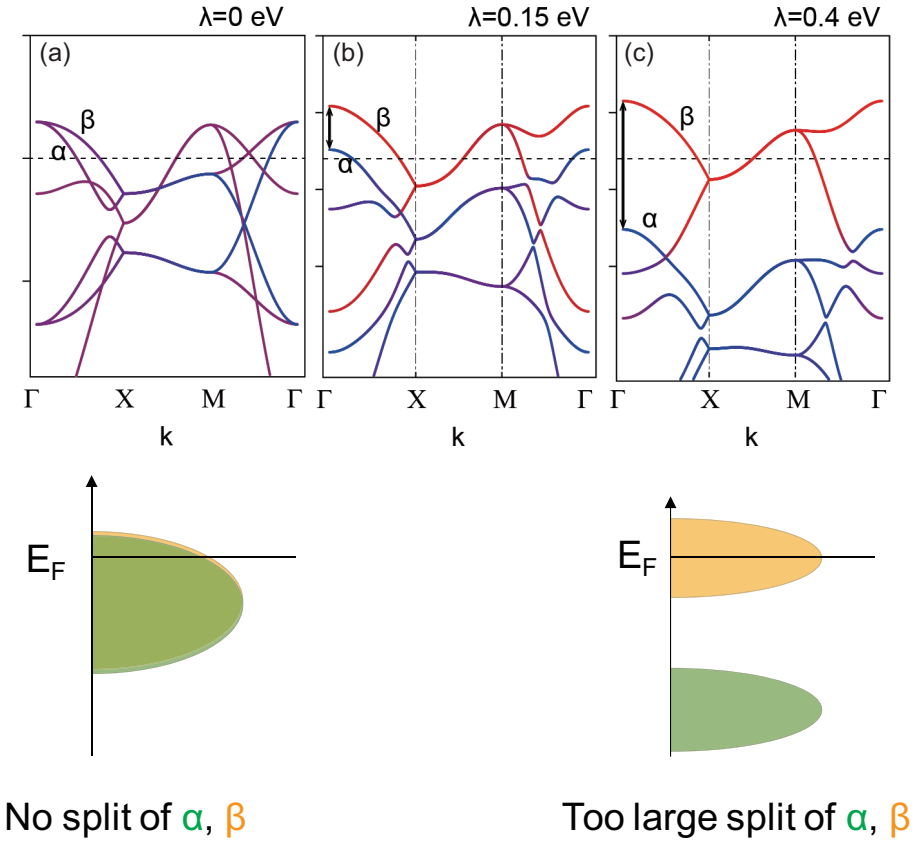

Figure 3.24: SOC dependent tight-binding calculation of SRhO

portant message. The Figure 3.24 shows the SOC dependent band structure of SRhO, calculated by tight-binding theory. The Figure 3.24(a) shows the zero SOC, which shows no split between the α and the β. Since the two bands are not split, the Lifshitz transition of α does not exist, hence, MIT cannot occur before full occupation of the two bands. If the SOC is too large, as in the Figure 3.24(c), the system split between the α and the β is too large, hence, the α band is already fully occupied and the β band is half filled, which would trigger the $J_{eff} = 1/2$ Mott phase as in SIO. Hence, only at the moderately spin-orbit coupled 4d SRhO would have the moderately split α and β to have Lifshitz transition driven MIT.

3.5 Conclusion

In this section the doping dependent electronic structure analysis on the 4d TMO SRhO discovered a new type of electronic property. The study revealed the possible relation between the Lifshitz transition, which is induced by the moderate SOC of the Rh atom, and the exotic insulating phase. The discovery of new 4d TMO physics would suggest important implications.

First, the study is a discovery of an exotic insulating state with unexpected properties that is not expected in ordinary insulator phase. The insulating phase in SLRhO is robust under charge doping and the size of a gap is approximately proportional to the doping rate. While the ordinary insulating phases are fragile under charge doping, charge doping in SLRhO does not break the insulating phase and the gap even increased gradually throughout the wide energy region. Furthermore, the Lifshitz transition of the SLRhO is not a specific property of the electron doped SRhO system, which implies that the study can be expanded to similar multi-band systems with split bands and anisotropy of the bands.

It is also notable that the MIT in SLRhO would acknowledge an effect of SOC in 4d TMO systems. The previous research of the SOC assumed an extreme limit, where the SOC is large enough to govern the system property. On the other hand, the 4d TMOs showed various exotic physical phenomena such as Van Vleck magnetism in Ca_2RuO_4 [57, 58], Hund metallic behavior in SRO [59–61], and Kitaev magnet α-$RuCl_4$ [62]. The study on electron doped SRhO MIT would assess the role of SOC in such phenomena, by showing an example of SOC-driven physics in 4d TMO system. Moreover, the doping dependent study on SRhO would be an initiating study of moderate SOC, which may lead to various novel physics driven by the SOC.

Chapter 4

Orbital selective doping effect in $Sr_2Ru_{1-x}Ir_xO_4$

Above study on the rhodate showed the properties of the moderately spin-orbit coupled system, where the SOC has a significant role to the major electronic property. In this chapter, via doping dependent study, the change of the SOC and its consequence to the band structure are introduced. The Ir doped SRO, the SRIO system, is the target material, where the 5d transition metal Ir substitution into the 4d Ru atom provides change of the SOC. From this chapter, a discovery of the SOC-driven orbital-selective doping effect in SRIO is introduced with thorough analysis of the phenomena with ARPES and tight-binding calculation.

4.1 Previous results

4.1.1 Sr_2RuO_4 and Sr_2IrO_4

The target material SRIO consists of two end compounds SRO and SIO. The both has layered perovskite structure, however, the two have very different properties. The SRO shows supereconducting metal state [63], and the SIO is an antiferromagnetic $J_{eff} = 1/2$ Mott insulator [7, 11]. Because of the uniqueness of each physical property, the two systems are exclusively and deeply studied so far.

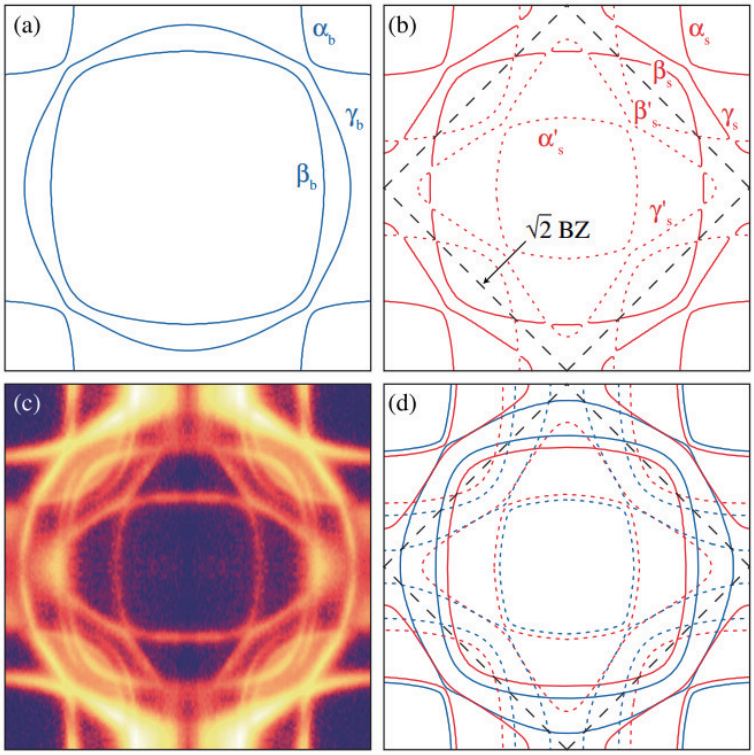

Figure 4.1: Electronic structure of SRO [64]

The superconductivity of the SRO has unsolved controversy, since the superconducting symmetry of the SRO is unknown [65–67]. It may due to the complex band structure of the SRO system. The SRO system consists of the three different band character near the Fermi level. The Figure 4.1(a) shows the three different Fermi surface of each band. The α and the β bands are mainly originated from the $d_{xz/yz}$ bands from the t_{2g} band of 4d orbital, and the γ band is from the d_{xy}. Because of the band character, the α and the β shows less-dispersive bands, which show almost straight line Fermi surfaces. On the other hand, the γ is highly dispersive band structure, showing circular shaped Fermi surface.

Unlike relatively simple bulk band structure, the surface band of the SRO is very complex. The surface layer of the SRO has structural distortion, which is well known by the low energy electron diffraction (LEED) and scanning tunneling microscopy (STM) as shown in the Figure 4.2. In the surface layer, the SRhO

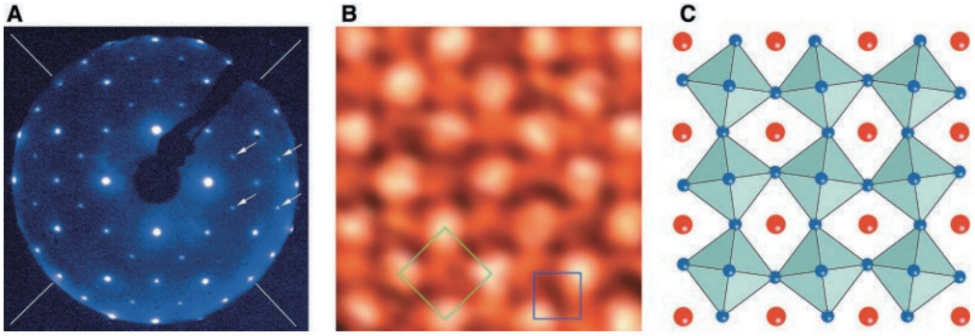

Figure 4.2: Octahedron rotation distortion on the SRO surface [68]

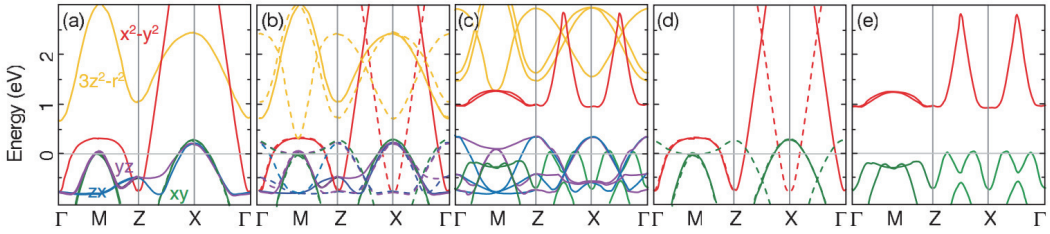

Figure 4.3: Octahedron rotation driven band renormalization [43]

like staggered octahedron rotation appears, which can be proved by the $\sqrt{2} \times \sqrt{2}$ superstructure peak in the LEED pattern (Figure 4.2(a)) and the unit cell doubling in the STM image. Because of the structure distortion, the band structure in the surface shows complex band renormalization.

The Figure 4.3 shows the octahedron rotation dependent LDA calculation study on SRhO system. The Figure 4.3(a) shows the band structure without any structure distortion. The Figure 4.3(b) shows duplicated bands considering the unit cell doubling (BZ reduction) from the octahedron rotation. The Figure 4.3(c) shows the final calculation result considering the octahedron rotation by including the hybridization effect between the duplicated bands and the original bands. The study reveals that the major band renormalization from the octahedron rotation comes from the band mixing between the d_{xy} band and the $d_{x^2-y^2}$ band [43, 69] which shows huge gap between the two as shown in the Figure 4.3(d) and (e).

As a result, the SRO surface band topology is not equal to that of the bulk band. The major difference appears on the γ band with large d_{xy} component,

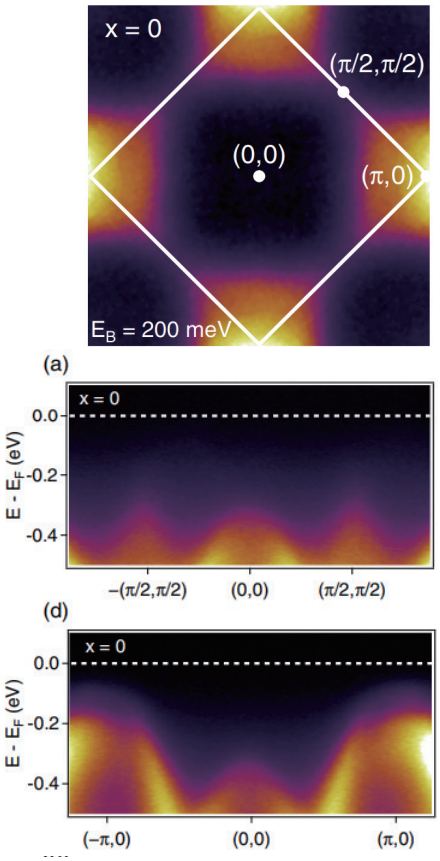

Figure 4.4: Electronic structure of SIO [8]

where the surface γ shows clover shaped Fermi surface centering on the center of the reduced BZ as shown in the Figure 4.1(b), which is very different from the bulk γ band with circular shape centering on the center of the original BZ. Moreover, the duplication of the α and the β band complicates the band structure further. Hence, the overall band structure of the SRO is highly complex, as shown with the ARPES measured Fermi surface data in the Figure 4.1(c), and the schematic description in the Figure 4.1(d).

On the other hand, the SIO shows insulating band structure due to SOC driven $J_{eff} = 1/2$ physics. The low bandwidth of $J_{eff} = 1/2$ band triggers a Mott phase even though the Coulomb U is small in 5d iridates. The band structure of the SIO is shown in the Figure 4.4. Since the SIO crystal structure is isostructural to SRhO, it already contains the octahedron distortion, showing

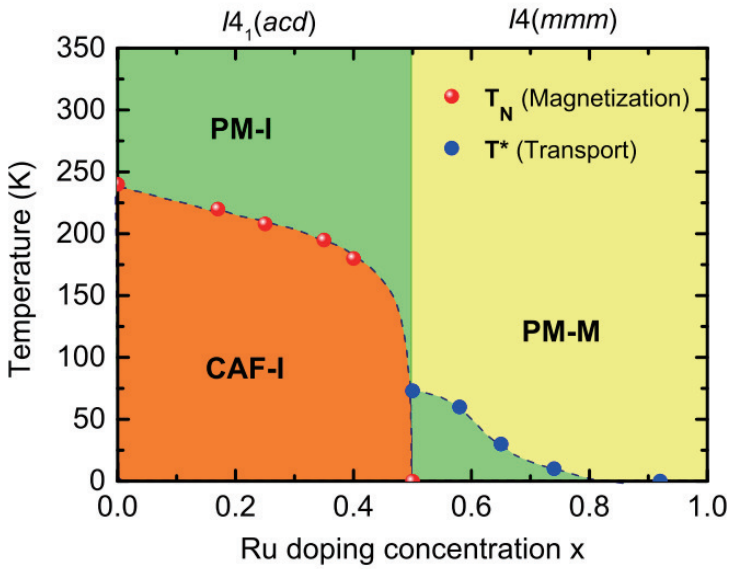

Figure 4.5: Phase diagram of SRIO [70]

$\sqrt{2} \times \sqrt{2}$ reduced BZ as for the surface of the SRO. Near the Fermi level, the two bands forms the insulating valence bands, which are $J_{eff} = 1/2$ bands and $J_{eff} = 3/2, |m_{J_{eff}}| = 3/2$ bands. The $J_{eff} = 3/2, |m_{J_{eff}}| = 1/2$ band is fully occupied, and the $J_{eff} = 1/2$ band is half filled to have Mott phase, as described from the previous chapter.

Since the end compounds have very different electronic properties, the studies on SRIO showed complex phase diagram as shown in the Figure 4.5. The magnetic transition from canted antiferromagnet to paramagnet occurs on Ir 0.5, as the temperature dependence of the magnetization is shown in the Figure 4.6. A MIT occurs at the same composition where the resistivity shows sign change of the slope at the high temperature region in the Figure 4.7.

To understand the mechanism of the complex phase diagram, one can consider three major parameters changing from Ir doping in the SRO: the electron number, octahedron rotation and SOC. It is clear that the electron would be provided by the Ir substitution. Transition metal in layered perovskites forms +4 oxidation state to form octahedrons, hence the Ru^{+4} would contain four valence electrons

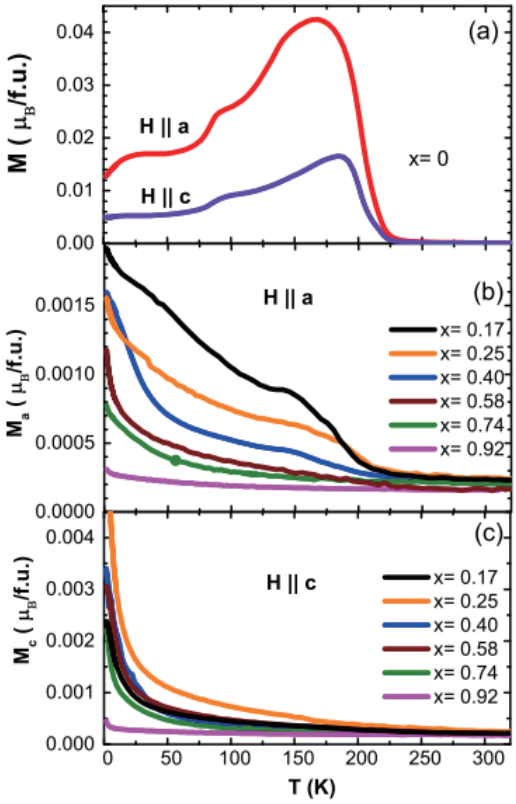

Figure 4.6: Magnetization of SRIO [70]

in the 4d t_{2g} band, while the Ir^{+4} would have five electrons in 5d bands. Hence, one may expect gradual increase of the electron number from the Ir substitution.

Structure transition is another parameter from the Ir substitution. Unlike the structure of the surface, the SRO crystal does not have octahedron rotation distortion. However, the SIO is isostructural to the SRhO, which has staggered octahedron rotation distortion. One may expect that the Ir substitution would provide gradual chemical pressure which would gradually change the octahedron rotation angle, as the Vegard's law expects linearly varying lattice constant from the doping. On the contrary, the SRIO shows abrupt change of structure around Ir 0.5. The Figure 4.8 shows the structure analysis of the SRIO system. The Figure 4.8(a) shows the Ir-O_1-Ir angle, where the O_1 is the oxygen atom within the ab-plane, hence, the angle indicates the existence of the rotation distortion. The octahedron rotation shows sudden appearance around the Ir 0.5, where the

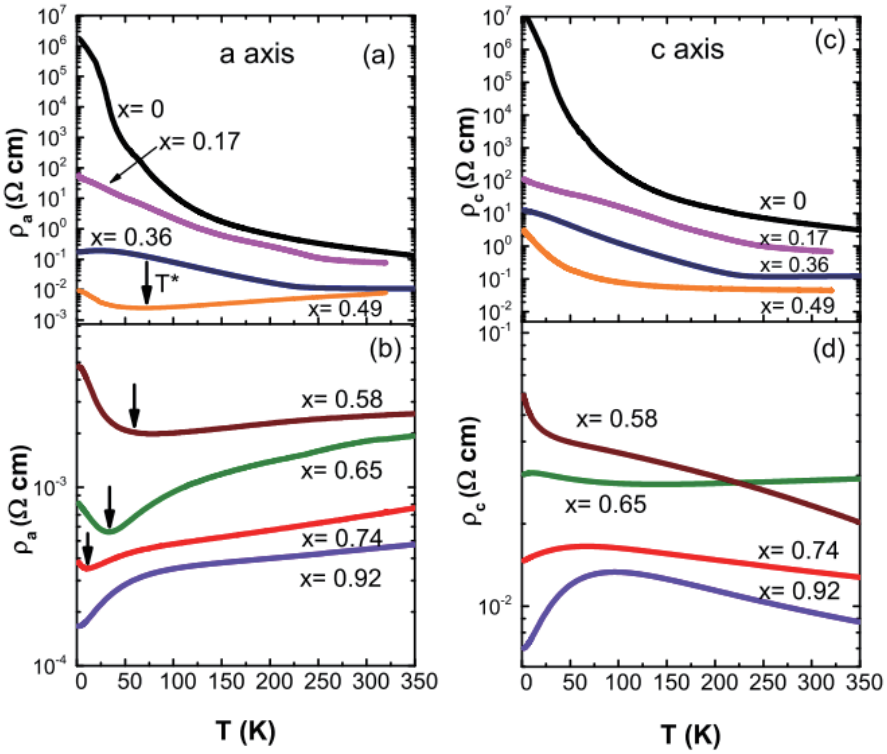

Figure 4.7: Resistivity of SRIO [70]

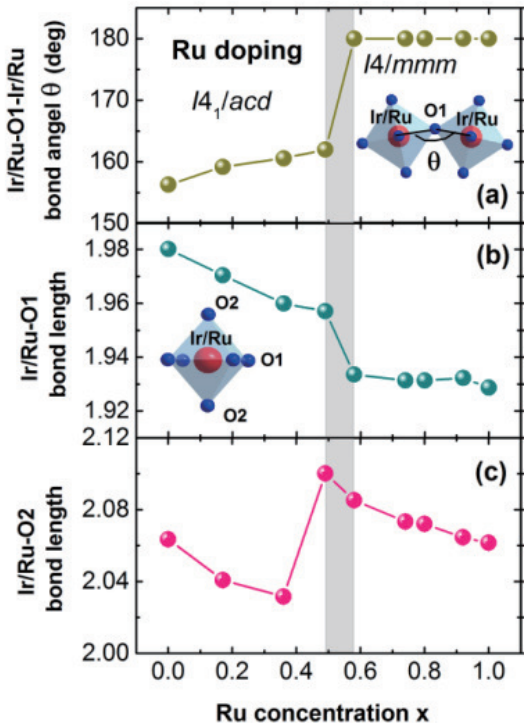

Figure 4.8: XRD analysis of SRIO [70]

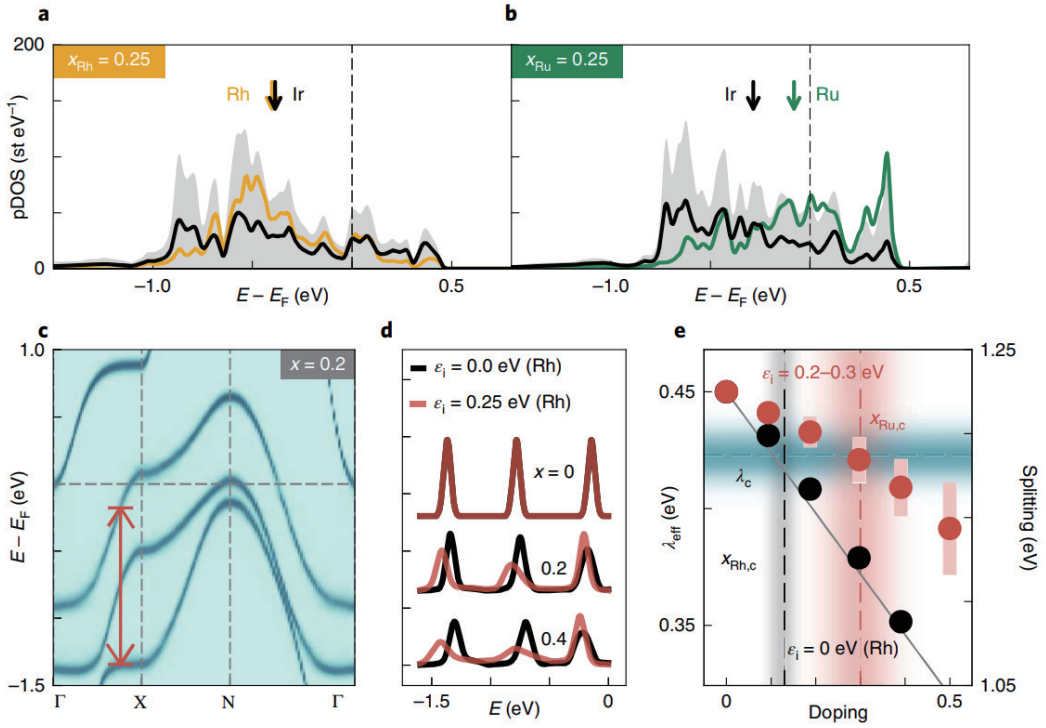

Figure 4.9: SOC estimation of Ru/Rh doped SIO [10]

compounds near Ru does not show any change of the angle from the 180 deg. Similarly, the Figure 4.8(b) and (c) shows similar first-order-like structure transition at Ir 0.5. Therefore, the structure dependent drastic electronic structure renormalization can be expected around Ir 0.5.

Last but not least, the SOC would be changed by the Ir substitution. The study of the doped SIO showed that the 4d transition metal (Ru or Rh) doping on the SIO would gradually change SOC. The Figure 4.9 shows the recent study on SOC estimation from the band structure. The DMFT calculation shows that the SOC would be varied by doping of the bands, which can be indicated by the SOC driven split of the bands (the red arrow in the Figure 4.9(c). The decrease of the SOC from the SIO would renormalize the band structure, which is shown with the collapse of the Mott gap from various studies.

Such complex parameter changes lead complex transitions of electronic structure, which is also expected by the complex phase diagram of Figure 4.5. Hence, it

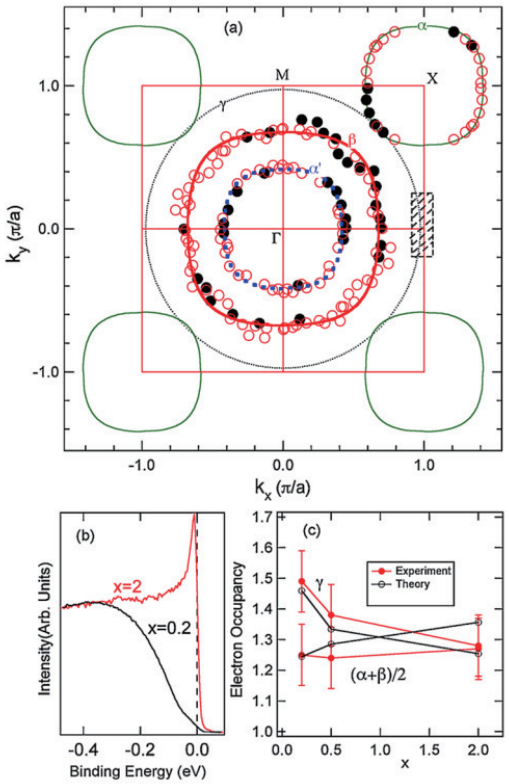

Figure 4.10: OSMP in CSRO [75]

is necessary to study the overall evolution of the SRIO electronic structure. However, the previous electronic structure studies are confined to study the physics of the SIO and the role of the SOC to the Mott phase [10, 70–74]. This thesis would introduce a systematic study of overall doping dependent band structure in the various doping concentrations of SRIO system, and would analyze the effect of each major parameter change. By the analysis, the thesis would introduce possible new physics driven by the SOC.

4.1.2 Orbital-selectiveness

One of the candidate of the new physics expected would be the orbital-selectiveness (OS). OS indicates the single band property that occurs exclusively within the multi-band structure. For example, the $Ca_{2-x}Sr_xRuO_4$ (CSRO) has

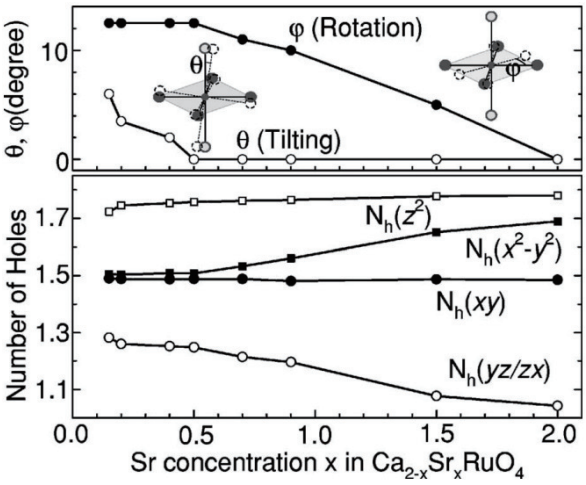

Figure 4.11: Doping dependent structure distortion of CSRO [76]

an orbital-selective Mott phase (OSMP) as shown in the Figure 4.10. From the SRO band structure with three bands (α, β, and γ), the research found that the γ band disappears at the Sr 0.2. The Figure 4.10(b) shows the spectral weight of the γ band at Sr 2.0 and Sr 0.2, with significantly reduced spectral weight at Sr 0.2.

The OSMP in CSRO occurs due to the anisotropic band renormalization of the bands from the structure distortion induced by doping. The Figure 4.11 shows the distortion angle of the system depending on Sr concentration. Starting from the undistorted SRO with Sr 2.0, the reduction of Sr contents immediately introduces the rotation distortion, indicated by θ. Further reduction of the Sr would introduce another distortion ϕ starting from Sr 0.5, which is the tilting of the octahedron by rotating octahedron along the in-plane axis. Such structure distortion modifies the band eigenstates, which creates an anisotropic bandwidth renormalization in α/β and γ [76, 77]. The γ band become much narrower compared to the α and the β, resulting γ band Mott transition, while leaving the α and the β bands metallic.

α-$MoCl_4$ is an another example of OS. In α-$MoCl_4$, the structure transition

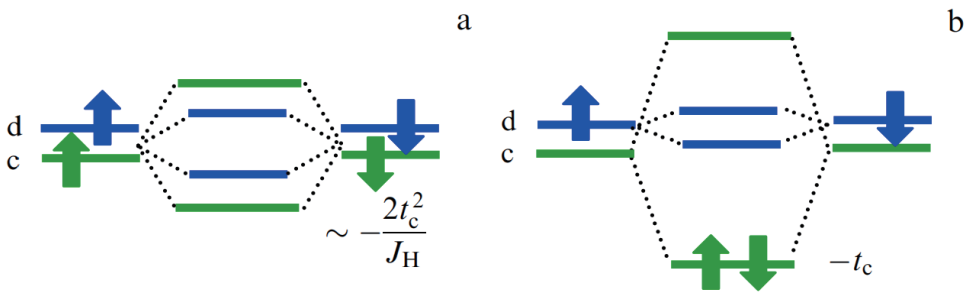

Figure 4.12: Schematic energy states of two neighboring Mo atoms without and with dimerization [78]

triggers the orbital-selective magnetic suppression. The Mo atoms in the system form dimer with nearby Mo atoms, and cause the change of the exchange energy. Without dimer, as shown in the left panel of the Figure 4.12, the exchange energy governs the energy states, therefore, the magnetic moments are localized on atoms. However, the dimerization enlarges the hopping rate between the nearby two atoms, hence, as the right panel of the Figure 4.12 shows, the bonding state between the two become significantly lower. The electrons would no longer localized and would occupy the bonding state, which would suppress the magnetic moment size. However, the formation of the bonding state is anisotropic. Since the dimer in the α-$MoCl_4$ would form along certain direction, only a certain band forms the low energy bonding state. Therefore, only electrons from the certain band suppresses the magnetic moment, hence, the orbital-selective magnetic suppression appears. Similar orbital-selective magnetic suppression is reported in many different systems such as $NaTiSi_2O_6$ [79], $CuIr_2S_4$ [80], indicating the structure has significant role in multi-band magnets.

As shown above, the previous studies attribute the origin of OS to crystal structure. The change of crystal structure would change the eigenstates, which possibly induce large anisotropy between bands. In many cases, indeed, the crystal field has enough energy scale to modify the band structure and trigger the OS.

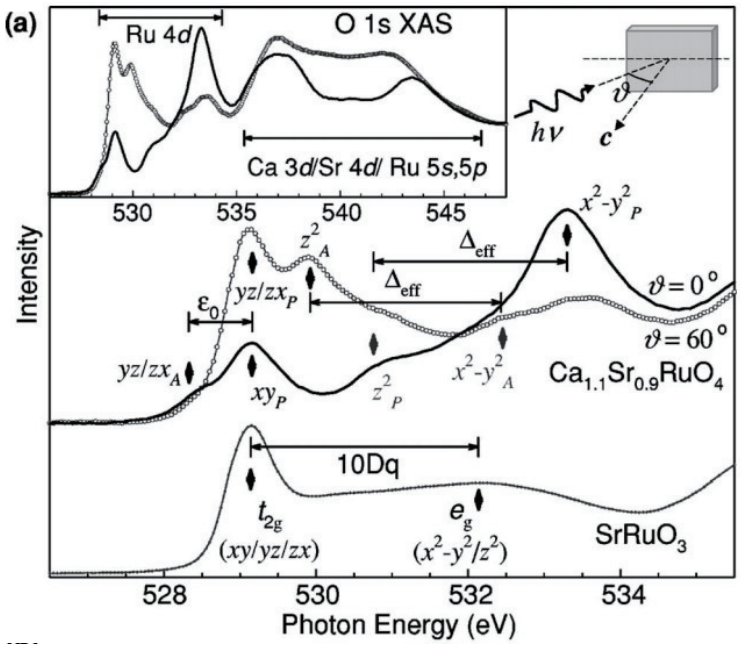

Figure 4.13: XAS measurement of d orbitals of CSRO [76]

For instance, CSRO has significant crystal field driven split between the d_{xy} and $d_{xz/yz}$ orbitals due to octahedron elongation along the c-axis. The Figure 4.13 shows the XAS result showing the energy levels of the d orbitals of CSRO system. The split within the t_{2g} orbitals (d_{xy} and $d_{xz/yz}$) is denoted with ϵ_0, which is about 900 meV. Such result suggests that the energy scale of the structure driven band renormalization in layered perovskite is about few hundred meV, which is enough to trigger the anisotropy between the bands in the CSRO system. This intrigues the idea that the other parameters with enough energy scale may show strong anisotropy of the bands, hence may trigger the OS.

The SOC would be a candidate to trigger the OS. The strength of SOC is significantly large in many systems. For instance, in the 4d TMO SRO, the scale of SOC is about 110 meV, which is not as big as the crystal field driven split of t_{2g} in layered perovskites, but still large enough to affect the band eigenstates, as mentioned in Chapter 1. The SIO, which is 5d TMO, has even larger SOC which is 400 600 meV [10, 44, 45] in the previous studies. However, the SIO system is

not suitable to study the OS since the system is single band Mott insulator.

In this thesis, by substituting Ir into the SRO system, the SOC in multi-band SRO is gradually controlled. The band evolution from the SOC change shows the anisotropic doping effect on γ band, which is possibly a new example of the OS. This thesis provides the possibility of new OS by showing exact role of SOC by distinguishing the effects from other parameters. The study would utilize the band structure simulation with tight-binding calculation compared with the actual electronic structure measured by ARPES. The observed orbital-selective doping effect on γ can be the first example of the OS triggered by SOC.

4.2 Experimental results

4.2.1 Sample growth and characterization

The SRIO single crystals are grown with the flux method. Unlike the floating zone method, which is used to grow the SLRhO system, the flux method uses the container which contains solution consists of the desired material to crystalize and the proper solvent that dissolve it. Even though the risk of contamination from the container presents for the flux method, the flux method is the best choice so far to grow the Ir-based materials. There are two major reason why the flux method is preferred after the floating zone method to grow SRIO single crystal.

First, the volatility of the RuO_2 and IrO_2 is the biggest issue of the SRIO growth. The floating zone method requires to melt the polycrystalline SRIO during the procedure, hence, the temperature of the molten zone would exceed 2000 °C, and the volatility (decomposition) temperature of the IrO_2 is about 1200 °C. Hence, the direct melting of the SRIO would not provide stoichiometric SRIO crystal and would show different phase which contains more Sr per Ru/Ir ratio.

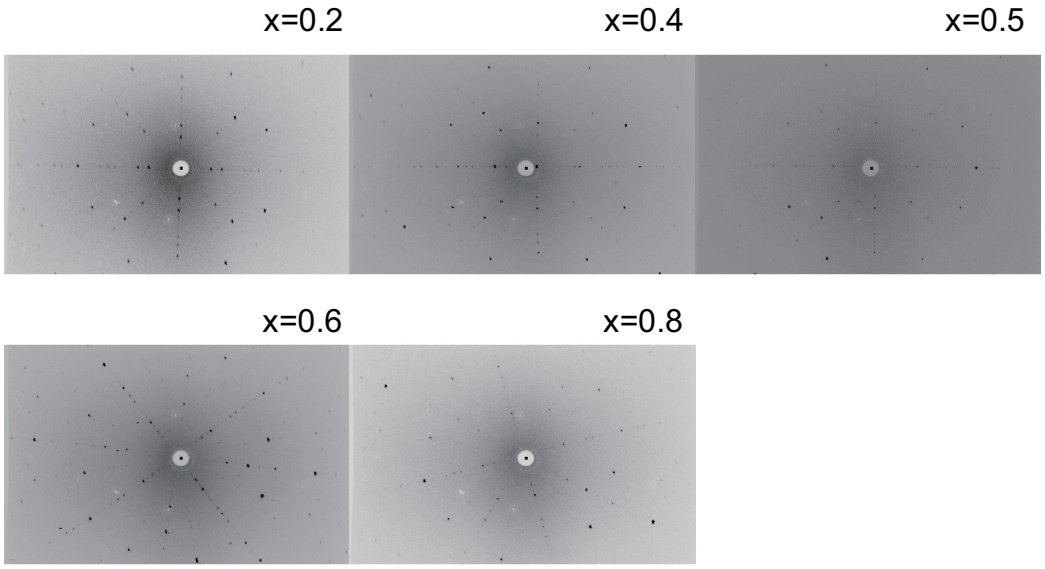

Figure 4.14: Laue images of SRIO

Second, the Ir clusterization is the other obstacle. The study of showed that the high temperature growth clusterizes Ir, which prevents the stoichiometric growth of the Sr_2IrO_3 [81]. Hence, the floating zone method, the high temperature growth method is not suitable to the SRIO growth. The flux method is much preferred growth method for the SRIO single crystals.

The growth of the crystal is done with $SrCl_2$ solvent for all doping region, which is common solvent for the SIO growth. Before growing single crystal, the polycrystal SRIO is grown with the solid reaction following the growth method shown in past researches. The polycrystal is then mixed with the proper amount of solvent. The mixture is then heated up to 1380 °C and cool down slowly.

The basic characterization is done with the grown single crystals. The Laue diffraction measurement shows the fine crystallinity, which shows clear pattern with no broad peaks in the Figure 4.14. The resistivity of selected doping shows gradual increase as shown in the Figure 4.15, which is consistent with the previous research shown in Figure 4.7. However, it is not clear to verify the electronic property of the system with such simple measurement, hence, the rest of the

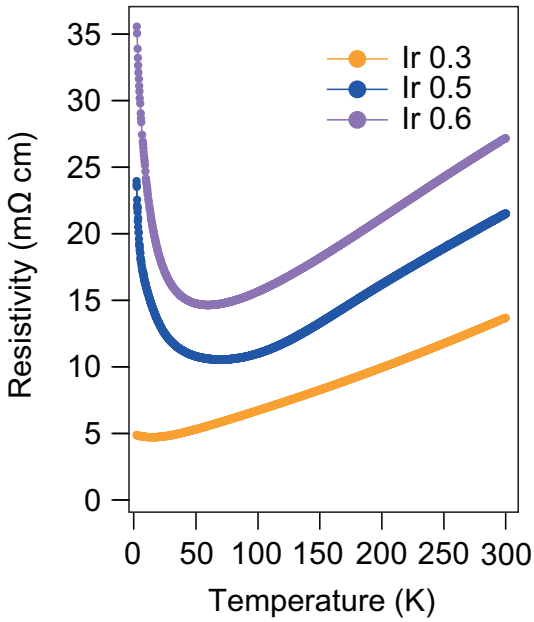

Figure 4.15: Single crystal resistivity measurement of SRIO

section would introduce the electronic structure analysis of SRIO with ARPES experiment.

4.2.2 Electronic structures

The electronic structure with ARPES is measured with synchrotron radiation source with 70 eV photon energy. The measurements all performed under 90 K with ultra-high-vacuum less than 5×10^{-11} Torr. The samples are cleaved under the same ultra-high vacuum, where the measurement is done on the freshly cleaves surfaces, as well as the aged surfaces (described below).

Figure 4.16 shows the Fermi surfaces of SRIO at selected doping, x =0.0, 0.2, 0.5. The upper panel shows the ARPES measurement, and the lower panel shows the schematic band structure with identifying the band character. The Fermi surface of the SRO in the Figure 4.16(a) and (d) shows three types of Fermi surface pockets (α, β, and γ) with conventional identification of the bands as shown in the Figure 4.1. The surface octahedral rotation distortion duplicates

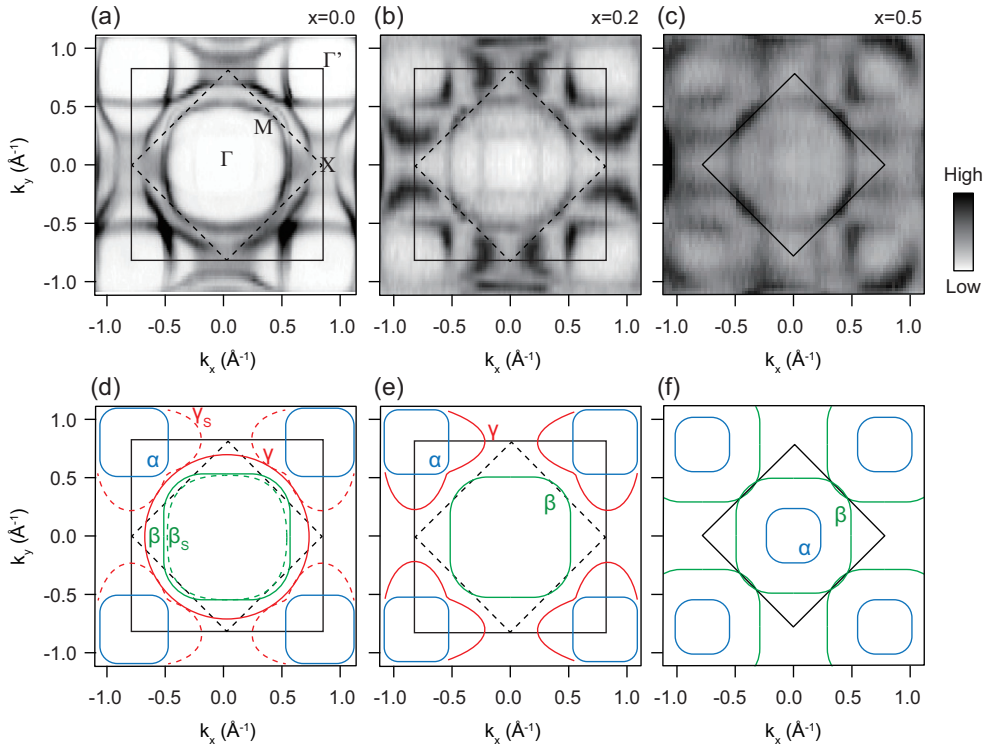

Figure 4.16: Selected electronic structure of SRIO [82]

the Fermi surface pockets to create surface bands, as indicated with dashed lines in the Figure 4.16(d) (α_S, β_S, and γ_S) within a reduced BZ by $\sqrt{2} \times \sqrt{2}$. Note that the bulk γ band is an electron-like pocket centered on Γ, while the surface band γ_S is a hole-like pocket centered on (π,π) of the unreduced BZ (or on Γ' of the reduced BZ). It is clear that the α/β and γ bands show completely different responses to Ir doping. As x increases, Fermi surface volume of α/β bands hardly changes, with the Fermi surface topology unchanged. On the other hand, the bulk γ band shows two-step Lifshitz transitions as shown in the Figure 4.16(b) and (e) (around $x = 0.2$) and Figure 4.16(c) and (f) (around $x = 0.5$).

The first Lifshitz transition occurs before x reaches 0.2. At the $x = 0.0$, the electron-like bulk γ Fermi surface clearly can be distinguished with the hole-like surface γ band. As x increases, the electron-like γ Fermi surface disappears before $x = 0.2$ while the hole-like γ becomes intensified in the Figure 4.16(b). To clarify the bulk γ band evolution, the ARPES measurement of aged sample surface is

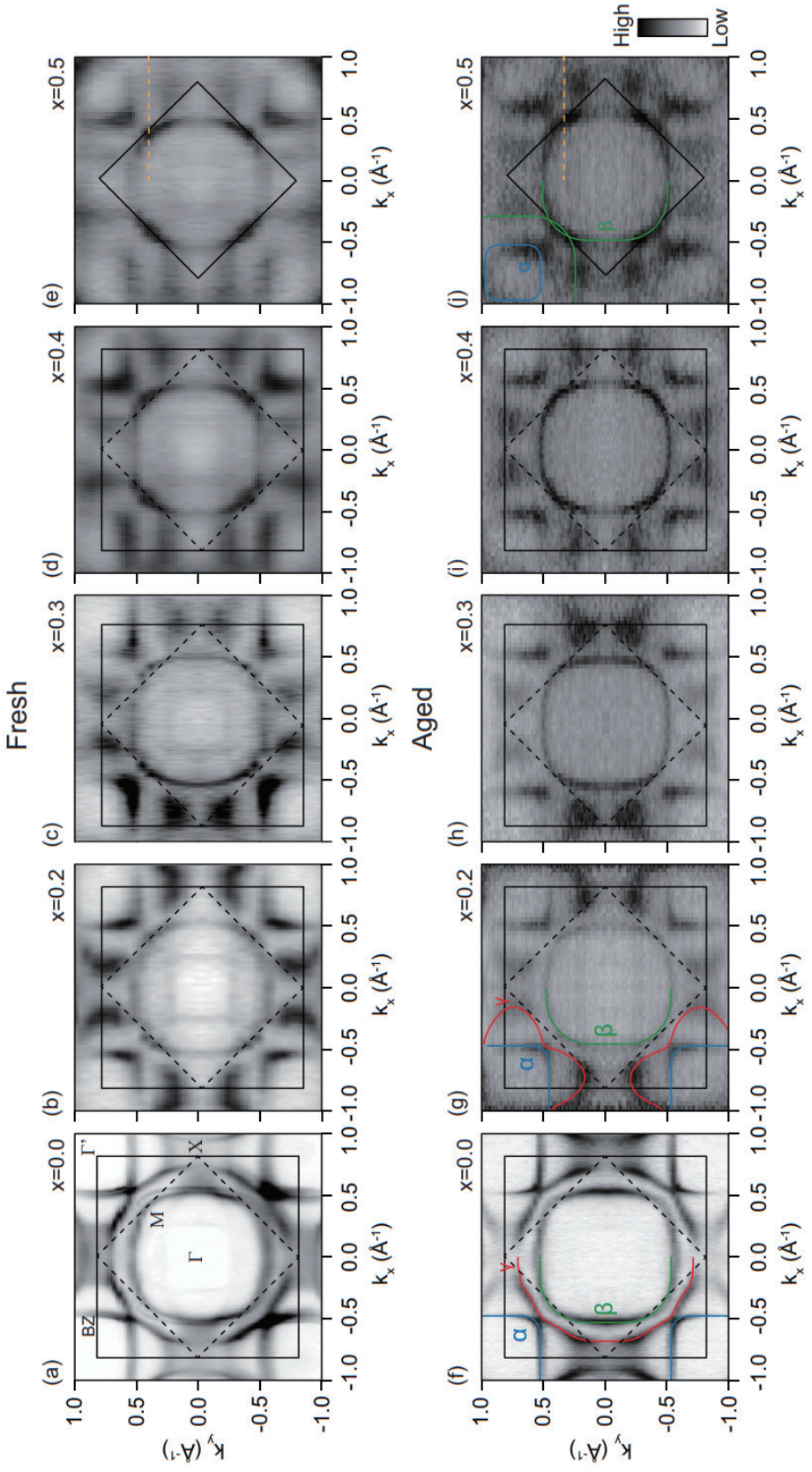

Figure 4.17: Doping dependent electronic structure of SRIO [82]

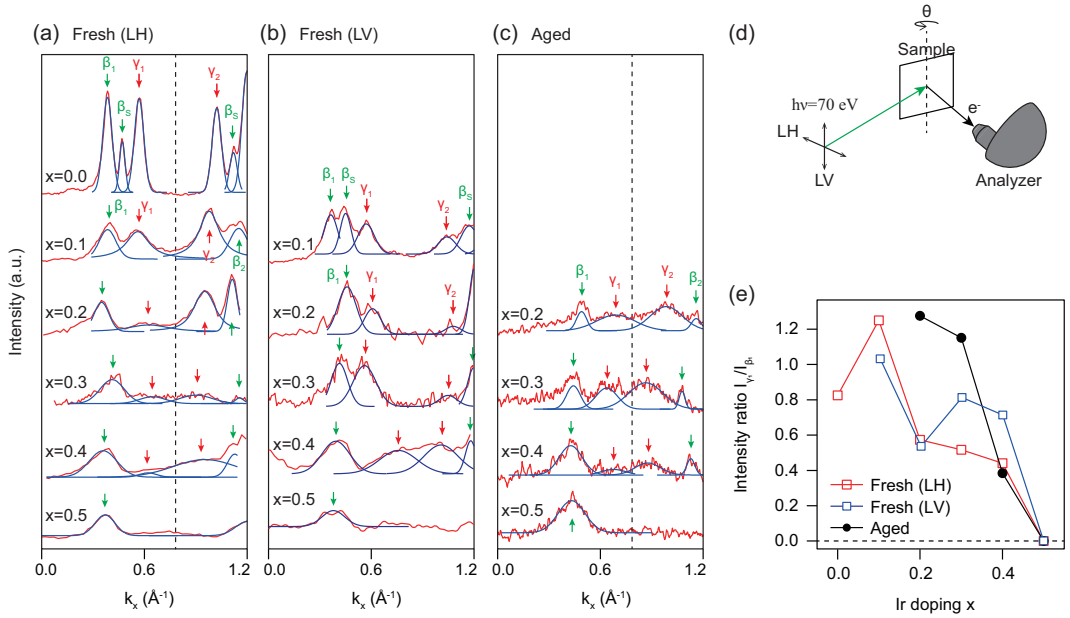

Figure 4.18: Doping dependent MDC analysis [82]

shown in the Figure 4.17(f-j). The aged Fermi surface is obtained by exposing the sample in the ultra-high vacuum over 9 h, which would eliminate the surface band signal. The absence of the α/β replica band in the Figure 4.17(f) suggests the significantly reduced surface bands. At $x = 0.2$ (Figure 4.17(g)), the hole-like γ band still exists even though the surface band is significantly reduced by aging. Hence, the aging measurement suggests that the disappearance of the electron-like γ Fermi surface is due to the Lifshitz transition of the bulk γ band to a hole-like Fermi surface.

After the second Lifshitz transition, the bulk γ band disappears around $x = 0.5$. To clarify the second Lifshitz transition, the Figure 4.18 shows the momentum distribution curve (MDC) analysis on the Fermi level. The distribution curves are extracted at the Fermi level and along the yellow dot line on the Figure 4.16(j) which would contain the signal from the β and the γ. The Figure 4.18(a, b) shows the extracted MDCs from the freshly cleaved samples and the Figure 4.18(c) shows MDCs from the aged samples. The Figure 4.18(a) used linear horizontal (LH) polarization, while the Figure 4.18(b) used linear vertical (LV) polarization,

within the ARPES measurement geometry depicted in the Figure 4.18(d). Figure 4.18(a-c) shows the doping dependent γ band signal reduction in the first and second BZ, which is denoted by the suffix 1 and 2, respectively. After peak fitting of all bands, as indicated with the blue line in the Figure 4.18(a-c), the Figure 4.18(e) shows the γ band peak intensity, normalized by the β band peak intensity in the first BZ. As a result, both freshly cleaved and aged surface shows the γ ban disappearance at the $x = 0.5$, indicating the second Lifshitz transition occurs around $x = 0.5$.

The two Lifshitz transition of the γ suggests the strong anisotropy of band evolution from the Ir substitution. At SRO, it is true that the γ band character, which is strongly d_{xy}, is quite different from the $d_{xz/yz}$ α and β. The d_{xy} band indeed is known to have larger bandwidth compared to the $d_{xz/yz}$, hence, one may expect the effect of the rigid-band shift from Ir substitution may change the γ electron number more than α and β. The first step to analyze the γ band anisotropy would be tracking the rigid-band shift of the bands.

The Figure 4.19 shows the quantitative analysis of each band with electron occupation. The filled squares indicate the electron number calculated from the ARPES Fermi surface data with Luttinger theorem. The empty diamonds are theoretically calculated values with considering the effect of the rigid-band shift from the SRO band structure. First the SRO, the non-doped system, is simulated with the tight-binding model as depicted in Appendix A. The Fermi level of the system is calculated from the density of states (DOS). By varying the total electron occupation, the estimated Fermi level would change, hence, the corresponding Fermi surface change would reflect the effect of rigid-band shift. The empty diamonds are calculation from the simulated Fermi surfaces with Luttinger theorem. Therefore, the difference between the experimentally estimated electron

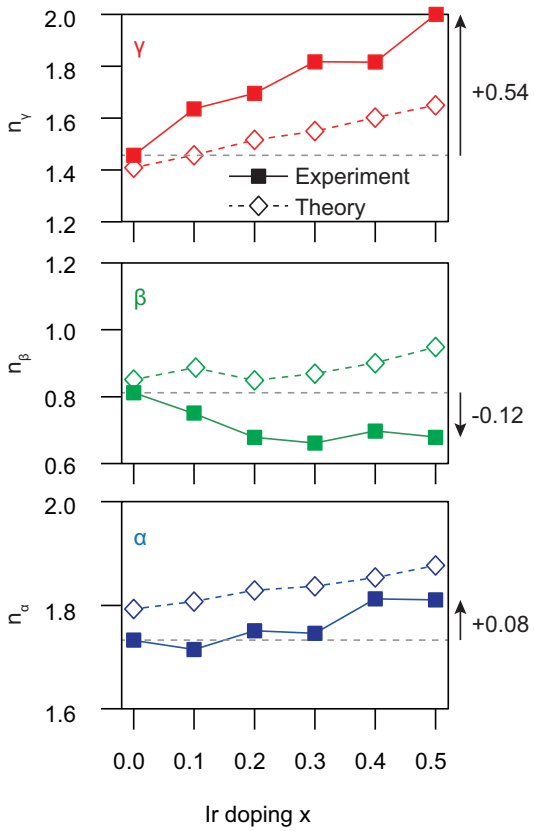

Figure 4.19: Doping dependent electron occupation of each band of SRIO [82]

number and the simulated electron number may exclude the effect of rigid-band shift from the electron supplied by Ir substitution.

From the Figure 4.19, one may clearly observe the γ band anisotropy. The experimentally calculated α electron number shows a little difference from the simulated electron number, however, the slope of doping is similar, and shows positive doping. The β, on the other hand, shows negative doping from the Ir substitution, while the simulation clearly shows positive doping. The γ band shows anomalously large doping rate, much higher than the simulated one. At the $x = 0.5$, the experimentally estimated electron doping of α, β, and γ are $+0.08e$, $-0.06e$, and $+0.54$, respectively. The estimation would imply that the electron number change of the α and the β seems to be compensated, and the γ receives all of the electrons from the Ir atoms. Hence, the γ band is selectively doped by Ir substitution.

This thesis defines the anisotropy of the doping on the γ as "orbital-selective doping effect", analogous to previous research on orbital-selectiveness. Even though the orbital character of the γ changes due to various parameter change as describes above, this thesis follows the Fermi surface pocket to identify the bulk γ and nominates the bulk γ band anisotropy as the γ orbital-selective doping effect. The previous research on CSRO, the orbital-selective Mott phase indicates the state of the band structure at certain compound, where the γ band has Mott phase. In CSRO case, the order parameter of the orbital-selective Mott transition is a gap size of the γ band. On the other hand, for the SRIO case, the electron number increase of the γ is the order parameter of the orbital-selective doping effect. Hence, even the "orbital" of the γ band differs by the doping level, the orbital-selective doping effect is defined by the phenomena that the bulk γ band electron number increase from the SRO is approximately same with the Ir doping rate.

The orbital-selective doping effect is consistent with the drastic change of the γ band. However, it remains a question. Even the tight-binding calculation simulates the large bandwidth of the γ band, the calculation cannot simulate the large doping rate of the experimental result. The drastic change of the γ band topology cannot be explained solely with the anisotropy of the bandwidth. Hence, role of the additional parameter is necessary.

4.3 Mechanism of γ band anomaly

To understand the anisotropy of the γ band, it is necessary to understand the mechanism of the γ orbital-selective doping effect. Based on previous researches on orbital-selectiveness, one may consider crystal structure change to understand

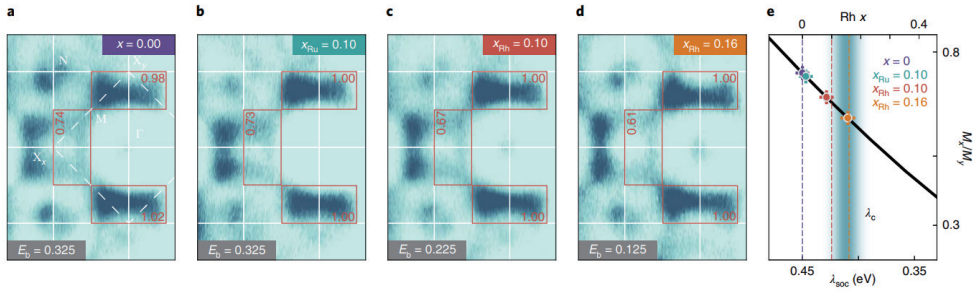

Figure 4.20: SOC measured by spectral weight analysis of doped SIO [10]

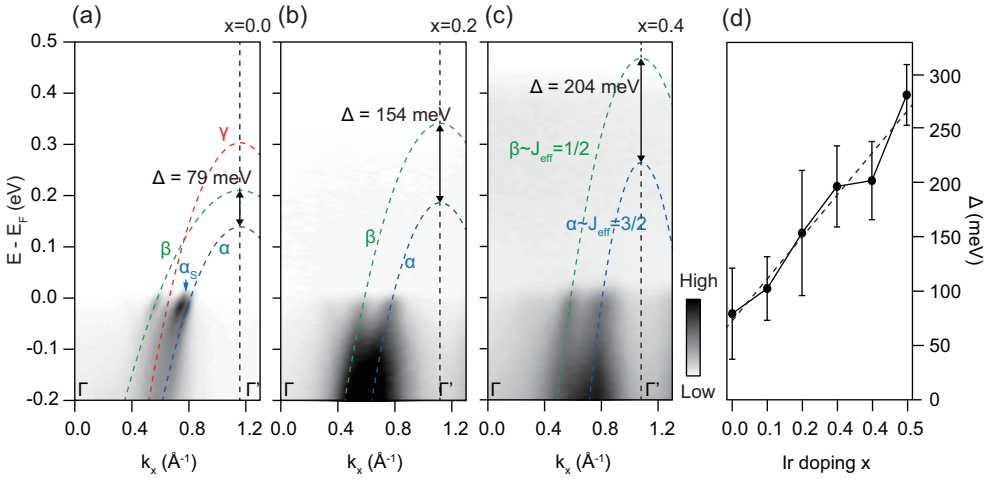

Figure 4.21: SOC measured by band split analysis of SRIO [82]

the orbital-selective doping effect on γ. Since the common origin of the orbital-selectiveness is crystal structure, it is natural to seek a structure transition. However, as shown in Figure 4.8, the structure transition of the SRIO only occur at $x = 0.5$ with sudden transition of the octahedron rotation angle. To achieve gradual doping of the γ band, the gradually changing parameter is required.

As mentioned above, one possible origin is the SOC. By the 5d transition metal Ir substitution on the 4d transition metal Ru, it is easy to consider the gradual change of SOC with respect to doping level. The Figure 4.20 shows the spectral weight analysis of the SRIO and $Sr_2Rh_{1-x}Ir_xO_4$ Fermi surface with ARPES techniques. By extracting the spectral weight of the Fermi surface, the study showed the linearly changing effective SOC by calculating the band splitting with the change of the doping. Similarly, the Figure 4.21 shows energy-momentum spec-

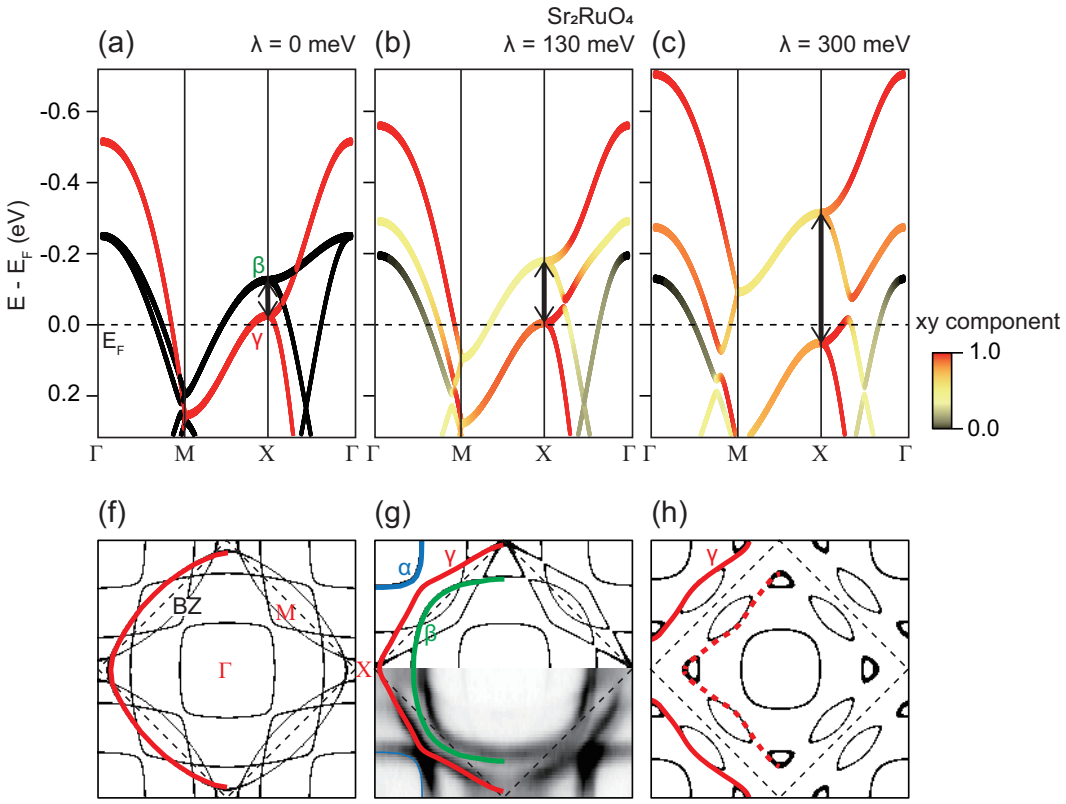

Figure 4.22: Tight-binding simulation of SRIO with varying SOC

trum along $\Gamma - M - \Gamma'$, where one may estimate the effective SOC from the energy split of bands. The α and the β in the Figure 4.21(a-c) are known to have SOC-driven split at the Γ point (also can be seen in the Figure 4.22, the tight-binding calculation with varying SOC, which is described below). Hence, the split of the α and the β (Δ) is related to the magnitude of SOC. The Figure 4.21(d) shows the doping dependent Δ, which shows the linearity with respect to Ir doping level. The analysis indicates that the SOC may gradually increase by Ir substitution.

To study the effect of the gradually varying SOC, tight-binding with varying SOC is shown in the Figure 4.22, with the method described on the Appendix A. The band structure in Figure 4.22(b) and (g) is the calculated band structure of SRO and corresponding Fermi surface, which shows good agreement with the ARPES measured Fermi surface. From the simulation, the Figure 4.22(a) and (f)

are simulated with reducing the SOC energy λ to 0 meV, and the Figure 4.22(c) and (h) are simulated with increasing λ to 300 meV. For all figures, the eigenstate of each point is projected with the d_{xy} band to show the band character, where the projection is shown with the color scale. At Figure 4.22(a), the bands can be distinguished clearly into two different characters, the d_{xy} band and the $d_{xz/yz}$ bands. The d_{xy} band corresponds to γ band, and the β is located above the γ band on X point as denoted on the Figure 4.22(a). The increase of SOC mixes the two bands, which can be indicated by the change of the projection. Moreover, the band mixing renormalizes the two bands, which can be represented by the split of the bands on the X point, shown with the black arrow. The Figure 4.22(b) shows increased d_{xy} component on the β indicating such band mixing, which enlarges the band split of the β and the γ by raising the β along energy direction and lowering the γ. Further increase of the SOC on Figure 4.22(c) enlarges such split.

The SOC-driven renormalization explains the γ orbital-selective doping effect. Since the SOC is gradually increasing from the doping, the β band position gradually moves upward in energy, resulting the negative doping as shown in the Figure 4.19. Moreover, the γ is lowered by the SOC, which leads to the large electron doping on the γ. Hence, with gradually varying the SOC, the β is negatively doped to compensate the electron doping of the α, and the γ band gradually sinks to receive all the electrons provided by the Ir substitution. The Figure 4.23(a) simulates the electron doping on the Fermi surface with large SOC. The arrow in the Figure 4.23(a) indicates the electron doping driven Fermi level increase on the same band structure in the Figure 4.22(c). The corresponding Fermi surface (Figure 4.23(d)) shows the largely doped γ band with remaining α and the β.

The SOC may explain the orbital-selective doping with assistance of rigid-

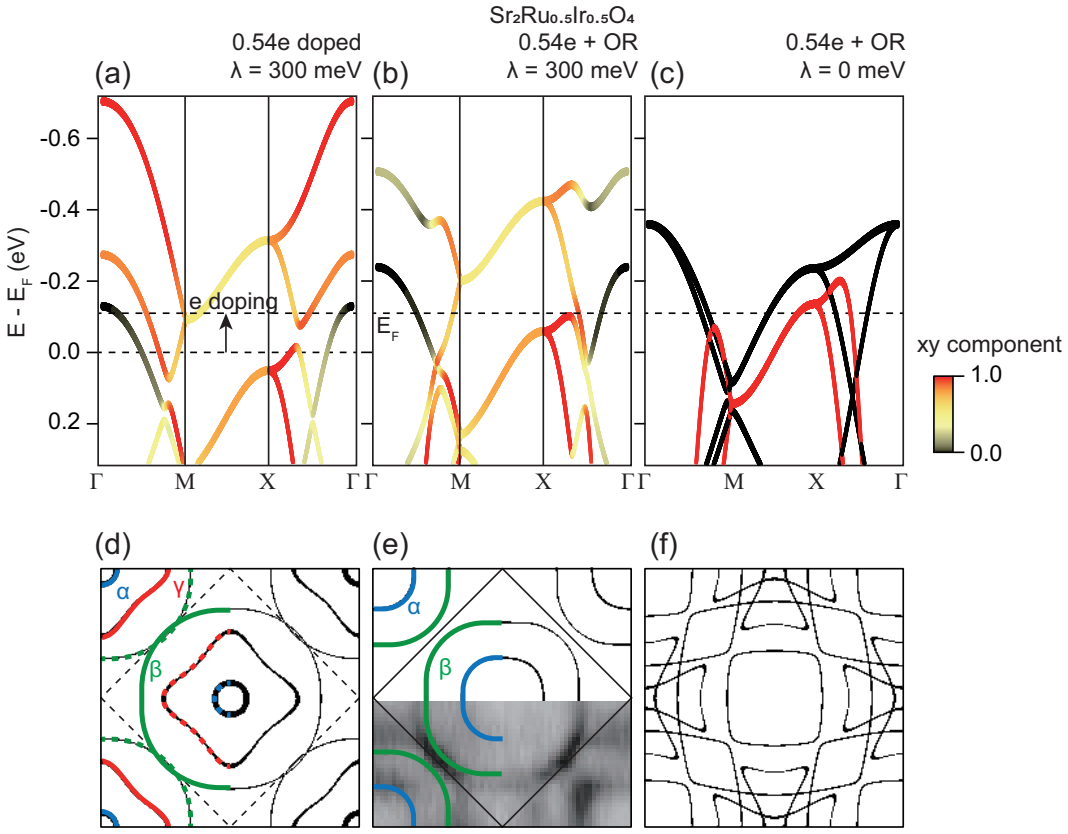

Figure 4.23: Tight-binding simulation of SRIO with and without OR

band shift, however, the remaining parameter exists, which is the octahedron rotation. In many chemically doped systems, the dopant may bring the difference of the radii, which may trigger the structure transition. Since, the SRO doesn't have octahedron rotation distortion, and SIO does have it, the Ir substitution on the SRO may trigger the gradually growing octahedron rotation angle due to gradually changing the crystal field. However, as mentioned above, the octahedron rotation doesn't appear until the doping level reaches $x = 0.5$. Therefore, the octahedron rotation may not affect the orbital-selective doping effect since, the orbital-selective doping is the gradual property that appears immediately by Ir substitution.

Though, the role of octahedron rotation may provide a clue of the second Lifshitz transition the disappearance of the γ Fermi surface. The second Lifshitz

transition appears at the $x = 0.5$ as mentioned above, which coincides with the octahedron rotation as shown by the previous studies (Figure 4.8). From the theoretical study of the octahedron rotation distortion of layered perovskite systems as shown in the Figure 4.3, the rotation distortion changes the electronic structure drastically, mainly by causing hybridization between the d_{xy} and $d_{x^2-y^2}$ due to unit cell doubling.

Hence, by including the effect of the $d_{x^2-y^2}$ hybridization, the octahedron rotation is implemented in the Figure 4.23(b) and (e). The resulting band structure has no γ band crossing the Fermi surface, since the hybridization sinks the top part of the γ which mainly have d_{xy} character. As a result, the Fermi surface in the Figure 4.23(e) does not have the γ band pocket, remaining the α and the β band pocket reasonably agree with the $x = 0.5$ ARPES data as overlaid on the Figure 4.23(e).

The Figure 4.23(c) and (f) shows the octahedron rotation driven hybridization without effect of SOC. The red γ band indicates a full projection of γ band to d_{xy} band character, which has large dip at the Γ point due to hybridization with $d_{x^2-y^2}$ band. It is notable that, without SOC, the γ band still crosses the Fermi level. This implies that the γ band does not become fully occupied at $x = 0.5$ if there is no effect of SOC. Still, for the second Lifshitz transition, SOC has a significant role on the Fermi surface topology.

The study of the tight-binding calculation compared with the ARPES data shows that the SOC may have crucial role. The SOC may trigger the γ selective doping effect by renormalizing the band character. Furthermore, even the γ band may disappear with coinciding octahedron rotation distortion, the SOC is a necessary parameter to make the γ band completely disappear.

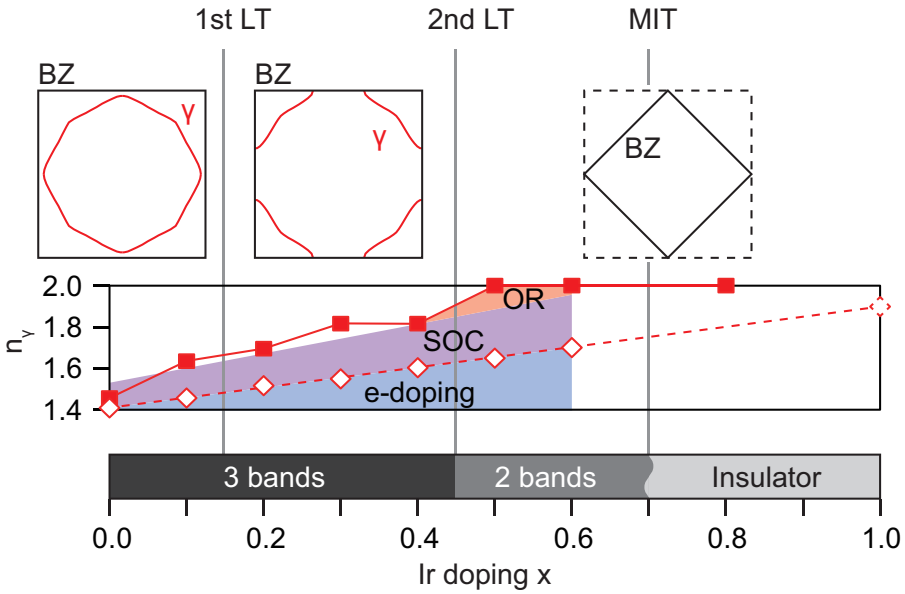

Figure 4.24: Overall γ band evolution depending on doping

4.4 Overall band evolution

With the novel physics of orbital-selective doping effect on the γ band, the study of the SRIO may provide full connection between the SRO and SIO band structure. As shown in the Figure 4.24, the γ band shows drastic change, which is due to the large change of the γ electron occupation n_γ. The bottom panel in the Figure 4.24 shows the complete phase diagram of the band structure on the Fermi level, which is completed by the additional ARPES measurement of the higher doping compounds in the Figure 4.25, where the $x = 0.6$ shows similar 2-band structure with $x = 0.5$ and the $x = 0.8$ shows SIO-like insulating band structure. Understanding this phase diagram completes the detailed understanding of the band evolution from 3-band metallic SRO system to single-band Mott insulator SIO system.

The 3-band structure of SRO has transition to 2-band system by filling the γ band. For $x \leq 0.4$, analysis above suggests that the γ is almost fully occupied by the gradual change of SOC, which is suggested as the γ band orbital-selective

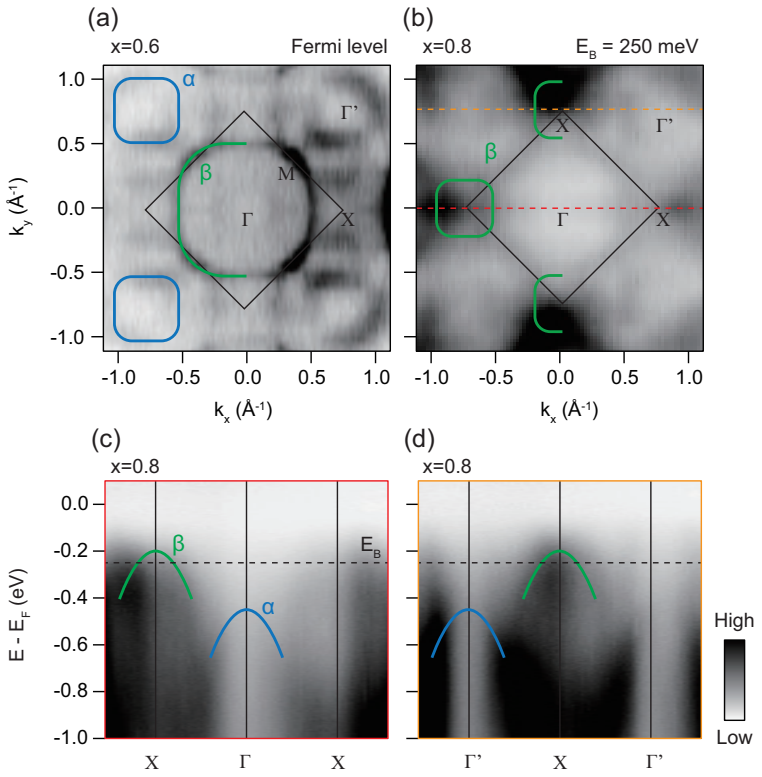

Figure 4.25: ARPES results of high doping concentration of SRIO

doping. At $x = 0.5$, the octahedron rotation renormalizes the d_{xy} component of the γ to fully occupy the γ. However, considering the small doping effect caused by octahedron rotation (0.18 e) and the fact that the SOC is necessary parameter for full occupation of the γ (Figure 4.23(c) and (f)), the SOC can be considered as a major parameter.

Further increase of SOC triggers the transition from 2-band to Mott insulator. As the SIO structure in the previous chapter (Figure 3.5) showes, the SIO has two bands near Fermi level, which are identified by α and β. The α and the β, which has $d_{xz/yz}$ character without SOC, are renormalized by SOC to become $J_{eff} = 3/2, |m_{J_{eff}}| = 3/2$ and $J_{eff} = 1/2$, respectively. The strong SOC would split the α and the β, and would make α band sink below Fermi level, remaining $J_{eff} = 1/2$ β only remains on the Fermi surface. At the SIO end, the only remaining β would be half filled, which induces the Mott phase. It is notable that

the electronic structure of the $x = 0.8$ (Figure 4.25(b-d)) is quite similar with that of SIO (Figure 4.4), indicating the Mott phase exists even at the $x = 0.8$.

4.5 Conclusion

In this section the electronic structure study of SRIO is introduced. The study showed overall band evolution from the distinct compounds SRO and SIO, and suggested a new type of orbital-selectiveness which may relies on the SOC-driven band renormalization. The study have several important implications.

The first concerns the discovery of an exotic orbital-selective doping effect driven by SOC. Until now, crystal structure was thought to be the most important factor to trigger orbital-selective phenomena. However, the energy scales of SOC strength (150-400 meV in 4d/5d TMOs) are comparable with that of crystal field splitting (a few hundreds of meV), thus the SOC may be a factor that is sufficient to trigger orbital-selective phenomena. Consistent with this, we observed an orbital-selective doping effect in SRIO, which is caused by the band evolution driven by the SOC. The observation suggests the SOC as a new origin to the orbital-selectiveness, and moreover, it would expand the boundary of materials with orbital-selectiveness.

Another importance of our study is the provision of more quantitative analysis on the role of SOC. Although there have been many studies on $5d$ iridates, which have strong SOC, most were limited to the strong SOC regime, focusing on the exotic phenomena of the system itself. For instance, there have been various electronic structure studies on SRIO [10, 70] as well as $Sr_2Rh_{1-x}Ir_xO_4$ [9] to understand the role of SOC, but most have focused on the strong SOC-driven Mott insulating state in SIO, not on how SOC determines the electronic structures.

To fully understand the role of SOC and to discover SOC-driven novel phenomena, a quantitative and comprehensive study that tracks electronic structure with SOC variation is essential. Therefore, it is essential to investigate the electronic structure of the metallic state rather than the insulating one, because the strong electron correlation effect precludes observing the electronic structure directly. In this respect, we focused on the metallic state of SRIO, and quantitatively extracted the effects of SOC in terms of electron re-distribution in the electronic structure. We believe that our study not only elucidates how SOC transforms electronic structure sufficiently to form the Mott state in SRIO but also provides a methodological way to estimate the effect of SOC quantitatively.

Systematic electronic structure studies on SRIO are performed and the result showed a novel orbital-selective doping effect. From the quantitative analysis of our ARPES results with the help of TB simulation, we found that the SOC in SRIO modifies the band structure, which leads to the orbital-selective doping effect on γ. The finding would not only open a new avenue to the orbital-selective physics by introducing a new origin, but would show a connection between the metallic multi-band SRO system and the single-band Mott insulator SIO.

Chapter 5

Summary and remarks

This thesis introduces a new SOC-driven physics in the 4d TMO systems. Even though the study on 4d systems not treated the SOC as a controlling parameter, this thesis suggested that the moderateness of the SOC enough to modify the eigenstates of the system, and trigger the new physics.

The study on the electron doped SRhO shows a new type of MIT that can be triggered by the Lifshitz trnasition. The study clearly addresses that such MIT cannot occur in the weak or strong SOC regime, which cannot induce the electron doping driven Lifshitz transition. The study not only emphasizes that the moderateness of the SOC may trigger the new physics, but also shows a method to study the multi-band system with the electronic structure analysis via ARPES.

The study on SRIO expands the physics of OS in multi-band systems. The study discovered a orbital-selective doping effect on a certain band, which is triggered gradually by the varying SOC in multi-band SRO system. The discovery may expand the study of OS, since the study of OS does not considered SOC as an triggering parameter. Furthermore, the study of OS in SRIO showed the role of multi-band systems, which often can be found in 4d TMO systems with moderate SOC.

This thesis showed that, even though the strong SOC showed exotic Mott

physics in 5d TMOs and topological properties in others, the study of the SOC does not have to be limited to the strong SOC limit. Even though the SOC is not large in the 4d TMOs, this thesis shows the band structures are strongly affected by such moderate SOC. Via thorough band structure analysis with the ARPES measurement with proper analysis techniques including tight-binding calculation, this thesis shows the SOC may trigger the new physics those are not found in the 5d TMO systems.

Furthermore, unlike the 3d/5d TMOs, the 4d TMO systems typically have the multi-band structure that natrually leads to complex interaction between the bands. The study of Hund coupling shows that the spin configuration of the multi-band 4d systems induces changes in correlation, which predicts strong correlation effect in some of the 4d systems [59]. Since the study of SRhO and SRO based compounds in this thesis showed that such multi-band structure can be constructed with the SOC, and triggers the new physics, the study of the Hund coupling and other multi-band features would be intrigued to implement the effect of SOC. As a result, this thesis not only enlarges the interest in the complex multi-band structure, but also introduces the new point of view to analyze the multi-band structure via tracking the effect of the SOC.

Moreover, there are many different 4d TMO systems that show new physics that has lack of explanation. The system of SRO shows anomalous doping dependent effect, where a slight doping of magnetic atoms would trigger the immediate long range order [83], and slight doping of the Ti provides immediate MIT [84].

This thesis would be a good informative note to further study of the complex 4d TMO systems, via introducing the method and example of studying 4d multi-band physics by considering the effect of SOC.

Bibliography

[1] John Bardeen, Leon N Cooper, and J Robert Schrieffer. "Microscopic theory of superconductivity". In: *Physical Review* 106.1 (1957), p. 162 (cit. on p. 2).

[2] NF Mott and R Peierls. "Discussion of the paper by de Boer and Verwey". In: *Proceedings of the Physical Society* 49.4S (1937), p. 72 (cit. on p. 2).

[3] KV Shanavas, Zoran S Popović, and S Satpathy. "Theoretical model for Rashba spin-orbit interaction in d electrons". In: *Physical Review B* 90.16 (2014), p. 165108 (cit. on p. 2).

[4] Z-H Zhu et al. "Rashba spin-splitting control at the surface of the topological insulator Bi_2Se_3". In: *Physical review letters* 107.18 (2011), p. 186405 (cit. on p. 4).

[5] Seung Ryong Park et al. "Chiral orbital-angular momentum in the surface states of Bi_2Se_3". In: *Physical Review Letters* 108.4 (2012), p. 046805 (cit. on p. 4).

[6] Albert Fert, Vincent Cros, and Joao Sampaio. "Skyrmions on the track". In: *Nature nanotechnology* 8.3 (2013), pp. 152–156 (cit. on pp. 4, 5).

[7] BJ Kim et al. "Novel J eff= 1/2 Mott state induced by relativistic spin-orbit coupling in Sr_2IrO_4". In: *Physical review letters* 101.7 (2008), p. 076402 (cit. on pp. 5–7, 65).

[8] Alberto De La Torre et al. "Collapse of the Mott gap and emergence of a nodal liquid in lightly doped Sr_2IrO_4". In: *Physical review letters* 115.17 (2015), p. 176402 (cit. on pp. 7, 68).

[9] Alex Louat et al. "Formation of an incoherent metallic state in Rh-doped Sr_2IrO_4". In: *Physical Review B* 97.16 (2018), p. 161109 (cit. on pp. 7, 93).

[10] Berend Zwartsenberg et al. "Spin-orbit-controlled metal–insulator transition in Sr_2IrO_4". In: *Nature Physics* 16.3 (2020), pp. 290–294 (cit. on pp. 7, 9, 72, 73, 76, 86, 93).

[11] BJ Kim et al. "Phase-sensitive observation of a spin-orbital Mott state in Sr_2IrO_4". In: *Science* 323.5919 (2009), pp. 1329–1332 (cit. on pp. 7, 65).

[12] MW Haverkort et al. "Strong spin-orbit coupling effects on the fermi surface of Sr_2RuO_4 and Sr_2RhO_4". In: *Physical review letters* 101.2 (2008), p. 026406 (cit. on pp. 8, 9).

[13] ME Becquerel. "Mémoire sur les effets électriques produits sous l'influence des rayons solaires". In: *Comptes rendus hebdomadaires des séances de l'Académie des sciences* 9 (1839), pp. 561–567 (cit. on p. 13).

[14] Albert Einstein. "On a heuristic point of view concerning the production and transformation of light". In: *Annalen der Physik* (1905), pp. 1–18 (cit. on p. 13).

[15] Baiqing Lv, Tian Qian, and Hong Ding. "Angle-resolved photoemission spectroscopy and its application to topological materials". In: *Nature Reviews Physics* 1.10 (2019), pp. 609–626 (cit. on pp. 14, 16).

[16] Carl Nordling, Evelyn Sokolowski, and Kai Siegbahn. "Precision method for obtaining absolute values of atomic binding energies". In: *Physical Review* 105.5 (1957), p. 1676 (cit. on p. 14).

[17] FI Vilesov, BL Kurbatov, and AN Terenin. "Energy distribution of electrons in photoionization of aromatic amines in the gaseous phase". In: *SPhD* 6 (1961), p. 490 (cit. on p. 15).

[18] A Oelsner et al. "Microspectroscopy and imaging using a delay line detector in time-of-flight photoemission microscopy". In: *Review of Scientific Instruments* 72.10 (2001), pp. 3968–3974 (cit. on p. 19).

[19] Toshiyuki Taniuchi, Yoshinori Kotani, and Shik Shin. "Ultrahigh-spatial-resolution chemical and magnetic imaging by laser-based photoemission electron microscopy". In: *Review of Scientific Instruments* 86.2 (2015), p. 023701 (cit. on p. 20).

[20] C Jozwiak et al. "A high-efficiency spin-resolved photoemission spectrometer combining time-of-flight spectroscopy with exchange-scattering polarimetry". In: *Review of Scientific Instruments* 81.5 (2010), p. 053904 (cit. on p. 20).

[21] Chris Jozwiak et al. "Spin-polarized surface resonances accompanying topological surface state formation". In: *Nature communications* 7.1 (2016), pp. 1–7 (cit. on p. 20).

[22] NJ Shevchik. "A high intensity discharge lamp for monochromatized UV angle-resolved photoemission spectroscopy". In: *Journal of Electron Spectroscopy and Related Phenomena* 14.6 (1978), pp. 411–416 (cit. on p. 20).

[23] Tomasz Durakiewicz et al. "He discharge lamp for photoemission experiments with radioactive materials". In: *Review of scientific instruments* 73.11 (2002), pp. 3750–3753 (cit. on p. 20).

[24] Akiko Hokura and Emiko Harada. "Synchrotron Radiation X-Ray Analysis of Metal-Accumulating Plants". In: (2017), pp. 125–145 (cit. on p. 21).

[25] URL: https://sites.google.com/a/lbl.gov/bl403-rixs-and-battery-es/home/beamline/beamline-flux-and-resolution/ (cit. on p. 22).

[26] Xingjiang Zhou et al. "New developments in laser-based photoemission spectroscopy and its scientific applications: a key issues review". In: *Reports on Progress in Physics* 81.6 (2018), p. 062101 (cit. on p. 23).

[27] Y Ishida et al. "Time-resolved photoemission apparatus achieving sub-20-meV energy resolution and high stability". In: *Review of Scientific Instruments* 85.12 (2014), p. 123904 (cit. on p. 23).

[28] Felix Schmitt et al. "Transient electronic structure and melting of a charge density wave in $TbTe_3$". In: *Science* 321.5896 (2008), pp. 1649–1652 (cit. on p. 23).

[29] S Gerber et al. "Femtosecond electron-phonon lock-in by photoemission and x-ray free-electron laser". In: *Science* 357.6346 (2017), pp. 71–75 (cit. on p. 23).

[30] T Kimura et al. "Magnetic control of ferroelectric polarization". In: *nature* 426.6962 (2003), pp. 55–58 (cit. on p. 23).

[31] Kunihiko Oka et al. "Crystal growth of La2-xSrxCuO4-delta by the travelling-solvent floating-zone method". In: *Journal of crystal growth* 137.3 (1994), pp. 479–486 (cit. on p. 23).

[32] DJ Song et al. "Photoemission studies on electron doped cuprate $Pr_{0.85}LaCe_{0.15}CuO_4$: Revisiting the chemical pressure effect". In: *Journal of Physics and Chemistry of Solids* 72.5 (2011), pp. 533–535 (cit. on p. 23).

[33] Hanna A Dabkowska and Antoni B Dabkowski. "Crystal growth of oxides by optical floating zone technique". In: (2010), pp. 367–391 (cit. on p. 25).

[34] Ruixing Liang, Douglas A Bonn, and Walter N Hardy. "Growth of YBCO single crystals by the self-flux technique". In: *Philosophical Magazine* 92.19-21 (2012), pp. 2563–2581 (cit. on p. 26).

[35] NH Sung et al. "Crystal growth and intrinsic magnetic behaviour of Sr_2IrO_4". In: *Philosophical Magazine* 96.4 (2016), pp. 413–426 (cit. on p. 26).

[36] Yunjeong Hong et al. "Large magnetic anisotropy in canted antiferromagnetic Sr_2IrO_4 single crystals". In: *Physical Review B* 93.9 (2016), p. 094406 (cit. on p. 26).

[37] URL: http://hyperphysics.phy-astr.gsu.edu/hbase/quantum/bragg.html (cit. on p. 28).

[38] Augusto Di Gianfrancesco. "Technologies for chemical analyses, microstructural and inspection investigations". In: (2017), pp. 197–245 (cit. on p. 29).

[39] URL: https://es.wikipedia.org/wiki/Cristalograf (cit. on p. 30).

[40] URL: https://chem.libretexts.org/Bookshelves/Inorganic_Chemistry/ (cit. on p. 33).

[41] Mitsuru Itoh et al. "Structure of two-dimensional conductor of Sr_2RhO_4". In: *Journal of Solid State Chemistry* 118.1 (1995), pp. 206–209 (cit. on p. 35).

[42] Ichiro Nagai et al. "Quasi-Two-Dimensional Fermi-Liquid State in $Sr_2RhO_{4-\delta}$". In: *Journal of the Physical Society of Japan* 79.11 (2010), p. 114719 (cit. on pp. 37, 44).

[43] BJ Kim et al. "Missing x y-Band Fermi Surface in 4 d Transition-Metal Oxide Sr_2RhO_4: Effect of the Octahedra Rotation on the Electronic Structure". In: *Physical review letters* 97.10 (2006), p. 106401 (cit. on pp. 38, 47, 67).

[44] Guo-Qiang Liu et al. "Coulomb-enhanced spin-orbit splitting: the missing piece in the Sr 2 RhO 4 puzzle". In: *Physical review letters* 101.2 (2008), p. 026408 (cit. on pp. 38, 39, 76).

[45] Cyril Martins et al. "Reduced effective spin-orbital degeneracy and spin-orbital ordering in paramagnetic transition-metal oxides: Sr_2IrO_4 versus Sr_2RhO_4". In: *Physical review letters* 107.26 (2011), p. 266404 (cit. on pp. 41, 76).

[46] Tetsuo Shimura et al. "Preparation and electronic properties of $Sr_{2-x}La_xRhO_4$". In: *Physical Review B* 49.8 (1994), p. 5591 (cit. on p. 41).

[47] Kyo-Hoon Ahn, Kwan-Woo Lee, and Jan Kuneš. "Doping-dependent bandwidth renormalization and spin–orbit coupling in $(Sr_{1-x}La_x)_2RhO_4$". In: *Journal of Physics: Condensed Matter* 27.8 (2015), p. 085602 (cit. on p. 42).

[48] Junyoung Kwon et al. "Lifshitz-Transition-Driven Metal-Insulator Transition in Moderately Spin-Orbit-Coupled $Sr_{2-x}La_xRhO_4$". In: *Physical Review Letters* 123.10 (2019), p. 106401 (cit. on pp. 46, 48, 49, 58).

[49] Yuefeng F Nie et al. "Interplay of spin-orbit interactions, dimensionality, and octahedral rotations in semimetallic $SrIrO_3$". In: *Physical review letters* 114.1 (2015), p. 016401 (cit. on p. 52).

[50] Louis Taillefer. "Scattering and pairing in cuprate superconductors". In: *Annu. Rev. Condens. Matter Phys.* 1.1 (2010), pp. 51–70 (cit. on p. 52).

[51] Tianping Ying et al. "Anderson localization of electrons in single crystals: $Li_xFe_7Se_8$". In: *Science advances* 2.2 (2016), e1501283 (cit. on pp. 53, 54).

[52] Aaron Bostwick et al. "Quasiparticle transformation during a metal-insulator transition in graphene". In: *Physical review letters* 103.5 (2009), p. 056404 (cit. on p. 55).

[53] Al L Éfros and Boris I Shklovskii. "Coulomb gap and low temperature conductivity of disordered systems". In: *Journal of Physics C: Solid State Physics* 8.4 (1975), p. L49 (cit. on pp. 55, 57).

[54] VI Arkhipov, EV Emelianova, and GJ Adriaenssens. "Onsager approach to the universal cross-over in variable-range hopping with Coulomb interactions". In: *Solid state communications* 115.3 (2000), pp. 131–136 (cit. on pp. 55, 57).

[55] KW Kim et al. "Metal-insulator transition in a disordered and correlated $SrTi_{1-x}Ru_xO_3$ system: Changes in transport properties, optical spectra, and electronic structure". In: *Physical Review B* 71.12 (2005), p. 125104 (cit. on p. 56).

[56] Zhenyu Wang et al. "Disorder induced power-law gaps in an insulator–metal Mott transition". In: *Proceedings of the National Academy of Sciences* 115.44 (2018), pp. 11198–11202 (cit. on p. 57).

[57] Giniyat Khaliullin. "Excitonic magnetism in Van Vleck–type d 4 Mott insulators". In: *Physical review letters* 111.19 (2013), p. 197201 (cit. on p. 64).

[58] PM Sarte et al. "Van Vleck excitons in Ca_2RuO_4". In: *arXiv preprint arXiv:2011.07425* (2020) (cit. on p. 64).

[59] Antoine Georges, Luca de' Medici, and Jernej Mravlje. "Strong correlations from Hund's coupling". In: *Annu. Rev. Condens. Matter Phys.* 4.1 (2013), pp. 137–178 (cit. on pp. 64, 96).

[60] Jernej Mravlje et al. "Coherence-incoherence crossover and the mass- renormalization puzzles in Sr_2RuO_4". In: *Physical review letters* 106.9 (2011), p. 096401 (cit. on p. 64).

[61] Manuel Zingl et al. "Hall coefficient signals orbital differentiation in the Hund's metal Sr_2RuO_4". In: *npj Quantum Materials* 4.1 (2019), pp. 1–6 (cit. on p. 64).

[62] Heung-Sik Kim, Andrei Catuneanu, Hae-Young Kee, et al. "Kitaev magnetism in honeycomb RuCl 3 with intermediate spin-orbit coupling". In: *Physical Review B* 91.24 (2015), p. 241110 (cit. on p. 64).

[63] Y Maeno et al. "Superconductivity in a layered perovskite without copper". In: *Nature* 372.6506 (1994), pp. 532–534 (cit. on p. 65).

[64] CN Veenstra et al. "Determining the surface-to-bulk progression in the normal-state electronic structure of Sr_2RuO_4 by angle-resolved photoemission and density functional theory". In: *Physical Review Letters* 110.9 (2013), p. 097004 (cit. on p. 66).

[65] K Ishida et al. "Spin-triplet superconductivity in Sr_2RuO_4 identified by ^{17}O Knight shift". In: *Nature* 396.6712 (1998), pp. 658–660 (cit. on p. 66).

[66] Andrej Pustogow et al. "Constraints on the superconducting order parameter in Sr_2RuO_4 from oxygen-17 nuclear magnetic resonance". In: *Nature* 574.7776 (2019), pp. 72–75 (cit. on p. 66).

[67] Kenji Ishida et al. "Reduction of the 17O Knight shift in the superconducting state and the heat-up effect by NMR pulses on Sr_2RuO_4". In: *Journal of the Physical Society of Japan* 89.3 (2020), p. 034712 (cit. on p. 66).

[68] R Matzdorf et al. "Ferromagnetism stabilized by lattice distortion at the surface of the p-wave superconductor Sr_2RuO_4". In: *Science* 289.5480 (2000), pp. 746–748 (cit. on p. 67).

[69] Eunjung Ko et al. "Strong Orbital-Dependent d-Band Hybridization and Fermi-Surface Reconstruction in Metallic $Ca_{2-x}Sr_xRuO_4$". In: *Physical review letters* 98.22 (2007), p. 226401 (cit. on p. 67).

[70] SJ Yuan et al. "From J eff= 1/2 insulator to p-wave superconductor in single-crystal $Sr_2Ir_{1-x}Ru_xO_4$ ($0 \leq x \leq 1$)". In: *Physical Review B* 92.24 (2015), p. 245103 (cit. on pp. 69–71, 73, 93).

[71] Rao MV Rama et al. "Metal to insulator transition in Sr 2 Ru 1-x Ir x O 4". In: *Journal of Physics and Chemistry of Solids* 61.12 (2000), pp. 1989–1999 (cit. on p. 73).

[72] A Glamazda et al. "Effects of hole doping on magnetic and lattice excitations in Sr 2 Ir 1- x Ru x O 4 (x= 0–0.2)". In: *Physical Review B* 89.10 (2014), p. 104406 (cit. on p. 73).

[73] S Calder et al. "Evolution of competing magnetic order in the J eff= 1/2 insulating state of Sr 2 Ir 1- x Ru x O 4". In: *Physical Review B* 92.16 (2015), p. 165128 (cit. on p. 73).

[74] S Calder et al. "Strong anisotropy within a Heisenberg model in the J eff= 1 2 insulating state of Sr 2 Ir 0.8 Ru 0.2 O 4". In: *Physical Review B* 94.22 (2016), p. 220407 (cit. on p. 73).

[75] Madhab Neupane et al. "Observation of a novel orbital selective Mott transition in $Ca_{1.8}Sr_{0.2}RuO_4$". In: *Physical review letters* 103.9 (2009), p. 097001 (cit. on p. 73).

[76] Han-Jin Noh et al. "Electronic structure and evolution of the orbital state in metallic $Ca_{2-x}Sr_xRuO_4$". In: *Physical Review B* 72.5 (2005), p. 052411 (cit. on pp. 74, 76).

[77] Minsoo Kim et al. "Observation of Kondo hybridization with an orbital-selective Mott phase in 4d $Ca_{2-x}Sr_xRuO_4$". In: (2020) (cit. on p. 74).

[78] Dmitry M Korotin, Vladimir I Anisimov, and Sergey V Streltsov. "Pressure-induced magnetic transitions with change of the orbital configuration in dimerised systems". In: *Scientific reports* 6 (2016), p. 25831 (cit. on p. 75).

[79] Jasper van Wezel and Jeroen van den Brink. "Orbital–Peierls transition in the spin chains of $NaTiSi_2O_6$". In: *Journal of magnetism and magnetic materials* 290 (2005), pp. 318–321 (cit. on p. 75).

[80] Paolo G Radaelli et al. "Formation of isomorphic Ir^{3+} and Ir^{4+} octamers and spin dimerization in the spinel $CuIr_2S_4$". In: *Nature* 416.6877 (2002), pp. 155–158 (cit. on p. 75).

[81] Kazunori Nishio, Harold Y Hwang, and Yasuyuki Hikita. "Thermodynamic guiding principles in selective synthesis of strontium iridate Ruddlesden-Popper epitaxial films". In: *APL Materials* 4.3 (2016), p. 036102 (cit. on p. 78).

[82] Junyoung Kwon et al. "Spin-orbit coupling driven orbital-selective doping effect in $Sr_2Ru_{1-x}Ir_xO_4$". In: *Physical Review B* forthcoming (2021) (cit. on pp. 80–82, 84, 86).

[83] JE Ortmann et al. "Competition Between Antiferromagnetism and Ferromagnetism in Sr 2 RuO 4 Probed by Mn and Co Doping". In: *Scientific reports* 3.1 (2013), pp. 1–7 (cit. on p. 96).

[84] JP Carlo et al. "New magnetic phase diagram of (Sr, Ca) 2 RuO 4". In: *Nature materials* 11.4 (2012), pp. 323–328 (cit. on p. 96).

Appendices

Appendix A

Tight-binding calculation method

Tight-binding calculation performed to simulate the SRIO and distinguish the effects of the electron doping and spin-orbit coupling (SOC). To apply the staggered octahedron rotation distortion, the nearest neighbor sites are considered not to be indentical, which is denoted as A and B as in the Figure. Hence, the unit cell is doubled. Total of four orbitals ($d_{zx}, d_{yz}, d_{xy}, d_{x^2-y^2}$). Therefore, the 8×8 (4 orbitals, 2 sites) Hamiltonian consists of NN hopping ($H_{AB,k}$), next NN hopping ($H_{AA,k}$ and $H_{BB,k}$), and SOC (H_{SOC}) is considered to calculate the band structure of SRIO. The total Hamiltonian can be written as

$$H_k = \begin{bmatrix} H_{AA,k} + H_{SOC} & H_{AB,k} \\ H_{AB,k}^{\dagger} & H_{BB,k} + H_{SOC} \end{bmatrix} + [Time\,Reversed]. \tag{A.1}$$

The constituent Hamiltonians are expressed as

$$H_{AB,k} = \begin{bmatrix} d_{NN,1}(k) & d_{NN,2}(k) & 0 & 0 \\ -d_{NN,2}(k) & d_{NN,3}(k) & 0 & 0 \\ 0 & 0 & d_{NN,4}(k) + u_1 & d_{NN,5}(k) \\ 0 & 0 & d_{NN,5}(k) & d_{NN,6}(k) \end{bmatrix}, \tag{A.2}$$

$$\begin{gathered} d_{NN,1}(k) = 2(t_1 \cos k_y + t_2 \cos k_x) \\ d_{NN,2}(k) = -2t_3(\cos k_x + \cos k_y) \\ d_{NN,3}(k) = 2(t_1 \cos k_x + t_2 \cos k_y) \\ d_{NN,4}(k) = 2t_4(\cos k_x + \cos k_y) \\ d_{NN,5}(k) = \tfrac{3}{2}t_5(\cos kx + \cos ky) \\ d_{NN,6}(k) = 4t_6 \cos k_x \cos k_y, \end{gathered} \tag{A.3}$$

for the NN hopping,

$$H_{AA,k} = H_{BB,k} = \begin{bmatrix} 0 & d_{NNN,1}(k) & 0 & 0 \\ d_{NNN,1}(k) & 0 & 0 & 0 \\ 0 & 0 & d_{NNN,2}(k) & 0 \\ 0 & 0 & 0 & d_{NNN,3}(k) + u_2 \end{bmatrix}, \tag{A.4}$$

$$\begin{aligned} d_{NNN,1}(k) &= 4t_7 \sin k_x \sin k_y \\ d_{NNN,2}(k) &= 4t_8 \cos k_x \cos k_y \\ d_{NNN,3}(k) &= t_9(\cos k_x + \cos k_y), \end{aligned} \tag{A.5}$$

for the next NN hopping, and

$$H_{SOC} = \begin{bmatrix} 0 & -i\lambda/2 & \lambda/2 & 0 \\ i\lambda/2 & 0 & i\lambda/2 & 0 \\ \lambda/2 & -i\lambda/2 & 0 & 0 \\ 0 & 0 & 0 & 0 \end{bmatrix}, \tag{A.6}$$

for the SOC Hamiltonian. k_x and k_y represent momentum points with a unit of π/a, where a represents the in-plane lattice constant, and λ is the SOC constant. To calculate the band structure for the case without OR (Figure 4.22), the energy offset of $d_{x^2-y^2}$ (u_2) was set to a huge number (50 eV) to prevent hybridization between e_g and t_{2g}. In the case with OR (Figure 4.23), u_2 was set to 2.8 eV. The values of other parameters are provided in Table I.

Table A.1: Hopping constants used for the band calculations.

t_1	t_2	t_3	t_4	t_5
-0.2	-0.02	0.05	-0.27	0.4
t_6	t_7	t_8	t_9	u_1
1.3	0.01	-0.07	0.1	-0.02

From the calculation, the DOS is calculated from the sum of the number of electron states in 314×314 momentum grid in the Brillouin zone. Fermi level is estimated from the DOS by counting state number from the low energy, considering the electron occupation out of 8 electrons in 4 orbitals. Furthermore, the Fermi surface is drawn with counting the electron states near Fermi level within ± 3 meV. The electron occupation of each band is calculated from the calculated Fermi surface with Luttinger theorem.

국문 초록

스핀-궤도 상호작용에 의한
4d 전이 금속 산화물의 전자적 물성

권준영

서울대학교 대학원

물리학과

응집 물질 물리에서는 전자의 다양한 성질들이 서로 간에 상호 작용을 일으키면서 물성을 형성하는 것이 잘 알려져 있다. 대표적인 예로 전자 간의 전기적 상호작용이 강한 물질은 강상관계 물질로 불리며 모트(Mott) 절연체나 초전도체 등을 형성하는 주요 원인이라고 알려져 있고, 전자의 스핀 간의 상호 작용은 복잡한 자성체를 구성하는 기본적인 현상이라는 것이 알려져 있다. 최근 다양한 방향으로 물성 연구가 확장된 결과, 스핀과 궤도의 상호 작용도 또한 새로운 물성을 이루는 중요한 현상이라는 것이 보고되었다. 스핀-궤도 상호 작용은 일반적으로 무거운 원자로 이루어진 물질군에서 그 특성이 확연하게 발현되는 현상으로, 비스무트와 같은 무거운 원자로 이루어진 Bi_2Se_3과 같은 물질에서 위상 절연체의 특성이 발견되면서 물성 연구에 큰 반향을 일으켰으며, 이리듐이나 백금과 같은 물질이 자성 물질의 조합되면 새로운 자기적 상호 작용에 의해 스커미온(skyrmion)과 같은 새로운 자성이 나타날 수 있다는 것이 보고되었다. 특히 Sr_2IrO_4 (SIO)에서는 이리듐 원자의 5d 궤도가 큰 전기적 상호 작용을 일으키지 못하는 것에도 불구하고 스핀-궤도 상호 작용에 의해 형성된 새로운 전자 고유 상태에서 전기적 상호 작용 효과가 극대화됨으로 인해서 모트 절연체가 될 수 있다는 것이 알려져 있다. 위와

같이 최근의 물성 연구는 스핀-궤도 상호 작용으로 인해 무거운 원자로 이루어진 물질들을 중심으로 과거보다 넓은 범위의 물질 연구가 이루어지고 있다.

본 연구에서는 위와 같은 스핀-궤도 상호 작용 연구를 확장하여 새로운 이해를 도출하고자 한다. 스핀-궤도 상호 작용에 관한 연구는 위와 같이 무거운 원자로 이루어진 물질에서 극단적이고 단순화된 모델을 바탕으로 연구가 활발하게 이루어졌다. 반면 같은 가벼운 원자로 이루어진 물질에서는 그 중요도가 떨어진다는 것이 일반적인 생각이다. 3d 전이 금속 산화물에서는 전자의 궤도가 결정 구조에 크게 영향을 받아 스핀-궤도 상호 작용은 가려지고 작용하지 않는다고 알려져 있다. 하지만 최근 연구에 따르면 4d 전이 금속 산화물에서 스핀-궤도 상호 작용의 역할이 주목을 받게 되었다. 루테늄이나 로듐과 같은 4d 전이 금속은 스핀-궤도 상호 작용의 크기가 150 meV 정도라는 것이 알려져 있어 물질의 밴드 구조에 큰 영향을 끼칠 수 있으며, 그 밴드의 특성이 5d 전이 금속의 경우와 비슷한 특성을 갖는다는 것이 보고 되었다. 나아가 4d 전이 금속 산화물에서는 스핀-궤도 상호 작용이 극단적으로 큰 5d 전이 금속 물질과는 달리 상대적으로 작기 때문에 다른 물성의 영향을 받게 된다. 따라서 전자의 전기적 상호 작용이나 자기적 상호 작용 등이 스핀-궤도와 함께 물리적 현상에 영향을 미치며, 스핀-궤도 상호 작용과 영향을 주고 받는 것을 기대할 수 있다. 본 연구는 위와 같이 상대적으로 작은 스핀-궤도 상호 작용과 다른 상호 작용 간의 복잡한 물리적 현상을 이해함으로써 단순화된 시스템에서 벗어나 스핀-궤도 상호 작용의 더 깊은 이해를 도모하고자 한다.

본 연구는 두 개의 4d 전이 금속 산화물 시스템을 통해 스핀-궤도 상호 작용의 이해를 넓히고자 한다. 첫 번째로 전자를 도핑한 Sr_2RhO_4 (SRhO) 물질은 크지도 작지도 않은 중도의 스핀-궤도 상호 작용을 보여줄 수 있는 시스템이다. SIO와 유사한 밴드 구조를 가지고 있음에도 불구하고 SRhO는 모트 절연체인 SIO와는 달리 두 개의 밴드(band)로 이루어진 금속 특성을 가지고 있다. 이는 스핀-궤도 상호 작용이 SRhO에서 상대적으로 작기 때문에 나타나는 현상으로, 두 개의 밴드가 충분히 에너지 상에서 멀어지지 않았기 때문에 발생하는 현상이다. 두 밴드의 작은

에너지 준위 차이로 인해 SRhO는 전자의 도핑에 따라 하나의 밴드가 페르미 준위 아래로 내려가는 리프시츠(Lifshitz) 전이 현상을 일으킬 수 있다. 본 연구에서는 이 리프시츠 전이와 동시에 남아있는 밴드에서 금속-비금속 상전이 현상이 일어나는 것을 확인하였다. 본 연구는 각분해 광전자 분광(angle-resolved photoemission spectroscopy) 실험을 통해 밴드 구조를 직접적으로 측정함으로써 위와 같은 현상을 제안하고 스핀-궤도 상호 작용에 의한 밴드 구조가 어떤 방식으로 금속-비금속 상전이 현상으로 이루어지는지에 관한 아이디어를 제시하고자 한다.

두 번째 시스템은 $Sr_2Ru_{1-x}Ir_xO_4$ (SRIO)이다. 도핑되지 않은 Sr_2RuO_4 (SRO)는 금속 특성을 보이는 시스템으로 세 개의 밴드가 페르미 준위에 존재하는 것이 확인된 바 있다. 여기에 이리듐을 도핑하면 전자의 갯수, 스핀-궤도 상호작용, 결정 구조 등 다양한 물성이 변화하는 것을 기대할 수 있는데, 이와 같은 물성이 변화하여 SIO 시스템에서는 앞서 말한 바와 같이 스핀-궤도 상호 작용에 의한 모트 절연체 상태가 되는 것이 잘 알려져 있다. 하지만 그 중간 상태에서의 밴드 구조는 충분한 이해가 이루어지지 않았는데, 본 연구에서는 SRO에서 SIO까지 도핑에 따른 복잡한 물성 변화에 따른 밴드 구조를 각분해 광전자 분광 실험을 통해 조사하고자 하였다. 분광 실험에 의하면 SRO의 밴드가 도핑에 의해 그 특성이 변화하면서 밴드 간의 이방성(anisotropy)가 존재하는 것을 발견하였으며, 이방성으로 인해 하나의 밴드에 이리듐이 공급하는 모든 전자가 도핑되는 궤도-선택적 전자 도핑 현상이 발견되는 것을 발견하였다. 본 연구는 밀접 결합 근사를 이용한 밴드 구조 계산을 통해 각 물성 변화에 따른 밴드 구조 변화 경향을 파악하고 궤도-선택적 전자 도핑 현상이 스핀-궤도 상호 작용에 의한 것이라는 해석을 제안하고자 한다.

본 연구는 두 개의 시스템의 총괄적인 연구를 통해 4d 전이 금속 산화물에서도 스핀-궤도 상호 작용이 새로운 물리적 현상을 만들어낼 수 있다는 점을 시사하고자 한다. 일반적인 물질은 다양한 물성이 충돌하면서 복잡한 현상을 야기시킨다는 것이 밝혀져 있으나 특히 스핀-궤도 상호 작용에 관한 연구는 복잡한 시스템보다는 단순화된 모델을 활용한 연구가 대부분이다. 본 연구를 통해 스핀-궤도 상호

작용이 아주 크거나 아주 작아 단순화할 수 있는 시스템 뿐만 아니라 중도의 크기 가지고 다른 물성과 상충하는 시스템에서도 스핀-궤도 상호 작용의 역할을 분리할 수 있으며 중요한 역할을 수행한다는 것을 알리고자 한다. 이를 통해 스핀-궤도 상호 작용에 대하여 더 깊은 이해를 도모하고, 복잡하다고만 알려졌던 4d 전이 금속 물질에서의 새로운 물성에 대한 연구 동기를 제안하고자 한다.

주요어 : 스핀-궤도 상호 작용, 전자 구조, 각분해 광전자 분광, 4d 전이 금속 산화물, 금속-비금속 상전이, 궤도-선택적 현상

학번 : 2016-37300

감사의 글

박사 과정 동안 많은 사람들과 이야기하고 교류하면서 새로운 것들을 많이 배웠습니다. 연구실에 들어온 것이 이렇게 오래됐다고는 생각하기 힘들만큼 시간이 빨리 지나갔지만, 주변 많은 분들의 도움으로 무사히 박사 과정을 마치게 되었습니다. 부족한 학생으로 무언가를 익히는데도 많은 시행 착오를 겪었지만 꾸준히 주변 분들의 가르침과 조언으로 학위 과정을 무사히 통과했습니다. 앞으로도 연구원으로서 많은 일들을 겪고 도움을 받을 사람들께 지면을 빌려 감사의 말씀을 전합니다.

무엇보다 제게 대학원 생활을 시작할 기회를 주시고 인도해주신 김창영 교수님께 감사 드립니다. 갓 들어온 신입생으로 배울 것이 너무나도 많았지만 교수님이 놓아 주신 길을 따라 많은 것들을 배웠고 연구원으로서 갖춰야할 지식뿐만 아니라 생각하는 방향이나 마음가짐에 관해서도 가르침을 받았습니다. 앞으로도 이어질 연구 인생에 시작점이 되어주신 교수님께 감사 드립니다.

제 연구 주제를 처음부터 차근차근 함께 따라가 주시고 밀어 주신 경원식 박사님께도 감사 인사 드립니다. 박사님께서 가지고 계시는 지식이나 노하우, 모든 것들을 친절하게 가르쳐주시고 조언도 해주신 덕분에 박사 과정 무사히 끝마칠 수 있었습니다.

누구보다 제 근처에서 저를 도와주시고 이끌어주신 연구실 동료 분들께도 감사의 말씀 전합니다. 석사 과정 때부터 실험도 같이 해주시고 깊이 생각하도록 해주신 박승룡 교수님, ALS에서부터 많은 아이디어와 재미있는 연구 계획 말씀해 주시던 김용관 교수님, 제 연구에서 가장 기본이 된 시료 성장에서부터 많은 부분을 가르쳐주시고 AIST에서 돌봐 주신 송동준 박사님, 제 석사 연구에 대한 아이디어와 함께 많은 실험 도와주셨던 정원식 박사님께 감사 드립니다. 칭찬도 많이 해주시면서 격려해주신 고윤영 박사님, 제 연구에 세세하게 신경 써 주시며 수많은 질문에도 친절히 같이 생각해 주신 한가람 박사님, 연구실에 신경 많이 쓰시면서도

제 실험까지 진지하게 고민하고 도와주셨던 김범영 박사님, 큰 도움이 되었습니다. 전혀 다른 연구 주제에도 제 얘기를 들어주시고 생각해 주신 서정진 박사님, 외국에 와서 적응하기도 힘든데 같이 즐겁게 얘기하고 도와주신 Shoresh Soltani 박사님께도 감사 드립니다. 많이 부딪치기도 했지만 많은 부분을 받아주시고 연구 생활뿐만 아니라 친한 동생처럼 상냥하게 대해 주신 조수현 박사님, 형처럼 많은 충고와 조언을 주신 김범서 박사님, 큰 장비 꾸리고 돌리느라 고생하시면서도 곧잘 도와주시고 한 살 형이면서도 친구처럼 지내 주신 정종근 형에게도 감사 드립니다.

저보다 조금 늦게 연구실에 들어왔지만 오히려 제게 도움 많이 주신 류한영 형과 후배님들, 허순상, 정우빈, 손병민, 김민수, 김윤식, 김동한, 정새결, 석병준, 김영도, 모두에게도 고맙다고 말하고 싶습니다. 그리고 각분해 분광 실험 장비를 설치하면서 설명도 많이 해주시고 많은 공부를 하도록 도움 주신 김형도 박사님, 분야 다른 연구실 들어오셔서 열심히 공부하시면서도 큰 누나처럼 연구실 사람들을 통솔하고 이끌어주신 송인경 박사님께도 감사 드립니다. 서울대에 들어오게 되면서 설치한 수많은 장비들과 설비들이 갖춰지는 모습을 보면서 위 분들의 큰 도움이 있어 가능했다고 짚고 싶습니다. 바쁘신 와중에도 많은 도움 주시고 조언해주시면서도 즐겁게 연구할 수 있도록 같이 일하며 도움을 주신 김미경 박사님께도 감사의 말씀 드리고 싶습니다. 그리고 연구를 뒤에서 뒷받침 해주시는 행정실의 많은 분들, 장비를 손봐 주시고 자잘한 부분까지 돌봐 주신 기술 지원 팀의 여러분께도 감사 인사 드립니다.

석사 과정 때부터 많은 도와 주시고 공동 연구에 큰 도움을 주신 최영재 교수님과 이나라 박사님, 최환영, 문재영 박사님께도 감사의 말씀 드립니다. 학위 도중에 합쳐서 반 년 이상을 보낸 AIST에서 타지에서 온 학생 임에도 불구하고 많은 도움 주신 吉田良行, 永崎洋, 石田茂之 박사님께도 감사 인사 드립니다. 또한 졸업 심사, 짧은 과정 중에서도 인생에 도움 될만한 많은 지적과 도움을 주신 유재준, 김기훈, 장준호 교수님께도 감사의 말씀을 드립니다.

그리고 물리학자가 되기로 마음먹은 때부터 줄곧 힘이 되어준 친구들, 물리학과

동기들에게도 감사 드립니다. 직장 다니느라 공부 하느라 바쁜 친구들, 외국 나가 고생하는 친구들, 대학원생으로 고생하는 친구들 다 같이 고생하면서도 고민이 있을 때, 좋은 일이 있을 때 친구들 덕에 많은 힘이 되었습니다.

마지막으로 지금까지 신경 써주시고 도와주시고 챙겨주신 부모님, 동생, 가족들에게 정말 감사 드립니다. 덕분에 연구 생활 하며 별 걱정 없이 잘 지낼 수 있었습니다. 그리고 제가 물리학자가 되고자 했을 때 칭찬해주시고 격려해주신 친척들에게도 감사 드립니다.

감사합니다.